

Copyright Warning & Restrictions

The copyright law of the United States (Title 17, United States Code) governs the making of photocopies or other reproductions of copyrighted material.

Under certain conditions specified in the law, libraries and archives are authorized to furnish a photocopy or other reproduction. One of these specified conditions is that the photocopy or reproduction is not to be “used for any purpose other than private study, scholarship, or research.” If a user makes a request for, or later uses, a photocopy or reproduction for purposes in excess of “fair use” that user may be liable for copyright infringement,

This institution reserves the right to refuse to accept a copying order if, in its judgment, fulfillment of the order would involve violation of copyright law.

Please Note: The author retains the copyright while the New Jersey Institute of Technology reserves the right to distribute this thesis or dissertation

Printing note: If you do not wish to print this page, then select “Pages from: first page # to: last page #” on the print dialog screen

The Van Houten library has removed some of the personal information and all signatures from the approval page and biographical sketches of theses and dissertations in order to protect the identity of NJIT graduates and faculty.

ABSTRACT

EXPERIMENTAL AND PHENOMENOLOGICAL STUDY OF PERSISTENT PHOTOCONDUCTIVITY IN $\text{YBa}_2\text{Cu}_3\text{O}_{6+x}$ THIN FILMS

by

Daniel-Dennis McAlevy Bubb

Persistent Photoconductivity in $\text{YBa}_2\text{Cu}_3\text{O}_{6+x}$ thin films is studied by means of infrared photoconductivity measurements after the films have been illuminated with visible light at low temperature. Experimentally, the effect is characterized by the samples' electrical response to infrared light, either causing the resistance to decrease or increase.

A cellular automata model is proposed in explanation of these results and is shown to be consistent with current experimental understanding of this unusual effect, both our results and those of others. The cellular automata model may have application to other unusual optical phenomena exhibited by $\text{YBa}_2\text{Cu}_3\text{O}_{6+x}$ such as resonant Raman scattering.

**EXPERIMENTAL AND PHENOMENOLOGICAL STUDY OF PERSISTENT
PHOTOCONDUCTIVITY IN $\text{YBa}_2\text{Cu}_3\text{O}_{6+x}$ THIN FILMS**

by
Daniel-Dennis McAlevy Bubb

**A Dissertation
Submitted to the Faculty of
New Jersey Institute of Technology and
Rutgers, The State University of New Jersey-Newark,
in Partial Fulfillment of the Requirements for the Degree of
Doctor of Philosophy in Applied Physics**

Federated Physics Department

January 2000

Copyright © 2000 by Daniel-Dennis McAlevy Bubb

ALL RIGHTS RESERVED

APPROVAL PAGE

EXPERIMENTAL AND PHENOMENOLOGICAL STUDY OF PERSISTENT
PHOTOCONDUCTIVITY IN $\text{YBa}_2\text{Cu}_3\text{O}_{6+x}$ THIN FILMS

Daniel-Dennis McAlevy Bubb

Dr. John Federici, Dissertation Advisor, Committee Chair
Associate Professor of Physics, Applied Physics, NJIT

Date

Dr. John Hensel, Committee Member
Distinguished Professor of Physics Emeritus, Applied Physics, NJIT

Date

Dr. Earl Shaw, Committee Member
Chairperson and Professor of Physics, Physics, Rutgers-Newark

Date

Dr. Gordon Thomas, Committee Member
Member of the Technical Staff, Murray Hill Bell Laboratories, Lucent Technologies

Date

Dr. William Wilber, Committee Member
U.S. Army Communications Electronics Command (CECOM), Fort Monmouth, NJ

Date

Dr. William Savin, Committee Member
Professor of Physics, Applied Physics, NJIT

Date

BIOGRAPHICAL SKETCH

Author: Daniel-Dennis McAlevy Bubb
Degree: Doctor of Philosophy in Applied Physics
Date: January 2000

Undergraduate and Graduate Education:

- Doctor of Philosophy in Applied Physics,
New Jersey Institute of Technology, Newark, NJ, 2000
- Master of Science in Physics,
Florida Institute of Technology, Melbourne, FL, 1995
- Bachelor of Science in Physics,
Ursinus College, Collegeville, PA, 1993

Major: Applied Physics

Presentations and Publications:

D. M. Bubb, J. F. Federici, *Cellular Automata Model for Persistent Photoconductivity in YBCO*, submitted to Journal of Physics : Condensed Matter.

D. M. Bubb, J. F. Federici, K. -H. Dahmen. *Two Component Bolometric Response of CMR Thin Films*, submitted to Thin Solid Films.

G. A. Thomas, D. M. Bubb T. Y. Koo, S. W. Cheong and J. F. Federici, *Lighting up Erbium with water: Observation of substantial crystalline matrix element enhancements*, submitted to Science.

D. M. Bubb, J. F. Federici, W. Wilber, S. Tidrow, J. Kim, and A. Piqué. *Wavelength and Photon Dose Dependence of Infrared Quenched Persistent Photoconductivity in $YBa_2Cu_3O_{6+x}$* , Phys. Rev. B **60**, 6827-33 (1999).

Daniel M. Bubb, *Persistent Photoconductivity in $YBa_2Cu_3O_{6+x}$ Thin Films*, Army Research Laboratory Seminar, 1 July 1999.

Daniel M. Bubb, *Wavelength and Photon Dose Dependence of Infrared Quenched Persistent Photoconductivity in $YBa_2Cu_3O_{6+x}$* , Naval Research Laboratory Seminar Series, 19 May 1999.

J. F. Federici, D. M. Bubb, W. Wilber, S. Tidrow, J. Kim, and A. Piqué. *Wavelength and Photon Dose Dependence of Infrared Quenched Persistent Photoconductivity in $YBa_2Cu_3O_{6+x}$* . Bul. Am Phys. Soc. **44**, 323 (1999).

D. M. Bubb, J. F. Federici, T. A. Tyson, E. Gillman, K. –H. Dahmen. *Temperature Dependent Photodoping of CMR Thin Films*, Bul. Am Phys. Soc. **44**, 1657, (1998).

D. M. Bubb, J. F. Federici, T. A. Tyson, E. Gillman, K. –H. Dahmen. *Photodoping of CMR Thin Films*, Bul. Am Phys. Soc. **43**, K38.22, (1998).

D. M. Bubb, J. F. Federici, T. A. Tyson, W. Savin, W. Wilber, and H. Blackstead, *Wavelength Dependence of Infrared Quenched Persistent Photoconductivity in $Y123$* , Bul. Am Phys. Soc. **42**, 767, (1997).

This thesis is dedicated to my beautiful wife and
in loving memory of Emilie Elizabeth McAlevy

ACKNOWLEDGMENT

First and foremost I would like to thank my wife for her endless support. Thanks, Peg.

I have had the wonderful privilege of having Dr. John Federici as a thesis advisor, for whom I have deep respect and admiration both personally and professionally.

I would like to thank all of my committee members for their service. Especially, I would like to thank Dr. John Hensel for careful reading of the manuscript. Dr. Gordon Thomas has been a *remarkable* source of insight and advice.

I would like to thank the National Science Foundation for funding the initial phase of research.

Dr. Ann K. Heilman has been a dear friend, I thank her for her timely assistance with samples and contacts. Also, I thank Drs. Steven Tidrow, Alberto Piqué, and Jeonggo Kim for providing us with samples. Geraldo Molina's efforts were instrumental in the early phase of the project. The 'Tuesday-nite' crew has been very helpful.

Dr. Trevor Tyson's door has always been open for insightful discussions. Similarly, I thank Dr. Beau Farmer. Dean Poate made it easier for us to get LN2 when we needed it. Dr. Haim Grebel allowed us to use a 1.3 μm laser for an extended period of time without complaint.

Additionally, I thank my family and friends for supporting my efforts. Especially, I would like to thank my father for instilling within me a deep desire to succeed, and to my mother for teaching me curiosity of all things when I was very young. My brother Michael has been very influential in my intellectual development.

Thanks to my 'outlaws' for warm meals and keeping me level!

Dr. J. M. Joseph has provided invaluable assistance and guidance.

Finally, I thank the Olsen family along with the good people at The School at Church Farm for their efforts.

TABLE OF CONTENTS

Chapter	page
1 INTRODUCTION AND OVERVIEW.....	1
2 PERSISTENT PHOTOCONDUCTIVITY IN $\text{YBa}_2\text{Cu}_3\text{O}_{6+x}$ THIN FILMS.....	18
3 SAMPLE PREPARATION AND CHARACTERIZATION.....	51
4 EXPERIMENTAL TECHNIQUES AND APPARATUS.....	68
5 EXPERIMENTAL RESULTS.....	83
6 CONCLUSION	105
APPENDIX REPRESENTATION OF CELLULAR AUTOMATA	107
REFERENCES.....	108

LIST OF TABLES

Table		Page
1	Summary of characterization data for $\text{YBa}_2\text{Cu}_3\text{O}_{6+x}$ samples	56

LIST OF FIGURES

Figure	Page	
1	Crystal Structure of YBCO (a) orthorhombic phase (b) tetragonal symmetry. Site numbers explained in text, axes are shown. Note that for (a), $a \neq b$, and in (b) $b = a$. Adapted from Ref. [14]. When $x = 0$ in $\text{YBa}_2\text{Cu}_3\text{O}_{6+x}$, sites O(1) are unoccupied. In a) pure orthorhombic phase is shown, O(5) sites are empty. In the bottom of Fig. 1a the unoccupied O(5) sites are marked with an X	6
2	Schematic of a) structural phase diagram. T –tetragonal phase, O-I pure orthorhombic phase, O-II cell-doubled orthorhombic phase. O-III phase omitted for clarity. b) electronic (magnetic) phase diagram. AF anti-ferromagnetic, SC superconducting phase. Metal-insulator transition near $x = 0.4$	8
3	Basal plane of O-II phase ($\text{YBa}_2\text{Cu}_3\text{O}_{6.5}$) The movement of oxygen into occupied chains produces two holes. Assumes negligible occupation of O(5) sites, a and b axes indicated on diagram. Exclamation points mark process in which O(1) atom moves from nearly empty chain to nearly full chain resulting in transfer of two holes to planes.....	10
4	Change in resistance during illumination for YBCO sample with $x \approx 0.3$. (Sample A in Table 1, Section 3.2.3)	12
5	Comparison of T_c enhancement for illumination and room temperature annealing. Adapted from Ref. [26]	14
6	Quenching Efficiency for Sample C in Table 1, Section 3.2.4. The sample had previously been illuminated with $\sim 10^{22}$ 2.4 eV (514.5 nm) photons before being exposed to IR light	15
7	PPC Spectral Efficiency – note large enhancement at 4.1 eV. Adapted from Ref. [46]	25
8	O(4) Raman mode for several exciting wavelengths. Note three separate contributions. Adapted from Ref. [60]	31
9	(a) Photoinduced diffusion model – upon photoexcitation oxygen moves from position 1 -> 2 in diagram. Shows resulting orthorhombic distortion. (b) Associated double well potential. Adapted from Ref. [23, 35]	33
10	Percentage of basal plane oxygen atoms in chains of various length. Adapted from Ref. [27]	34

LIST OF FIGURES
(Continued)

Figure	Page
11 Schematic of interactions included in ASYNINI model for O-II phase. Thick lines connecting sites indicate interactions – (a) V_1 , (b) V_2 , (c) V_3 . Adapted from Ref [34].....	37
12 Polarization of chains through dipole formation. (a) O(1) site has -1 valence (b) transfer of an electron (charge transfer) from O(4) site results in dipole moment on O(1) site. Adapted from Ref. [35]	39
13 Optical Conductivity of $\text{YBa}_2\text{Cu}_3\text{O}_{6+x}$ crystal with $x \approx .2$. Dashed line shows two separate contributions to spectrum. Adapted from Ref. [83]	46
14 (a) proposed band structure for fully deoxygenated YBCO. Cu(2) $3d^{10}$ band is above Fermi energy. Cu(1) $3d^{10}$ band acts as narrow intragap band. O(2,3) 2p and Cu(2) $3d^9$ bands are hybridized and lie below Fermi energy, i.e. valence band. O(2,3) 2p and Cu(2) $3d^9$ and Cu(2) $3d^{10}$ are separated by charge transfer gap of 1.7 eV and Cu(1) $3d^{10}$ and Cu(2) $3d^9$ are separated by 1.3 eV. (b) Schematic of process involving midgap luminescence (1) electron-hole pair is created, (2) hole migrates from valence band to Cu(1) $3d^{10}$ band, (3) electron experiences Coulombic interaction with $3d^{10}$ hole and forms exciton below conduction band, (4) recombination of electron and hole with photon emission. (c) 1.16 eV resonant Raman scattering - ω_i incident photon, ω_s scattered photon. Adapted from Ref. [85].....	47
15 Variation of c-axis lattice parameter with oxygen deficiency (δ in $\text{YBa}_2\text{Cu}_3\text{O}_{7-\delta}$). Ref [94].....	54
16 Bragg peaks of Sample A after initial post-deposition annealing to make $\delta \approx 0$	57
17 (a) conditions for Bragg scattering (b) detector arrangement	59
18 Log-log plot to illustrate effect of annealing on c-axis lattice parameters. Number above peak is index l in $(0\ 0\ l)$ reflection, S indicates substrate peak. Note shift to higher d-spacing when oxygen is removed	60
19 Width and intensity of (005) peak at intermediate annealing stage (1) and after final (2) annealing. Note that even though the intensity has changed by a factor of 2.4, the width remains constant	61
20 Increase in photoresponse, i.e. $\Delta R/R\%$ as a result of annealing for Sample A.....	62

LIST OF FIGURES
(Continued)

Figure	Page
21 Film A : first order Raman spectrum (A) at moderate power density, and (B) after exceeding the damage threshold. Numbering of modes explained in text	63
22 Oxygen content as a function of radial distance from center of damaged spot. Adapted from Ref. [107]	65
23 Sample mounting, 4-point technique, and circuit used to measure voltage drop across sample, v. Note that $R \gg r$	70
24 Sample/contact geometry. Application of I, and measurement of V shown for Sample B	71
25 Optical access cryostat used in study	75
26 Rotation of polarization of pump beam	77
27 Ti:Sapphire Laser Cavity. See text for explanation on mirror numbering	78
28 Monitoring the wavelength of the Ti:Sapphire laser	81
29 Relative change in resistivity vs. cumulative photon dose for several films (inset) Fit of resistivity vs. time (Eqn. 2.1) for Sample A when illuminated with 4 W all lines Ar+ laser light. Fit parameters shown on plot	83
30 Hysteresis in Resistance vs. Temperature curve for Sample A. Sample is cooled to 77 K, then illuminated. It is allowed to slowly warm, excess conductivity decays in about 30 hours	84
31 Contrasting the behavior of Sample E when illuminated at 296 K and 77 K, respectively	85
32 IR Photon Energy Dependence of Quenching Efficiency for Samples A & B (after visible illumination)	87
33 Comparison of HE band of Ref [79] with photon energy dependence results for Quenching Efficiency of Fig. 32. Dashed line represents linear fit to one of the trials in Fig. 32. Left vertical axis in units of $10^{-4} -\Delta T/T$	88
34 Comparison of Sample A's response to 1.4 eV (887 nm) before and after illumination with visible light	90

LIST OF FIGURES
(Continued)

Figure	Page
35 Comparison of Sample C's response to 1330 nm (.93 eV) and 514.5 nm (2.4 eV). The response to Ar+ light is about an order of magnitude greater than 1330 nm light which is consistent with the spectral efficiency measurements of Refs. [23, 29, 46]	92
36 Quenching Efficiency as a function of Cumulative Visible Photon Dose for Sample A (1330 nm)	93
37 Representation of basal plane of oxygen deficient YBCO below the metal insulator transition. (a) an electron is trapped leading to the motion of oxygen into the chains, the disturbance propagates to the next lattice site – it will propagate until it reaches a vacancy or the situation in (b) electron cannot be trapped because oxygen cannot move into chain	97
38 Growth of average chain length while lattice is perturbed. Inset shows fit of Eqn. 5.1 to data for one of the lattices with $\beta = .85$	99
39 Simulated resistivity as a function of 'illumination time' (perturbations)	103
40 Flowchart representing Cellular Automata code	107

CHAPTER 1

INTRODUCTION AND OVERVIEW

1.1 Introduction

Persistent photoconductivity (PPC) and photoinduced superconductivity (PISC) have been the subject of a recent review article which details the remarkable interaction of high temperature superconducting thin films with light [1]. Many new superconductors interact with light differently from their ‘conventional’ predecessors [2]. Instead of weakening the superconducting properties, illumination enhances every single measure of superconductivity in $R\text{Ba}_2\text{Cu}_3\text{O}_{6+x}$ (R = rare earth or Y) as well as other select other materials [1]. Since the mechanism behind high temperature superconductivity has not been elucidated yet, understanding PPC and PISC may shed some light on this question.

A variety of optical and transport measurements have been done on high temperature superconducting materials before, after, and during illumination [1]. Studying the changes that occur as the superconducting properties are optically ‘tuned’ provides valuable information about the differences between normal state and superconducting properties. In addition, there is an analogy between the light induced changes that occur and doping by other (perhaps chemical) means. The light induced changes are fully reversible and much cleaner than chemical doping. Also, studying insulating samples which remain in the normal state, allows us to probe a defect structure which, when populated with trapped carriers, may act as a protagonist or precursor to the observed structural changes.

The objective of this dissertation is to present new experimental results in support of a defect-based model for PPC and PISC in $R\text{Ba}_2\text{Cu}_3\text{O}_{6+x}$, which incorporates the observed rearrangement of oxygen within the material in a natural way. In order to gain understanding of the mechanism for PPC we performed infrared photoconductivity measurements on insulating thin film samples of YBCO at low temperature (77 K). We performed these measurements before and after illumination with visible light in order to diagnose an intrinsic defect structure in YBCO which may be responsible for PPC. Our experimental results suggest that a defect structure is ultimately responsible for the observed phenomena. We also present a cellular automata simulation which models the time dependent behavior of illuminated samples. The results of this simulation, when interpreted within currently accepted theory, predict the correct magnitude of the relative change in resistivity due to illumination. The sum of our experimental results, coupled with our simulation support our basic premise that trapped charges lead to structural rearrangements, and a higher conductivity state.

This document will be organized as follows: the remainder of Chapter 1 will provide the necessary background in which the problem of PPC/PISC is properly cast. Chapter 2 will review the literature in this field and explore some of the proposed explanations in detail, but stop short of the new work to be presented. Chapter 3 will detail the sample preparation, fabrication, and characterization. Chapter 4 will describe the experimental setup and techniques used in the study. In Chapter 5, the experimental results will be presented with a proposed explanation in the form of a cellular automata. Finally, Chapter 6 will serve as a summary.

1.2 Superconductivity

Superconductivity was discovered by H. Kamerlingh Onnes in 1911 [3]. In elemental mercury a zero resistance state was observed at a critical temperature (T_c) of 4.1 K. It was not until the 1950's that a satisfactory explanation could be put forth to explain the microscopic mechanism behind this striking phenomenon [4]. This is the so-called "BCS" model of superconductivity. Simply put, below T_c , the free electrons in a superconductor are in a paired state, which is mediated through the exchange of a virtual phonon. An energy gap arises from the formation of pairs, which depends on the strength of the electron phonon coupling and the Debye frequency. The free electrons are paired in momentum space (Cooper pairs). The actual pairing distance, as gleaned from the pairing wavefunction, is typically larger than the spacing between Cooper pairs. The ground state of the electron gas is unstable with respect to the formation of these pairs. Since the paired electrons (net spin = 0) can be treated as bosons, statistical mechanics tells us that near absolute zero the pairs will collapse into the same ground state. Thus, superconductivity is a collective state of the electron gas, which cannot be thought of as simply consisting of pairs of electrons.

The superconducting state is characterized by zero resistance, but a superconductor is more than just a 'perfect' conductor. The microscopic pairing of the electrons has a macroscopic consequence: diamagnetism. The pairs of electrons with opposite spins effectively shield the interior of the superconducting material against magnetic flux for fields of sufficiently low strength ($H < H_c$). Fields exceeding H_c will break apart the Cooper pairs. In a similar fashion the response of superconductors to electromagnetic fields is characterized by strong absorption if the photons have energy

equal to or greater than the superconducting energy gap. Typically this gap leads to an absorption edge in the far infrared to microwave region at absolute zero [5]. This absorption results in the breaking of Cooper pairs and degrades the superconducting properties of the material. By monitoring changes in the far-infrared transmission while exciting with visible light, workers have resolved the Cooper pair breaking in time [6].

In addition, it was observed that among the isotopes of a given element, there is an empirical law between the critical temperature and the atomic mass number, M :

$$T_c \propto M^{-\alpha} \quad (1.1)$$

where $\alpha \sim .5$. One of the triumphs of BCS theory is that it predicts an exponent of $\sim 1/2$ [7]. This observational relationship is known as the isotope effect and was a crucial clue in understanding that pairing is mediated by the electron-phonon interaction.

1.3 High Temperature Superconductivity

In 1986 the discovery of a new class of materials with large critical temperatures occurred [8]. The so-called High- T_c materials presented new and formidable challenges for conventional BCS theory. The electron-phonon coupling and the density of states near the Fermi surface are input parameters in BCS theory. One can never achieve the large critical temperatures exhibited by High- T_c materials with physically reasonable input parameters within the context of BCS theory [9]. The absence of the isotope effect [5,9] further casts doubt upon the possibility of understanding the High- T_c materials within the BCS framework. More troubling is the inability of the newer models such as the resonant valance bond (RVB) [9] and the

modified Hubbard models [10] to account for the coexistence of antiferromagnetism and metallic behavior in the phase diagram. Extensive band structure calculations have been carried and reviewed [11] thoroughly, but have been unable to account for the existence of antiferromagnetism in the ground state in many of the high- T_c materials.

More recent reviews seem to indicate that we are not much further along in understanding the mechanism of High- T_c Superconductivity than we were ten years ago [9]. It is precisely for this reason that understanding PPC and PISC in the High- T_c compounds is a worthwhile goal.

1.4 $\text{YBa}_2\text{Cu}_3\text{O}_{7-\delta}$: Phenomenology

1.4.1 Crystal Structure and Phase Diagram

The most well known of all the High- T_c superconductors is $\text{YBa}_2\text{Cu}_3\text{O}_{7-\delta}$ (YBCO). The lanthanum containing compounds synthesized by Bednorz and Mueller showed increased T_c 's when subjected to pressure ($\frac{dT_c}{dP} > 0$). To introduce 'chemical' pressure into the system, smaller and isovalent yttrium was substituted for lanthanum. The compound YBCO was first synthesized in 1987 [12]. It's T_c of approximately 92 K broke the liquid nitrogen barrier (77 K) and it's relative ease of synthesis has made it extremely popular among High- T_c researchers. Depending on the oxygen concentration in the material, the crystal structure assumes either tetragonal or orthorhombic symmetry. Actually, the structure also depends on temperature, but we will postpone a discussion of this point until we develop a phase diagram shortly. The crystal structure of YBCO is shown in Figure 1.

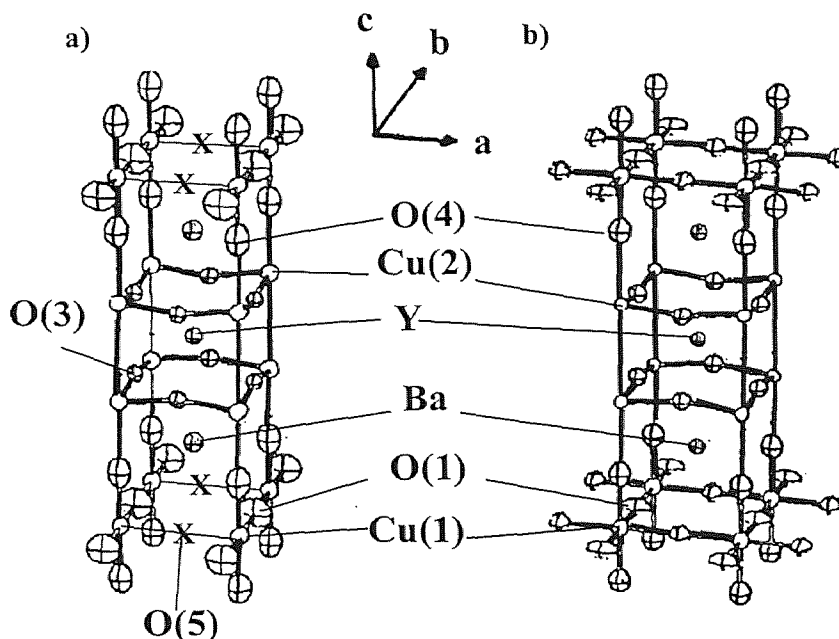


Figure 1 Crystal Structure of YBCO (a) orthorhombic phase (b) tetragonal symmetry. Site numbers explained in text, axes are shown. Note that for (a), $a \neq b$, and in (b) $b = a$. Adapted from Ref. [14]. When $x = 0$ in $\text{YBa}_2\text{Cu}_3\text{O}_{6+x}$, sites O(1) are unoccupied. In a pure orthorhombic phase is shown, O(5) sites are empty. In the bottom of Fig. 1a the unoccupied O(5) sites are marked with an X.

Moving from Figure 1 a) to Figure 1 b) the sites marked O(1) and O(5) become equivalent. So do the sites O(2) and O(3). The change to orthorhombic symmetry occurs when the oxygen preferentially occupies O(1) sites at the expense of O(5) sites. This string of O(1) sites, randomly occupied short of full oxygenation, is known as the “chain” layer. In fully oxygenated YBCO there are no O(1) vacancies and the chains consist of long lines of consecutively occupied O(1) and Cu(1) sites along the b-axis connecting one unit cell with the next. In either crystal structure the puckered planes are simply referred to as the “planes.” Their occupancy remains the

same and the only change that occurs within the planes during the structural phase transition is that the O(2) and O(3) sites become nonequivalent.

The structural transition, tetragonal \rightarrow orthorhombic just cited above, depends not only on oxygen concentration, x , but also temperature such that it can be represented in a T vs. x structural phase diagram as in Figure 2a. Besides the tetragonal phase, there are in fact two orthorhombic phases that can be distinguished, O-I and O-II. In the O-I phase, the oxygens are randomly distributed on O(1) sites as discussed above. The second orthorhombic phase, the unit cell doubled O-II phase, exists in intermediate oxygen concentrations $.3 \leq x \leq .7$. The 'pure' O-II phase exists in a narrower range of oxygen concentration around $x = .5$. This unit-cell doubled phase is marked by alternating full and empty chains.

The ordering of oxygen atoms (vacancies) in the O-II phase in the basal plane is a remarkable phenomenon that occurs in YBCO after synthesis. The critical temperature has been shown to depend on the amount of orthorhombic order (ratio of b and a lattice parameters) in the chains [13]. In an experiment [14], samples of YBCO were heated above the O-II \rightarrow T phase transition in a pure oxygen atmosphere. Samples that were returned to room temperature quickly, i.e. 'quenched', showed reduced T_c . The critical temperature was found to recover if the samples were maintained at room temperature. This aging effect, characterized by a change in T_c ($\Delta T_c > 0$), is a function of oxygen content [15]. This enhancement occurred for oxygen contents in the range 6.4 to 6.6 with T_c roughly 10-60 K, and ΔT_c peaking at 12 K [15]. Enhancements of T_c as large as 20 K have been reported, and it was originally believed that there would be a strong relationship between increased O(1) occupancy and ΔT_c .

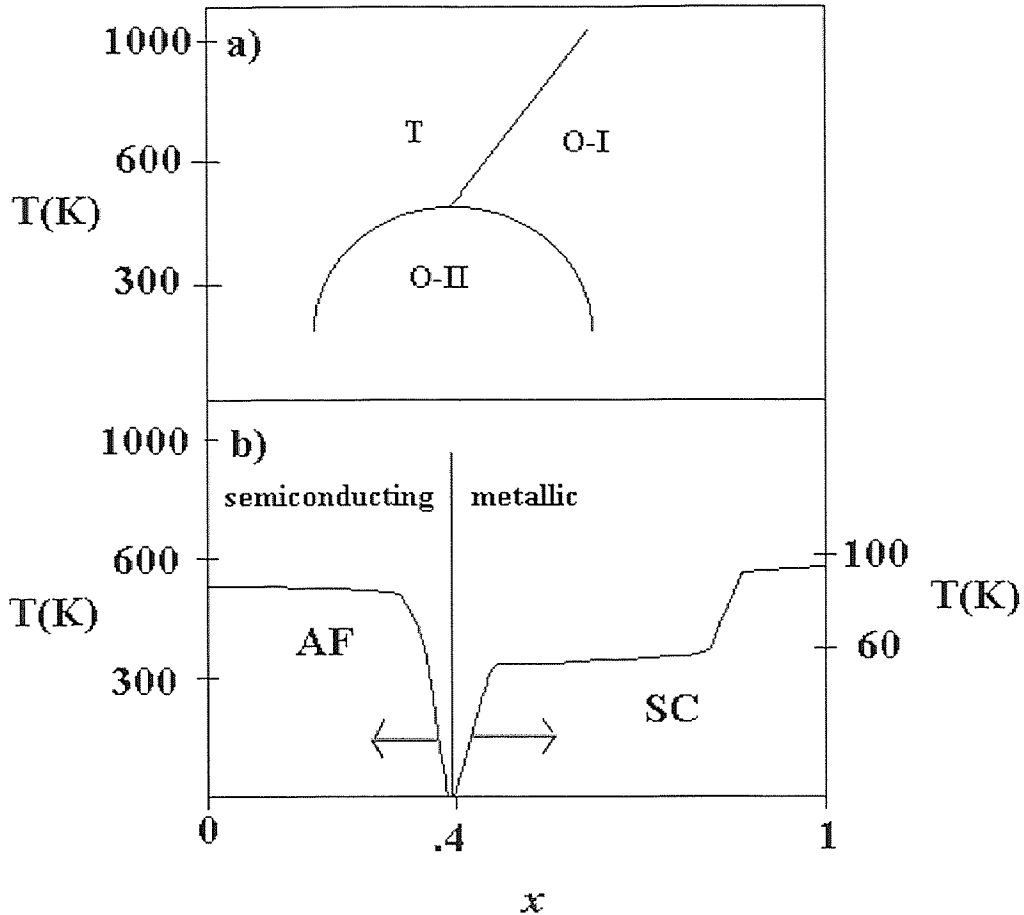


Figure 2 Schematic of a) structural phase diagram. T –tetragonal phase, O-I pure orthorhombic phase, O-II cell-doubled orthorhombic phase. O-III phase and others omitted for clarity. b) electronic (magnetic) phase diagram. AF anti-ferromagnetic, SC superconducting phase. Metal-insulator transition near $x = 0.4$.

That is, it was expected that the mechanism would involve oxygen atoms moving from O(5) sites to O(1) sites. Surprisingly, this is not the case. It turns out that the mechanism is more subtle. The relevant parameter is the oxidation state of the Cu(1) sites as will be explained shortly. Measurements on ceramic $\text{YBa}_2\text{Cu}_3\text{O}_{6.41}$ quenched rapidly from 520°C showed orthorhombic order but were not initially superconducting [14]. (The average occupancy of the O(I) sites was ~ 0.38 while the

occupancy of O(5) sites was ~ 0.4 .) During the aging process the occupancy of the O(1) and O(5) sublattices did not appreciably change. However, ΔT_c increased approximately 20 K ($0 \rightarrow 20\text{K}$). There was also an accompanying increase in the diamagnetic moment. This seemed to contradict earlier results which indicated that the shift in T_c was directly related to an increase in the O(1) sites at the expense of O(5). In the $\text{YBa}_2\text{Cu}_3\text{O}_{6.41}$ sample [14], there was definitely an increase in the basal plane orthorhombicity, defined as the difference in the a and b axis lattice parameters. However, this increase in orthorhombic order could not be traced to decreasing O(5) sublattice population as previously believed [13].

In Figure 2 b) the electronic (magnetic) phase diagram for $\text{YBa}_2\text{Cu}_3\text{O}_{6+x}$ is shown. For the low oxygen contents on the left side of the diagram, the material is antiferromagnetic and insulating. The upper boundary to region “AF” represents the Néel temperature (T_N), which rapidly drops to zero as the metal insulator transition is approached from the left. On the right side the upper boundary of “SC” gives the superconducting critical temperature (T_c) which also drops to zero as the metal insulator transition is approached from the right. The so-called ‘60 K – plateau’ occurs for oxygen contents around $x = 0.5 \rightarrow 0.8$. This is characterized by nearly flat dependence of T_c on the oxygen content.

1.4.2 Charge Transfer Hypothesis

Early work focused on the observed structural changes that occur as the oxygen content is gradually increased from zero [16]. There is a step-like increase in the c-axis lattice

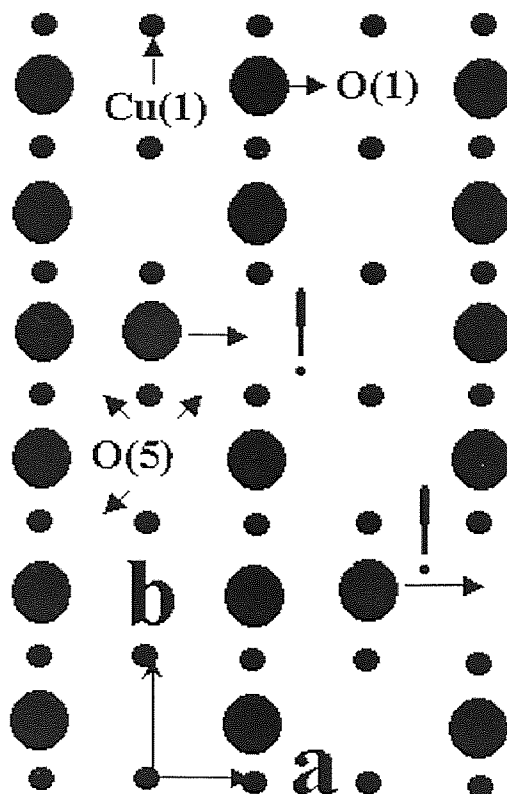


Figure 3 Basal plane of O-II phase (YBa₂Cu₃O_{6.5}) The movement of oxygen into occupied chains produces two holes. Assumes negligible occupation of O(5) sites, a and b axes indicated on diagram. Exclamation points mark process in which O(1) atom moves from nearly empty chain to nearly full chain resulting in transfer of two holes to planes.

parameter as the metal insulator transition is crossed related to the transfer of charge from the puckered planes to the chain layers. Alternatively, adding oxygen to the chain layers can be viewed as doping the puckered planes with holes. As previously mentioned, the transfer of holes is related to the oxidation state of the Cu(1) site. In this model, twofold coordinated Cu(1) sites are assigned to the +1 state. Threefold and higher coordinations are assigned to the +2 state. Initially, following quenching, a random distribution of O atoms in the chain layer will lead to a maximization of

threefold coordinated Cu(1) sites, and hence Cu^{+2} . As shown in Figure 3, for oxygen content 6.5 (O-II phase), the reordering of O atoms *locally* to every other chain will lead to the creation of two monovalent Cu(1) sites in the vacancy chains, and two divalent sites in the oxygen chains. The site that the oxygen moves to is already bordered by two Cu(1) sites in the +2 state, so there is a net transfer of charge between the chains and planes. This *local* oxygen ordering process is to be distinguished from the *global* [13] process in which the O(1) sublattice occupancy increases at the expense of the O(5) sublattice. The local process reflects the experimental result that the relative population of oxygen sublattices does not change, and it accounts for the charge transfer in a natural way. Experimental evidence to support this ordering process is not limited to x-ray and neutron diffraction. Optical measurements in the infrared (IR) support the notion that there is an increase in the $\text{Cu}(1)^{+1}$ sites over time [17].

1.4.3 Blackstead-Dow Model

Attempts have been made to discredit the so-called “charge-transfer hypothesis,” on the basis that it violates charge conservation [18, 19]. These conclusions are dependent upon the use of bond-valence sum method to extract layer charges from neutron diffraction data. This method assumes strictly ionic valences for the constituents in YBCO, an assumption which is hard to reconcile with metallic behavior in the phase diagram. The layered High- T_c cuprate compounds show a remarkable mixture of ionic and covalent bonding. It seems that any theory attempting to explain superconductivity in them must allow for a mixture of both types of bonding. However, the so-called Blackstead-Dow (B-D) model correctly predicts superconductivity to exist in the

closely related $\text{PrBa}_2\text{Cu}_3\text{O}_{7-\delta}$ system. The authors predict that the condensate occurs in the charge reservoir layers. There is preliminary experimental evidence of superconductivity [20], but there are many unresolved questions about the substitutional nature of the Pr^{+3} ion [21, 22].

1.5 Persistent Photoconductivity in YBCO

1.5.1 Relationship of PPC to Oxygen Ordering

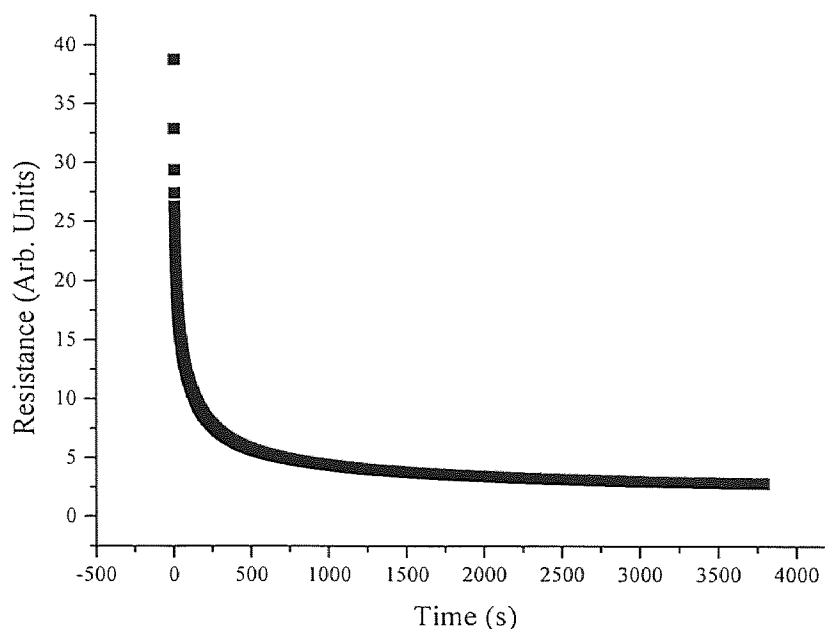


Figure 4 Change in resistance during illumination for YBCO sample with $x \approx 0.3$. (Sample A in Table 1, Section 3.2.4)

Vacancy ordering is not the only remarkable phenomenon to occur in YBCO. If oxygen deficient YBCO is exposed to visible light, its normal state conductivity is increased. The excess conductivity persists with time, long after the light is shut off. At low temperature (<270 K) the lifetime of the photoinduced state is essentially

infinite. Figure 4 shows the resistivity of a $\text{YBa}_2\text{Cu}_3\text{O}_{6.4}$ thin film during illumination. The resistivity decreases according to stretched exponential dependence on illumination time. This functional dependence will be discussed in Chapter 2. Measurements for a range of oxygen contents [23] show that the effect is peaked near the metal insulator transition. Remarkably, the superconducting properties can be favorably affected as well. Samples at the edge (insulating side) of the metal insulator transition that would not otherwise become superconducting, will do so if illuminated with sufficient photon dose. Illuminated samples show increased diamagnetic moment, larger critical current, and a positive shift in T_c [23]. Also, changes in structure during illumination [24] track changes in resistivity. Local structure measurements show that the Cu(1)-O(4) bond lengths distribution splits into two well defined peaks, indicating that there is some ordering process that occurs during illumination [25]. Other measurements showed that the enhancement of T_c as a function of oxygen content [26] bore remarkable similarity to that which is due to room temperature annealing [15].

Figure 5 shows a comparison of the room temperature annealing effect [15] and the enhancement of T_c due to illumination [26]. A class of models began to emerge which described the phenomenon in terms of photoinduced basal plane ordering in analogy to room temperature annealing. These models are generally referred to under the blanket term: “oxygen ordering.”

1.5.2 Vacancy Capture Model

Experimental evidence began to appear that suggested these oxygen ordering models provided incomplete description [27, 28] of the mechanism for persistent

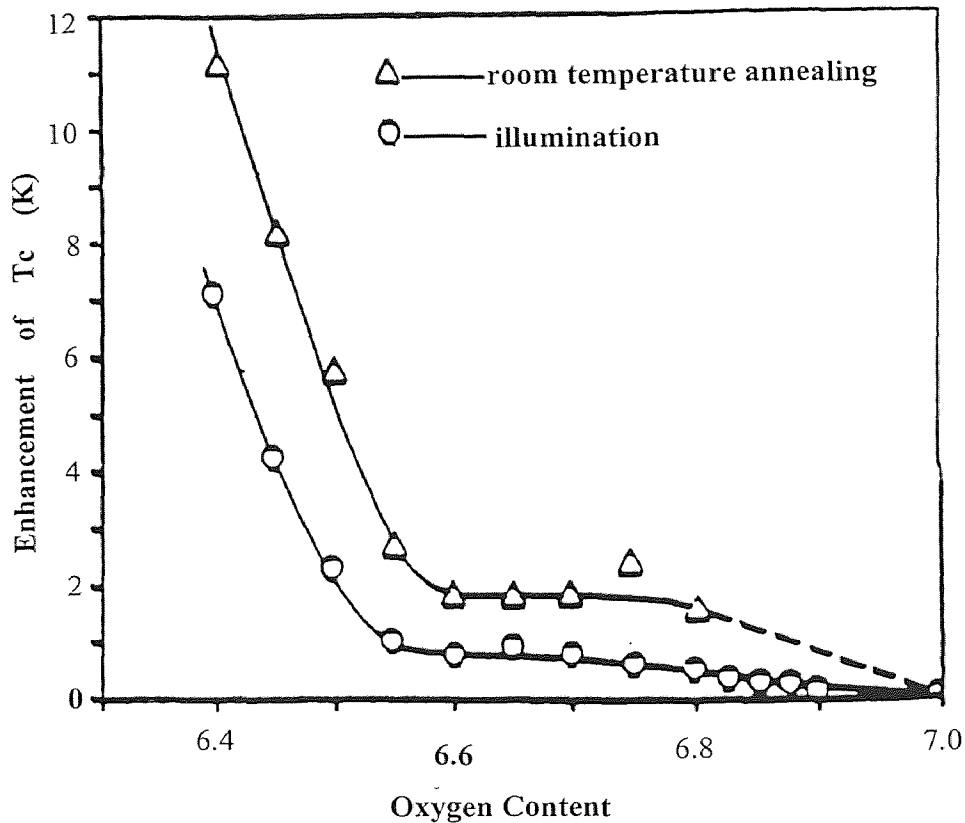


Figure 5 Comparison of T_c enhancement for illumination and room temperature annealing. Adapted from Ref. [26].

photoconductivity (PPC) and photoinduced superconductivity (PISC) in YBCO. A new explanation arose, the “vacancy capture” model. In this model, oxygen vacancies in the basal plane act as traps for photogenerated electrons. Once an electron-hole pair is created during illumination, if the electron is trapped, the hole can contribute to the conductivity by being transferred to the CuO_2 planes. Experimental evidence for the vacancy capture model has centered on photoconductivity measurements [27, 28], photoluminescence measurements [29], and infrared photoconductivity after illumination [30]. Peaks in the photoluminescence spectrum that are associated with

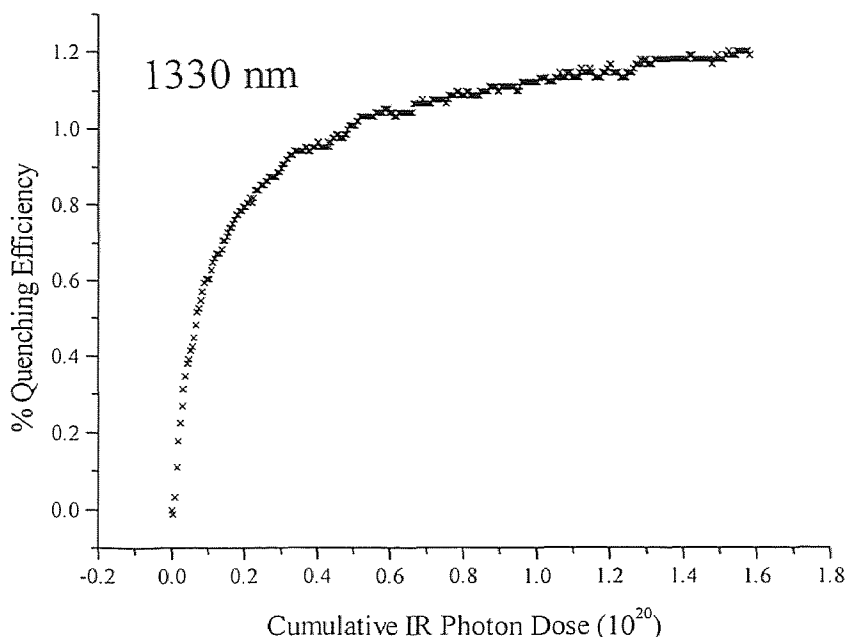


Figure 6 Quenching Efficiency for Sample C in Table 1, Section 3.2.4. The sample had previously been illuminated with $\sim 10^{22}$ 2.4 eV (514.5 nm) photons before being exposed to IR light.

oxygen vacancies, decreased after illumination in such a manner consistent with a reduction in the number of vacancies. Samples with a reduced number of vacancies, or higher oxygen content, showed a smaller effect. The results support the notion that oxygen vacancies act as traps (F-centers) which weakly luminesce after illumination [29].

After illumination with visible light, if thin films of YBCO are exposed to infrared (IR) light, the resistivity shows a small increase, or is said to be partially quenched [30]. Figure 6 shows the observed quenching efficiency at 1330 nm (.93 eV) for a YBCO sample with $x \approx 0.2$. In other systems [31], this type of IR response after visible illumination is associated with the excitation of trapped carriers. A quenching effect of this nature would be predicted by the mechanism proposed for

photoluminescence. These results are consistent with the explanation given for the photoluminescence measurements [29]; trapped carriers in the chain layer allow the transfer of mobile holes to the CuO_2 planes. Unfortunately, the observed quenching efficiency, i.e. $\Delta R_{IR} / \Delta R_{vis} (\%)$, is far too small to be consistent with the large change in resistivity caused by illumination with visible light [30]. Additionally, it has been shown that if every vacancy trapped an electron, (in $\text{YBa}_2\text{Cu}_3\text{O}_{6+x}$ with $x < .4$), T_c should be raised from 0 K to 92 K [26], which has never been observed. (This conclusion is based the reported dependence of T_c on hole concentration [32], and one hole being transferred for each electron trapped.) However, it is difficult to explain the post-visible IR photoconductive response within the context of oxygen ordering models. Recent results [33] show that the response to IR light before visible illumination is to initiate the PPC state, yet illumination with 1 part in 10^5 of the visible photon dose required to saturate the PPC effect, causes the IR response to change dramatically. Wavelength and photon dose dependent measurements [33] support the idea that a broad distribution of defects, which populate quickly with respect to the other dynamics of PPC, could act as precursors to the oxygen ordering processes. A similar, but not related, model has already been proposed in which dipole fields that are induced by charge transfer cause rearrangement of basal plane oxygen [34]. However, the model predicts that PPC should occur in $\text{Bi}_2\text{Sr}_2\text{CaCu}_2\text{O}_{8+\delta}$ (BSCCO) which, to date, has not been observed [1].

Finally, we mention other experimental results which support a defect based model for PPC. When fast neutron irradiated thin films are illuminated with visible light the photoresponse becomes slightly larger [35]. Additionally, related work done

with over-doped materials shows that oxygen vacancies are a necessary ingredient to observe PPC in $\text{R}\text{Ba}_2\text{Cu}_3\text{O}_{6+x}$ and its (doped) rare-earth homologues [35].

Many normal state parameters have been observed to change in oxygen deficient YBCO as the result of illumination. Examples cited in Ref. [1] include the resistivity, c-axis length, Hall coefficient and mobility, resonant Raman peaks, and many more. An extended discussion of the experimental results and proposed models will be the subject of Chapter 2. In Chapter 5, we will return to the results obtained in Ref. [33] and the model proposed therein.

CHAPTER 2

PERSISTENT PHOTOCONDUCTIVITY IN $\text{YBa}_2\text{Cu}_3\text{O}_{6+x}$ THIN FILMS

2.1 Samples Studied

Most experimental studies on PPC in YBCO use thin film samples. There are several reasons for this. The first is that visible light has a penetration depth of about 1000 Å in [36] the visible region. Any photoinduced change in a macroscopically thick sample would be more difficult to detect than in a thin film. YBCO is also very brittle and it is difficult to grow large crystals. PPC has been observed in single crystals, and although the change in resistivity is small, if the sample is modeled as a composite of two resistors in parallel (one is the illuminated part, the other is the remainder) relative change in resistance is comparable to that of films [37]. The existence of a persistent change in resistivity in single crystals is convincing evidence that PPC cannot be written off as a grain boundary or stress/strain effect. It will be important to summarize the experimental results obtained on thin film samples in order to fully appreciate the many ways in which PPC has been characterized.

2.2 Experimental Observations

2.2.1 Changes in Normal State Resistivity

The first way in which PPC was characterized is the large change in resistance that occurs during illumination for oxygen deficient samples. At room temperature the lifetime of the photoinduced state is on the order of hours, while at low temperature it is essentially infinite. PPC has been observed in other systems, for example $\text{Al}_{1-x}\text{Ga}_x\text{As}$ [38, 39] with $x > .22$, but only at low temperature. Other systems exhibiting PPC will

briefly be discussed in Section 2.4.3. Studies on YBCO [23, 40] have shown that the functional dependence of resistivity on illumination time can be expressed as:

$$\rho(t) = \rho_{\infty} + (\rho_0 - \rho_{\infty}) \exp \left[- \left(\frac{t}{\tau_{ill}} \right)^{\beta_{ill}} \right], \quad (2.1)$$

where ρ_{∞} is the saturation value of the resistivity for $t \rightarrow \infty$, ρ_0 is the unilluminated value, τ is a time constant, and β is a ‘so-called’ dispersion parameter ($0 < \beta < 1$).

Similarly, the excess conductivity due to illumination decays at sufficiently high temperature:

$$\frac{\Delta\sigma(t)}{\Delta\sigma(0)} = \exp \left[- \left(\frac{t}{\tau_{rel}} \right)^{\beta_{rel}} \right], \quad (2.2)$$

$$\Delta\sigma(t) = \sigma(t) - \sigma_0.$$

The conductivity before illumination is σ_0 , and $\sigma(0)$ is the conductivity immediately after shutting off the light source. Stretched exponential decay is typically observed in systems with a distribution of time constants. β ranges between zero to one and represents the departure from exponential behavior. The relaxation time, τ , is determined from an Arrhenius plot [23, 40], as it is a thermally activated process.

$$\tau = \tau_0 \exp \left(\frac{\Delta}{kT} \right) \quad (2.3)$$

Although it is widely agreed that Δ is $\sim .9$ eV in YBCO, there is disagreement about the meaning of the dispersion parameter. Semiconducting YBCO samples [23] show β_{rel} increasing linearly with temperature while metallic samples [40] show a decrease of β_{rel} with temperature. This casts doubt on the interpretation [23] of $1-\beta$ as the measure of the width of a distribution of traps. However, measurements of the PPC

efficiency (generally defined as inversely proportional to the number of photons required to produce a given resistance change at a particular wavelength) on both sides of the metal-insulator transition indicate there is a common mechanism for the initiation of PPC in both metallic and insulating films. Although the absolute value of the PPC efficiency generally decreases with increasing x above the metal-insulator transition, the position of the spectral efficiency peaks do not change with x [41].

Whatever the interpretation of the dispersion parameters, it has been shown that PPC is only a function of visible photon dose, and not of incident power [23]. At low temperature, if the illumination is interrupted at any point, the resistivity will remain at that value until the illumination begins again. There are small changes that occur due to thermal effects when the light is turned on or off, but sample heating has been eliminated as a concern in studies of PPC. In most cases the thin films are immersed in liquid nitrogen during illumination, or an inert gas. Concerns about changing oxygen stoichiometry are then alleviated. PPC is a single photon process that cannot be explained as a thermal artifact.

2.2.2 Structural Changes

It has been observed that lattice parameters change under illumination. Fractional changes in the c -axis [24, 42] show the same functional dependence as the resistivity on illumination time. The c -axis contraction is attributed to a decrease in the Ba-Cu(1) distance after careful refinement of the x-ray data [24]. The same changes in structure were reported for room temperature annealing results in a $\text{YBa}_2\text{Cu}_3\text{O}_{6.41}$ ceramic sample [14]. Another indication of oxygen ordering during illumination are the XAFS results

in Ref. [25], where the bond lengths distribution between the Cu(1) – O(4) sites splits into two peaks upon illumination. These structural changes that occur after illumination strongly suggest that there is a link between the room temperature annealing and photoinduced phenomena. In fact, the changes in T_c and interplanar Ba-Cu(1) distance have essentially the same functional dependence on time during the room temperature annealing experiments as resistivity does during illumination [14]. Once again, the changes in the c-axis are inconsistent with, and evolve oppositely to, sample heating.

However, there is one difference that bears mentioning. At room temperature the metastable oxygen-disordered state slowly orders as determined by the increasing superconducting critical temperature and neutron diffraction results [15]. The PPC state will disorder after the light is shut off as determined by the relaxation of excess conductivity. One would be forced to posit the existence of a super-ordered state as the result of illumination to reconcile these seemingly contradictory observations.

Optical measurements in which the oxygen has been disordered without changing the oxygen content have served to reinforce the notion that, although the way in which the phenomenon of PPC and the oxygen disordered states relax is similar, the effects do not cancel each other out [43]. Changes in conductivity induced by heating $\text{GdBa}_2\text{Cu}_3\text{O}_{6+x}$ thin films, then quickly cooling, are compared with those caused by light at low temperature. The combined effect of disordering the basal plane oxygen and then illuminating the film is not the same as the sum of the separate effects. If the resistivity changes caused by light are deliberately matched with those caused by disorder at 150 K, then the films are cooled, T_c will be different from the unilluminated

equilibrium value. If the two effects really canceled each other out, T_c should be the same for films allowed to equilibrate at room temperature and then cooled, and for films whose oxygen is disordered and then illuminated. A comparison of the Arrhenius plots for relaxation times yields a barrier of .85 eV for the disordering process and .9 eV for the relaxation of the excess conductivity caused by illumination. The relaxation time for the disordering process is almost an order of magnitude larger than the PPC relaxation. The exponent, β , shows essentially the same behavior for both processes [43]. So, although the processes leading to relaxation are similar, if not the same, the initiation of the PPC effect cannot be explained in terms of oxygen ordering in the basal plane.

Measurements in the IR have linked the growth of the average chain length and the initiation of PPC [44]. The authors attempt to explain AC conductivity found by optical conductivity measurements in a region of the phase diagram where DC measurements yield insulating behavior. The zero frequency extrapolation for reflectivity measurements yields a finite conductivity for $\text{YBa}_2\text{Cu}_3\text{O}_{6.2}$. For oxygen contents less than 6.2, extrapolation to zero frequency yield zero conductivity as expected. A percolation model is proposed in explanation of this phenomenon [44]. The chains are treated as spherical metallic particles embedded in an insulating matrix. The dielectric function for fully deoxygenated $\text{YBa}_2\text{Cu}_3\text{O}_x$ ($x = 6.0$) is used to represent the insulating matrix. At some critical point in the phase diagram the metallic particles begin to touch each other and form a percolation path. The transition to overall metallic behavior occurs close to the metal/insulator transition and the orthorhombic/tetragonal structural phase transition ($x = 6.35$). Despite excellent agreement between optical

measurements of films with extremely low oxygen contents ($x = 6.1, 6.2$) and numerical calculations, the model remains somewhat problematic in that it no longer applies once the transition to overall metallic behavior occurs. A more complete description would require a formidable calculation for higher oxygen contents ($x > 6.3$) and would not allow the model to remain as simple, i.e. metallic particles in an insulating matrix. However, it must be noted that the authors establish a strong correlation between chain length and the optical properties including PPC. To do this, the samples are heated to well above 300 K (300° C), thereby shortening the chain length while not altering the oxygen content. A lower free carrier concentration is evident from a reduction of the spectral weight in the mid-infrared reflectivity, along with a small blueshift in the peaks. The chain length as a function of temperature is already known from an Arrhenius plot. When PPC is initiated through exposure to visible light the opposite evolution occurs. There is an increase of spectral weight in the mid-infrared and a redshift in the peaks. This yields convincing evidence that growth of the average chain length is correlated with the initiation of the PPC state.

2.2.3 Changes in Transport

The Hall coefficient, R_H , also has the same functional dependence upon illumination time as does the resistivity [45]. The simplest possible interpretation is that of the one-band picture. In this case, the Hall coefficient is inversely proportional to the number of free carriers. The decrease in the Hall coefficient with illumination is seen as direct

evidence of photodoping. The Hall mobility, $\mu_H = \frac{R_H}{\rho}$, has more complicated

behavior. At room temperature, while R_H and ρ decrease, μ_H increases [45]. At low

temperatures, μ_H has been reported to increase while R_H and ρ both decrease [1].

Interpreting the meaning of these results becomes more difficult. A linear planar Hall effect has been reported for a-axis oriented $\text{EuBa}_2\text{Cu}_3\text{O}_{6.5}$ films [28]. That is, samples with the current, measured electrical field, and magnetic field all in the same plane still showed a measurable transverse voltage which is linear in the magnetic field. The Lorentz force is zero in this case, so the observed effect is not well understood. Measurements of the conventional Hall effect do not offer any insight, other than to reinforce the idea that it is extremely difficult to extract meaningful results from measurements of parameters like μ in this complex material. Such experiments tend to give results suitable for post-diction rather than prediction.

2.2.4 Spectral Efficiency

A natural question that may arise, is, how efficient is a particular wavelength in initiating PPC? It was originally reported that there was a threshold at 1.6 eV, photon energies below this would not cause PPC [23]. The spectrum was measured out to 3.3 eV, and the peaks in the spectrum were assigned to transitions within the CuO_2 planes. Several points bear mentioning. In the first study, the efficiency, η , is defined as:

$$\eta(\omega) = \frac{1}{R(0)} \left. \frac{dR(t)}{dt} \right|_{t=0} \frac{1}{N_{ph}(\omega)}. \quad (2.4)$$

$N_{ph}(\omega)$ is the flux density of photons of energy $\hbar\omega$, and R is the film resistance. The spectrum is obtained by illuminating with a broadband source through a monochromator. The power level is very low, peaking at $.4 \text{ mW/cm}^2$. The resistance of the film is continuously recorded as a function of time. After a time of $\Delta t = 1$

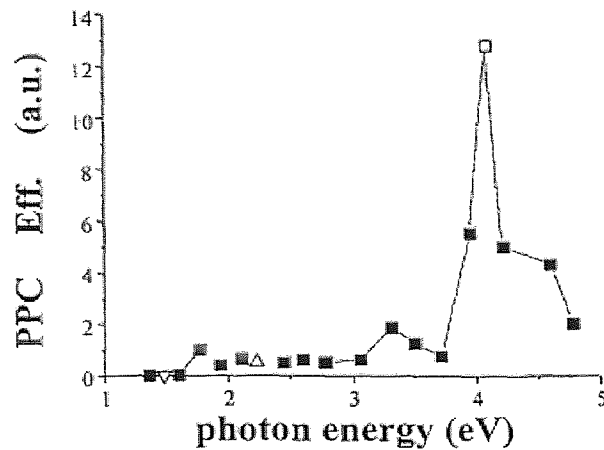


Figure 7 PPC Spectral Efficiency – note large enhancement at 4.1 eV. Adapted from Ref. [46].

minute, the wavelength is incremented in units of 5 nm. $\eta(\omega)$ is constructed from the slopes of straight line segments at wavelength step. Subsequent studies extend the energy range out to 4.8 eV, with a large enhancement at 4.1 eV [46]. The efficiency shown in Figure 7 is defined differently, but the meaning is generally the same. The 4.1 eV peak is associated with a particular¹ transition in an O(4)-Cu(1)-O(4) dumbbell in the chains [47]. These Cu(1)⁺¹ sites have oxygen vacancies on either side. One interpretation of these results is that creating an electron-hole pair in close proximity to an oxygen vacancy enhances the probability for electron capture, thus supporting a trapping model for PPC [29, 46].

Real time, *in situ* ellipsometry measurements have shown that there is enhanced absorption at 4.1 eV and this absorption is correlated with oxygen deficiency [48]. The ellipsometric variables were monitored in a rapid thermal processing chamber during

¹ $3d_{3z^2-1} \rightarrow 4p_x$

both pure oxygen and vacuum anneals. Ellipsometry allows for sensitive determination of the oxygen content as well as diffusion coefficients. As an interesting side note, it was found that the mechanisms for oxygen in- and out diffusion are different. This is yet another result which serves to highlight the importance and complicated nature of the motion of oxygen in $RBa_2Cu_3O_{6+x}$. The correlation of this enhanced absorption with oxygen deficiency tends to support the interpretation given of the PPC efficiency results given above [46].

One caveat applies to these results. In all of the measurements reviewed in Ref [1], it is said that there are almost no PPC effects below 1.55 eV (800 nm). In fact, this is not the case. Recent results show that, for even extremely small photon doses in the visible, the response to IR light dramatically changes [33]. In the measurements of the spectral efficiency cited above, it is possible that during alignment, the films were illuminated with enough visible photon dose to saturate the response to IR. Alternatively, the measurements could have begun in the UV, and by the time the monochromator had stepped through to the IR, the response to IR light had totally changed. It has been shown that for photon energies as low as .93 eV (1330 nm) PPC is initiated [33]. However, if the film is illuminated with as little as 10^{18} photons, IR light partially quenches the PPC state. Comparing this to the saturation dose of $\sim 10^{23}$, it is easy to see why this may have been overlooked. These results will be discussed in more detail in Chapter 5.

Photoluminescence measurements (discussed in Section 1.5.2) [29] establish a correlation between peaks in the PPC efficiency spectrum and the photoluminescence spectrum, while photoconductivity measurements indicate that the light induced

changes in mobility may play a role in the PPC effect [27]. It is surmised that the changes in mobility might be related to the changes in the lattice. Earlier objections that are raised to a trapping model are countered with the argument that they do not include the effect of the changes in mobility and the lattice. Recall that it has been claimed that if every vacancy trapped an electron, transferring a hole to the planes, then it should be possible to raise T_c from 0 K to 92 K [26], although such an objection ignores the structural changes that occur due to trapping, along with changes in mobility.

2.2.5 Role of Oxygen Deficiency and Doping State

Other important results that have been mentioned are the absence of PPC in $Y_{1-x}Ca_xBa_2Cu_3O_{6+x}$ unless the material is oxygen deficient [35, 49]. The Ca substituted films introduce holes to the CuO_2 planes. This allows the material to become superconducting for oxygen contents well below the metal/insulator transition in $YBa_2Cu_3O_{6+x}$ [50]. In general, high T_c materials are characterized as overdoped ($\frac{\partial T_c}{\partial n} < 0$) or underdoped ($\frac{\partial T_c}{\partial n} > 0$) with respect to an increase in the free carrier concentration, n . In the case of Ca-doped films, PPC effects occur in both cases of over- and underdoped films. In both cases the conductivity always increases, while T_c can either increase or decrease. Other dopants are discussed [1], and it is concluded that oxygen vacancies are necessary for PPC to occur.

The observation of PPC in $Tl_2Ba_2CuO_{6+x}$ (Tl2201) shows that chain layers are not a necessary ingredient for PPC to occur [51] in the High- T_c compounds. T_c in this compound can be varied from 85 K to 0 K by *adding* oxygen [52]. Therefore, Tl2201

is in the overdoped regime. The PPC effects in Tl2201, though very small, are fully quenchable with IR light [51]. Unlike $R\text{Ba}_2\text{Cu}_3\text{O}_{6+x}$, illuminating Tl2201 can lead to an increase in normal state resistivity without prior exposure to visible light. However, the PPC effects in Tl2201 decay at a much faster rate and are much smaller in magnitude. Even at 30 K, the photoinduced state slowly decays [51]. This is in complete contrast to $R\text{Ba}_2\text{Cu}_3\text{O}_{6+x}$, where no relaxation is observed below 100 K, and implies a different trap distribution in Tl-based compounds.

Whatever one may think about the trapping mechanisms proposed for PPC in Tl2201, one must acknowledge that it is extremely difficult to propose an oxygen ordering scheme to explain the experimental observations. One would be forced to accept that one wavelength would cause oxygen to move in such a way as to increase the conductivity, and another wavelength would result in oxygen motion that would lower the conductivity. As such reasoning relates to $R\text{Ba}_2\text{Cu}_3\text{O}_{6+x}$, the initiation of PPC would order the lattice, and subsequent illumination with IR radiation would disorder the lattice. Also, a small amount of illumination with visible light, far below the saturation dose, will order the lattice in such a way as to cause IR radiation to disorder it. However, prior to this small visible photon dose, IR photons result in PPC.

2.2.6 Resonant Raman Scattering

One area that has recently attracted attention is resonant Raman scattering (RRS) experiments with both films and crystals. It is claimed that such experiments can give direct evidence of photo-assisted oxygen ordering [53] as a potential mechanism for PPC. Experiments are done on $\text{GdBa}_2\text{Cu}_3\text{O}_x$ thin films. The authors identify two sets

of lines in the Raman spectrum that become active due to loss of inversion symmetry. These modes are associated with Cu and O sites in short chain fragments. One line that is associated with monomer chain fragments bleaches during illumination and gives evidence of oxygen ordering. These modes are not Raman active for oxygen contents near the ortho-I and ortho-II phases because there is inversion symmetry for the long chains. Spectral features are identified as having a relationship with chain length, then the oxygen is thermally and reversibly disordered without changing the oxygen content. Those features correlated with chain length are observed to decrease with thermal disorder, thus providing evidence that oxygen ordering occurs during illumination. In addition, the ortho-I and ortho-II phases do not exhibit the bleaching effect.

These results are part of a larger body of work that began on fully oxygenated YBCO [54]. A resonance phenomenon was identified at 2.2 eV with normally forbidden lines appearing at 232 cm^{-1} and 597 cm^{-1} . Subsequent work has identified ortho-III² correlations as having an important relationship with RRS [55]. The strength of the resonance, defined as the Raman intensity of the 230 cm^{-1} to 340 cm^{-1} mode is about an order of magnitude larger than in fully oxygenated YBCO. The authors fit the intensity of the 230 cm^{-1} mode during illumination to stretched exponential decay time dependence. Remarkably, there are similar fit parameters to those for PPC [23, 40]. In another study on crystals with T_c varying from 57-70 K [56], the same Raman intensity is fitted with exponential decay during illumination time. Although the RRS phenomenon is certainly interesting, its relationship to PPC is unclear at best. RRS exists for fully oxygenated YBCO, and the resonance line has no clear relationship to the PPC efficiency spectrum. This phenomenon has been observed [55] for YBCO

(6.35→6.5), albeit at much reduced strength. Here the PPC effect is the large, just on the other side of the metal insulator transition. The bleaching also occurs at a much lower photon dose than the PPC effect saturates [55, 56], so unless the phenomena are related, but on different time scales there is no clear connection. Yet we have chosen to mention it, because several authors have proposed in the literature that there is a relationship between PPC and RRS. There may well be such a connection, but it does not seem to be sufficiently clear yet to qualify as an explanation for PPC [53, 55].

Having reviewed the experimental work done on High T_c materials exhibiting PPC, the next task will be to examine proposed mechanisms. First, a brief discussion concerning microstructure and morphology will be given. For the interested reader, a thorough review of the experimental work is given in Ref. [1].

2.3 Microstructure and Morphology

Despite the remarkable parallels between the basal plane ordering process that enhances T_c in quenched samples [13], and the dynamics of PPC [26], it is clear that there are different mechanisms responsible for each. Measurements on films whose oxygen has reversibly been disordered, then illuminated at low temperature, show that the illumination and oxygen disordering are not inverse processes [43]. Furthermore, the underlying mechanism of oxygen ordering is far from understood, as can be gleaned from recent theoretical work [57]. In single crystal $YBa_2Cu_3O_{6.4}$, observation by ultra-high resolution electron microscopy of the distribution of basal plane oxygen atoms confirms that the microstructure is quite complex [58, 59]. In areas of roughly 100 Å in

² alternating two full chains with one empty

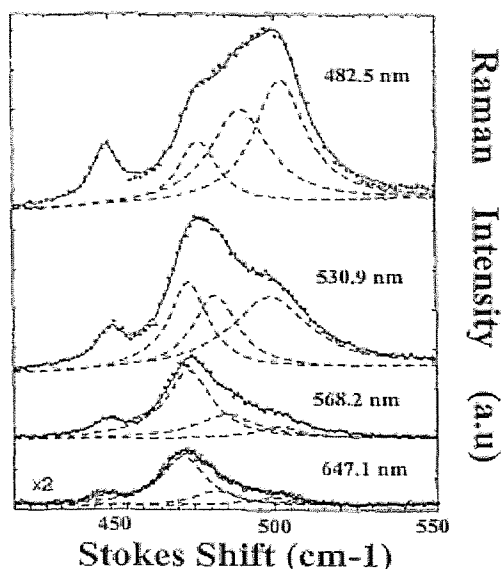


Figure 8 O(4) Raman mode for several exciting wavelengths. Note three separate contributions. Adapted from Ref. [60].

diameter, local regions of fully oxygenated $\text{YBa}_2\text{Cu}_3\text{O}_{6+x}$ were observed, while in other regions of similar size the O(1) and O(5) sublattices were found to be empty. The areas of fully oxygenated material can be broken down into smaller regions that are close packed with cluster size 8-30 Å. Additionally, neighboring basal planes were found to have only partial correlation in terms of their oxygen distributions. Resonant Raman scattering measurements on single crystal $\text{YBa}_2\text{Cu}_3\text{O}_{6.4}$ serve as additional confirmation of these results [60]. At low temperature, the well known O(4) band was decomposed into several Lorentzians, each of which can be assigned to tetragonal ($\text{YBa}_2\text{Cu}_3\text{O}_6$), ortho-I, or ortho-II YBCO. Figure 8 shows the results of the decomposition, with the three contributions clearly indicated. The authors interpret this as evidence for the co-existence of several phases within the same crystal, similar to that reported in the microstructure studies [58,59]. A final complicating factor that needs to be considered

when dealing with thin films is the presence of grains. Films grown on LaAlO_3 (LAO) are the most common because of the highly oriented nature of films [61]. Although the c -axis of the film can be made perpendicular to the substrate plane, the in-plane epitaxy is hard to control because of the twinned nature of the substrate [62]. So, although the film is oriented with respect to the c -axis, the a - and b -axis show no particular orientation. The picture that we are left with is quite muddy. Not only can the oxygen content vary in regions on the order of 10's of lattice spacings, but, in films, these clusters can be within grains. So, given these observations concerning microstructure and morphology, the likelihood of a global ordering process as a mechanism for PPC in thin films of YBCO seems to seriously diminish. Nevertheless, we will now examine the various mechanisms proposed to explain PPC and PISC in $\text{RBa}_2\text{Cu}_3\text{O}_{6+x}$.

2.4 Proposed Mechanisms for Persistent Photoconductivity

2.4.1 Oxygen Ordering Mechanisms

First, we will review the models that fall under the general heading of oxygen ordering. The basic premise of such models is that the increase in conductivity and T_c along with the contraction of the c -axis that occurs after illumination of oxygen deficient $\text{RBa}_2\text{Cu}_3\text{O}_{6+x}$ mimic those changes that occur by adding oxygen. The first example is known as the photoinduced oxygen diffusion model [23]. An oxygen atom occupying an O(5) site absorbs a photon and in an excited state jumps into a O(1) site. A schematic is shown in Figure 9, along with the associated double well potential for the oxygen atom. Given sufficient thermal energy the oxygen atoms will eventually relax and begin to repopulate the O(5) sublattice. Once the oxygen atoms lengthen the chain

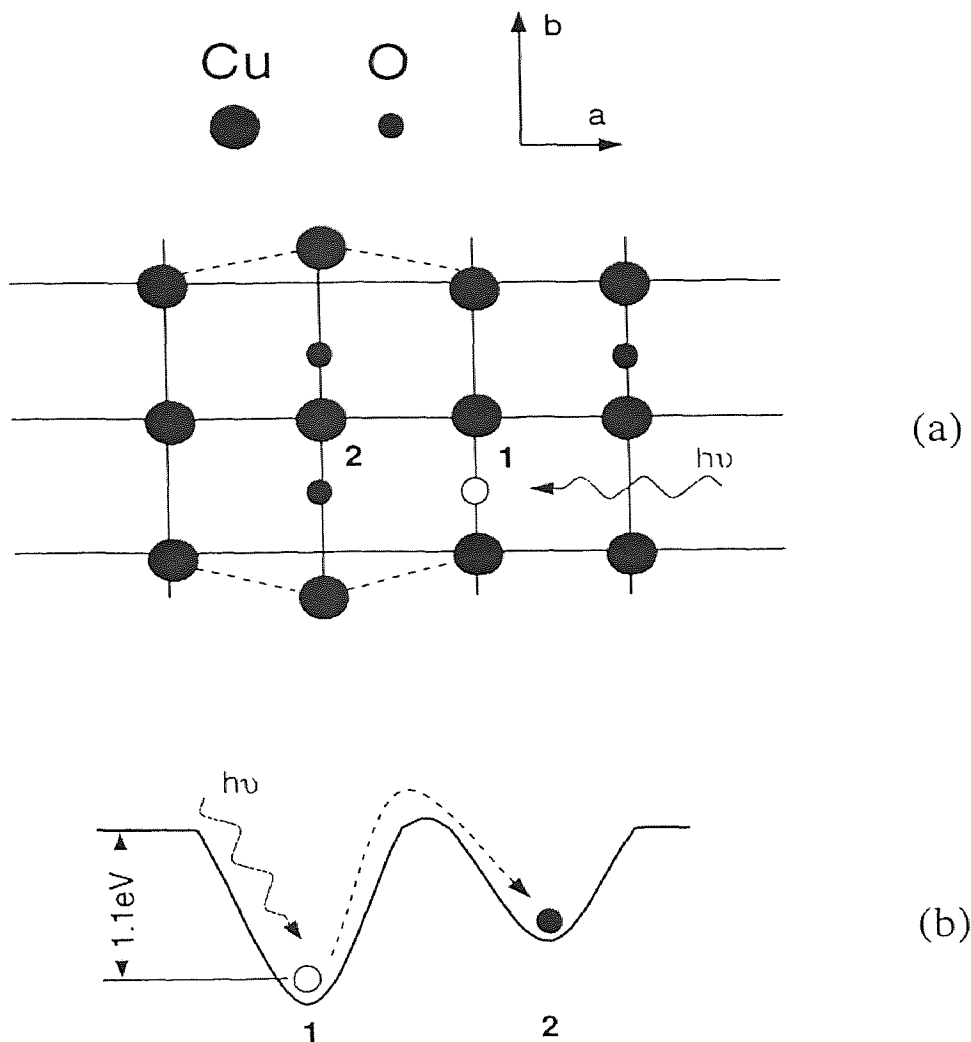


Figure 9 (a) Photoinduced diffusion model – upon photoexcitation oxygen moves from position 1 \rightarrow 2 in diagram. Shows resulting orthorhombic distortion. (b) Associated double well potential. Adapted from Ref. [23, 35].

fragments sufficiently, the chains will ‘inject’ holes into the CuO_2 planes as discussed in Chapter 1. While this model accounts for the light induced orthorhombic distortion, it fails to explain the enhancement [27, 28] of PPC below the metal-insulator transition. A simple statistical calculation [27, 28] shows that a random distribution of oxygen atoms in the basal plane for the tetragonal phase, yields an insufficient population of

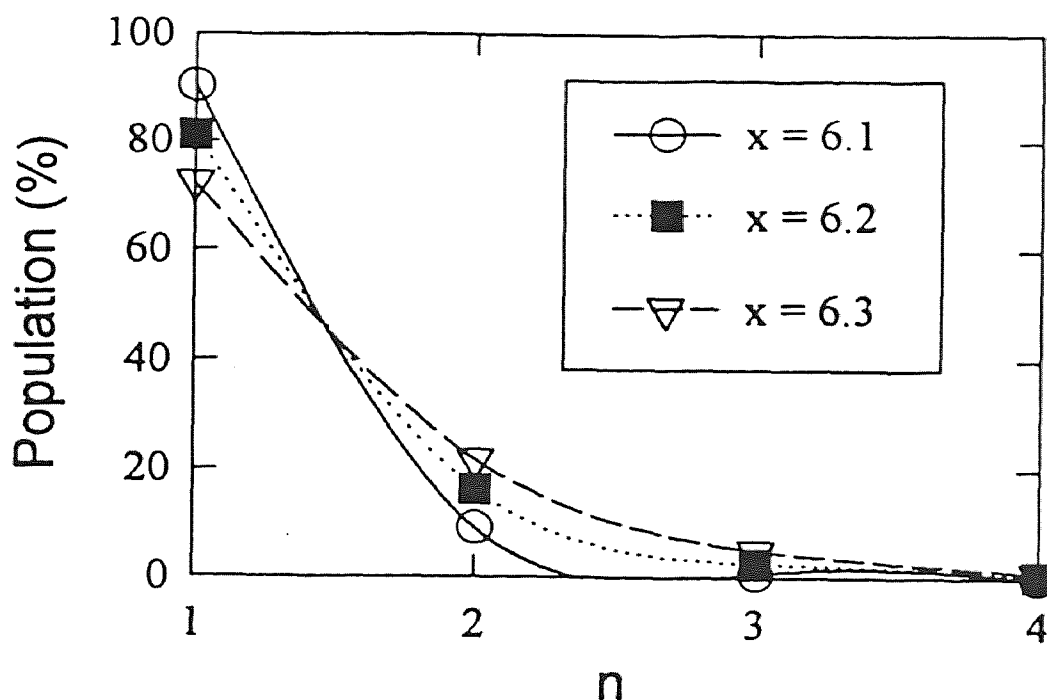


Figure 10 Percentage of basal plane oxygen atoms in chains of various length. Adapted from Ref. [27].

chain lengths required for injection of holes into the CuO_2 planes. It has been shown that the average chain length required to inject holes is between three and four [63]. Figure 10 shows the results of the calculation, giving the relative populations of various chain lengths, where n is the length of a given chain. As the oxygen content is decreased below the metal-insulator transition, the probability becomes negligible that oxygen migration from the O(5) sublattice into the O(1) sublattice will cause the growth of chain fragments of sufficient length to inject holes. Therefore, this model predicts that the PPC effects should decrease with decreasing oxygen stoichiometry in disagreement with experimental results [1, 23, 27, 28, 29, 33].

In examining the results of Figure 10, it may be helpful to briefly review the definition of chain fragments of various lengths. For example, in the sequence V-Cu-O-Cu-O-V, we have the representation of a fragment of length $n = 2$ where V is an oxygen vacancy, O represents an oxygen atom, and Cu represents an atom. The designation of the site “(1),” as in Cu(1) has been omitted for clarity. Similarly, V-Cu-O-Cu-O-Cu-O-V represents a fragment of length $n = 3$.

A related model is the photoinduced charge transfer mechanism [23]. Consider a chain fragment of length n . Fragments of $n \geq 2$ in a sample with oxygen content less than 6.4, have 1 $O^{\cdot -}$ and $(n-1) O^{\cdot}$ ions [63]. It is proposed that during illumination photogenerated electrons get trapped in unoccupied p-levels in monovalent O, while holes will be transferred to the planes. Since this model predicts that the effect should be proportional to the number of fragments with $n \geq 2$, it is inconsistent with the result shown in Figure 10.

The photoassisted oxygen ordering model asserts that electron-hole pairs created during illumination result in a modification of local fields such that it becomes advantageous for oxygen atoms occupying O(5) occupied sites to jump to neighboring unoccupied O(1) sites within chain fragments [26]. This ‘redistribution’ of fields, and consequent oxygen-ordering, occurs when a Cu^{+2} site neighboring an occupied O(5) site captures a photogenerated electron, converting its valence to Cu^{+1} . This allows the transfer of a hole to the CuO_2 planes. Although this model seems to successfully explain the enhancement of T_c (see Figure 5) that occurs due to illumination, it has difficulty explaining the PPC results obtained on Tl2201 [51], also discussed in Section 2.2.5.

2.4.2 Theoretical Considerations Concerning Oxygen Ordering

Finally, some theoretical considerations concerning the photoassisted oxygen-ordering model bear mentioning. To facilitate this, we will review some general considerations involved with the modeling of the structural phase diagram. The most common theoretical description is based upon the asymmetric next-nearest-neighbor Ising model (ASYNNNI) [64]. The basic Hamiltonian is given [34]:

$$H_0 = V_1 \sum_{NN} n_i^k n_j^l + V_2 \sum_{\substack{NNN \\ (Cu)}} n_i^k n_j^k + V_3 \sum_{NNN} n_i^k n_j^k - \mu \sum_i n_i^k \quad (2.5)$$

Figure 11 shows the various interaction terms in the Hamiltonian as well as the two separate O(1) sublattices in the O-II phase. The sums run over indices $k, l = O(1)_1, O(1)_2$ and O(5) sublattices. The occupation numbers, n , assume values 0 or 1. The interaction term V_1 represents the repulsive nearest-neighbor oxygen-oxygen potential, i.e. between an occupied O(5) and an occupied O(1) site. The term V_2 represents an attractive interaction ‘in-line’ when oxygen atoms have Cu sites between them. The repulsive term V_3 can be understood as the energy loss due to a threefold coordinated Cu site at the end of a chain fragment. Typically, one gains information about temperature dependent behavior of the system by calculation of the grand canonical potential.

One criticism of this model is the lack of inclusion of fermionic degrees of freedom, thus effectively limiting the range of interaction [65]. To accommodate longer range interactions, the Hamiltonian may be recast in terms of an Ising spin variable, using $n_i = \frac{(1-\sigma_i)}{2}$. Such a lattice gas model has been applied to the O-I phase

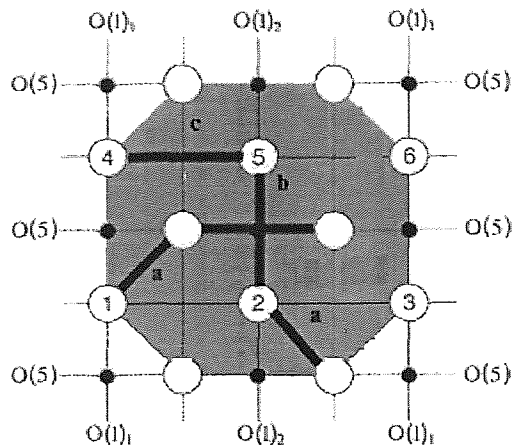


Figure 11 Schematic of interactions included in ASYNNNI model for O-II phase. Thick lines connecting sites indicate interactions – (a) V_1 , (b) V_2 , (c) V_3 . Adapted from Ref. [34].

in which nearest-neighbor oxygen sites interact antiferromagnetically [66]. Next-nearest-neighbor sites interact attractively if separated by a Cu site, or repulsively otherwise. It has been shown that such a model can explain some features in the phase diagram, and some aspects of oxygen ordering [66]. Within reasonable accuracy the O-I \rightarrow T line in the phase diagram can be constructed. One important feature of the model is the sublattice dependent chemical potential. It is noted that the application of uniaxial stress during crystal growth lessens or mitigates the effect of twinning [67]. By appropriate choice of the chemical potential, one could favor the population of one sublattice at the expense of the other. In the authors' language, the degeneracy of the twinned structure is removed. However, the success of the model was limited in attempts to similarly model the O-II phase. The ASYNNNI model fails to properly predict the O-I \rightarrow O-II transition temperature, placing it substantially closer to the O-I \rightarrow T transition line in the phase diagram than it actually is [65]. Additionally, it

predicts long range order to exist in the O-II phase, which is not evident experimentally. It is concluded that the ASYNNNI model gives adequate description of the ordering dynamics in the O-I phase but fails when the O-II phase is approached [65]. However, this has not prevented attempts to rehabilitate the model with the inclusion of additional parameters [68, 69].

In the first such study [68], the addition of a 3-D coupling term to describe weak correlation between the CuO_x chains is investigated. The phase diagram is not altered, but there is a large change in the transition temperature. Even with the inclusion of this term there is still unsatisfactory agreement with the experimentally observed temperature gap in the $\text{O-I} \rightarrow \text{O-II}$ and $\text{O-I} \rightarrow \text{T}$ phase transitions.

In an attempt to include long-range interactions between oxygen sites, an extra repulsive term (V_5) is added which couples sites *not* bridged by a Cu site *and* two lattice parameters apart [69]. By choosing V_5 carefully, this additional parameter can be tuned to 'turn on' only after the chains have begun to form. The value of V_5/V_1 is chosen to be .02 +/- .02. The upper limit of this parameter causes O-III correlations to appear in the phase diagram where they are not observed experimentally. The calculation yields reasonable results for the temperature differential spoken of before between the boundary lines in the structural phase transition. Experimentally, one observes, $\Delta T = 250$ K, the calculation yields $\Delta T = 170$ K. There is modest success in identifying O-III correlations in the simulated structure factor. These new results indicate that successful modeling of the basal plane will include some 3D interaction between planes, and some longer range interactions. However, terms describing longer range interactions will be significant only in regions of the phase diagram where

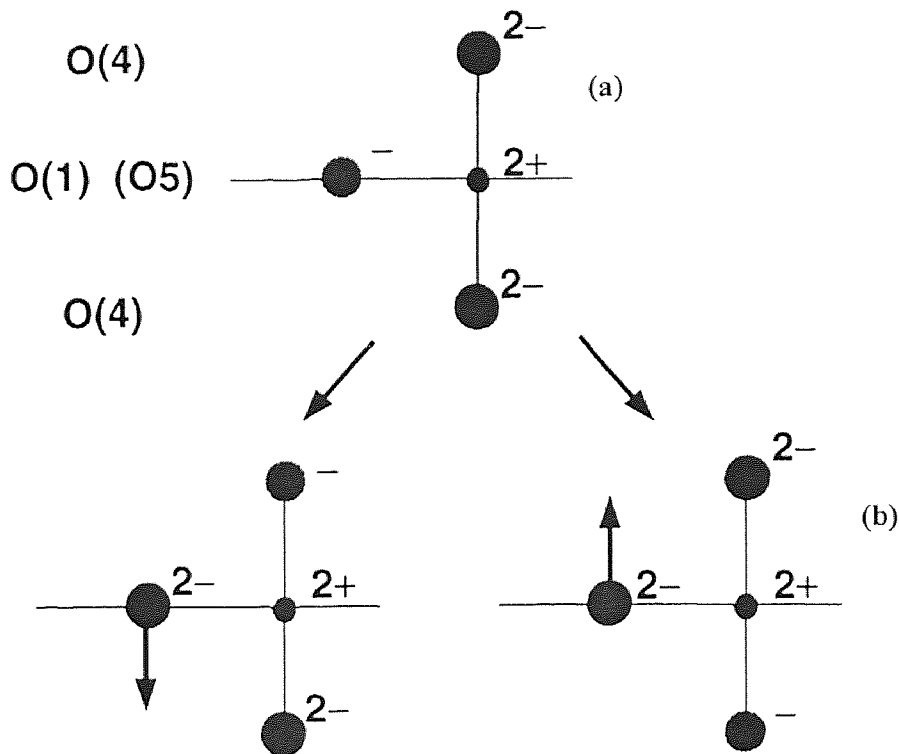


Figure 12 Polarization of chains through dipole formation. (a) O(1) site has -1 valence (b) transfer of an electron (charge transfer) from O(4) site results in dipole moment on O(1) site. Adapted from Ref. [35].

oxygen is 'frozen-in'. The authors have yet to map out the phase diagram based upon their modified ASYNNNI, but soon to be published work provide the necessary experimental results to do so [70].

This reasoning leads us to a discussion of a particular application of the ASYNNNI model to PPC [34]. This model proposes the addition of a dipole term to the Hamiltonian (2.5), which leads to a renormalization of the chemical potential, and the basal plane structural changes. In particular, the region of the phase diagram near the metal-insulator transition is concentrated upon. Recall that this is where the largest enhancement of T_c is observed upon illumination.

The basic mechanism that is presumed to result in basal plane order is charge transfer, with consequent formation of dipole moments on fourfold coordinated chain oxygen sites. As shown in Figure 12, the dipole is formed when a monovalent chain site oxygen somehow transfers a hole to the CuO_2 planes via an O(4) site. The charges on each ion are adjusted to convert monovalent chain oxygens into divalent ions. A dipole cannot form near a chain end because the valence of threefold coordinated oxygen is -2 , thus inhibiting the charge transfer process. If enough charge transfer occurs, the chains will become polarized. This polarization will lead to renormalization of the chemical potential, and consequently, oxygen ordering.

The model uses the Hamiltonian (2.5) plus an additional term to describe the effect of the ‘induced’ dipoles:

$$H_E = -\sum_k \Delta G_k(\varepsilon) \sum_i n_i^k. \quad (2.6)$$

$\Delta G(\varepsilon)$ is the change in the Gibbs energy as the result of the Ising field, $\varepsilon = E \cdot p_0$. The fields are considered to be small, and the Gibbs energy can be written in terms of the susceptibility and Ising field. If the dipole strength, p_0 can be estimated properly or obtained from experiment, the model can be written as having only one free parameter: J , the dipole interaction strength.

The aim is to obtain correlation functions from Figure 11 consistent with the Hamiltonian (modified by equation 2.6), thus constructing the light-induced enhancement of the percolation path, and therefore, T_c . The relationship between T_c and the percolation path is given [71]:

$$T_c(x) = T_c^{\max} \left[1 - \left(\frac{\xi_0}{d(x)} \right)^2 \right]. \quad (2.7)$$

$d(x)$ is the minimal width of the percolation path, the threshold for superconductivity. It is related to the correlation functions gleaned from the Hamiltonian. ξ_0 is a correlation length, presumably of a Cooper pair. This relationship is interesting, because provided with $T_c^{\max} = 92$ K, it gives the two plateau dependence of T_c on oxygen content, x .

Several features of the model bear mentioning. First, it bears some resemblance to the work in which a sublattice dependent chemical potential was used to mimic the effects of uniaxial stress [66]. The transition temperature was found to vary with the chemical potential in a small way. The authors of the current model were apparently unaware of this result and make no mention of it [34]. A key result was that the model fails to work properly in the O-II region of the phase diagram. Even with the chemical potential so formulated, the degeneracy of the O-II \rightarrow T line is not removed with respect to the O-I \rightarrow T line in the phase diagram. To remove this degeneracy, long range interactions need to be added [65, 68, 69, 70]. The reason that this cannot be ignored in the dipole induced reordering model [34], is that it depends so intimately on the dynamics of the O-II phase, and the Hamiltonian (2.5) has been shown to inadequately describe the O-II phase.

Another difficulty for the model is that it predicts the enhancement of T_c is smaller if the sample is illuminated at a lower equilibrium temperature than room temperature [34]. This is at odds with the myriad of PPC results which show various effects are larger in magnitude below room temperature.

2.4.3 Defects in the Chain Sites

The stability of defect O(1) sites is a prerequisite for the vacancy capture model. It has been shown that such sites may exist [72], and if so, are stable [73]. A reasonable defect based mechanism purporting to explain PPC must depend on intrinsic defects. It is important not to rely on extrinsic defects like grain boundary effects because PPC has been observed in single crystal specimens of high quality in which grain boundary effects should be negligible [37]. Other materials exhibit PPC, such as $\text{Al}_{1-x}\text{Ga}_x\text{As}$. The PPC in these materials is typically with DX centers³, deep trap levels that are associated with donors [38]. The thermal ionization energy and optical ionization energy are quite different, indicating that the lattice is strongly coupled to the DX level. Experiments with other materials have confirmed that this is indeed an intrinsic effect.

Both CdS and ZnS films in the photoconductive state can be optically quenched with IR radiation [74]. A simple model is presented for these results in which an electron-hole pair is initially created by bandgap radiation. The hole becomes trapped at a 'sensitizing' center, with a large capture cross-section for a hole when occupied by an electron, but a small capture cross-section for an electron when occupied by a hole. The ratio of these two capture cross-sections is the order of 10^6 . Then IR radiation may excite a hole directly into the valence band where it will undergo recombination, or to the upper level of the sensitizing center where it may be thermally activated into the valence band. There are alternative explanations offered for systems other than CdS and ZnS, and there is rich literature on the subject [38], but the most commonly accepted mechanism for PPC in III-V and II-VI materials is lattice relaxation accompanying the formation of DX centers. This lattice relaxation is large enough such

that it compensates for the trapping of two electrons. Such a trap is called a negative U-center, where U is the Hubbard correlation energy. The correlation energy is negative when the trapping of a second electron reduces the deep energy level, more than compensating for the on site repulsion between the pair [38]. More recent work on materials in which an electron gas is confined to two dimensions and couples with local moments [75], indicate that this is the likely explanation for PPC. In this case heterostructures are formed in which quantum wells are confined between n -doped barriers. Then PPC is understood to occur when the populated deep levels are photoionized at sufficiently low temperatures, the electrons are excited into the conduction band, and the conductivity is enhanced. In this case, doping with manganese leads to a narrowing of the trap, resulting in an effective repulsive barrier for recombination. The relaxation of PPC can be fit with stretched exponential decay dependence on time. These cases contrast with PPC observed in the $R\text{Ba}_2\text{Cu}_3\text{O}_{6+x}$ homologues. In the case of III-V and II-VI materials, electrons are trapped in deep levels to begin with, and then are excited to the conduction band. In optical quenching studies [74], IR radiation is said to release a trapped hole to the valence band where it can be trapped by a center with a large capture cross section for an electron. There is also the possibility of exciting an hole from a lower to a higher trapped level where it can be thermally activated. Both of these processes contrast with the vacancy capture mechanism, whereby electrons are trapped at oxygen vacancies in the chain sites. Such vacancies can be filled by two electrons, in which case they are called F centers. Alternatively they may trap one electron, and are known as F^+ centers. Theoretical calculations concerning stability indicate the oxygen vacancies are F^+ centers [72]. So,

³ “D” stands for Donor, “X” for unknown lattice defect

given the differences between PPC that is observed in III-V and II-VI materials, and $R\text{Ba}_2\text{Cu}_3\text{O}_{6+x}$ it is unlikely that the explanation for PPC in high- T_c materials will bear more than qualitative resemblance.

2.4.4 Polarons and Photomodulation Spectroscopy

Photomodulation spectroscopy is a useful optical technique in which above-bandgap radiation is allowed to excite carriers and fractional changes in the IR transmission are monitored. Early work on the optical properties of $R\text{Ba}_2\text{Cu}_3\text{O}_{6+x}$ and related materials focused on the possibility of uncovering a polaron pairing mechanism for superconductivity. When ceramic samples, ground and mixed with KBr, were illuminated with laser light it was discovered that there was a change in the IR spectra as evidenced by $\Delta T/T$, where T is the transmission [76]. This is a useful technique because thermal artifacts, if present, would appear as derivative shaped signals in $\Delta T/T$. Also, any effects arising from metallic particles embedded in an insulating medium, i.e. ‘effective medium’, would have a one-to-one correlation between $\Delta T/T$ and T . Neither of these two common artifacts appear in the results of Ref. [76]. When an insulating material is used, the photoinduced conductivity, $\sigma_p(\omega)$, may be written as:

$$\sigma_p(\omega) = \frac{nc}{4\pi d} \left(-\frac{\Delta T}{T} \right) \quad (2.8)$$

where ω is the photon energy, d is the absorption coefficient, n is the refractive index, and c is the speed of light. So, mindful of these potential artifacts, one can correctly interpret $-\Delta T/T$ not consistent with these features as genuine photoinduced absorption (PIA). A detailed comparison of the PIA and phonon bleaching yielded interesting

results. First, a broad electronic absorption occurs at .13 eV, the nature of which is not immediately clear. Second, it is observed that bleaching occurs for IR active vibrational (IRAV) modes that are associated with the tetragonal structure, while the photoinduced IRAV modes occur for Raman modes of the tetragonal phase that are in 1:1 correspondence with the orthorhombic phase. This leads the authors to conclude that photogenerated charge carriers somehow distort the local structure, converting it from tetragonal to orthorhombic. It is important to note that these local structure modifications occur on a short time scale when compared with PPC. The fractional changes in the c-axis induced by PPC require illumination with approximately 60 W/cm² power density for 1 1/2 hours to saturate, whereas the local structure changes appear immediately upon illumination with 40 mW/cm² [77]. Furthermore, the PIA and bleached modes identified are associated with the Cu(1), O(1), and O(5) sites in the CuO_x chains. The shortening of the Cu(2)-O(4) bond is taken as evidence for charge transfer between the chains and planes, with the O(4) site mediating [78]. The correspondence between the new modes induced by illumination in the insulating phase of YBCO and the Raman spectrum of the metallic phase convince the authors that a local distortion due to trapped carriers is formed upon illumination. It is suggested that polarons of low effective mass and extending up to several lattice constants are formed along the chains [76, 77].

Similar results done over a much larger energy range revealed that the $\Delta T/T$ for photon energy .09 eV to 2.5 eV had a much larger peak around 1 eV with width 1 eV [79]. The peak at .13 eV decrease rapidly compared with the 1 eV peak when the chopping frequency of the laser beam is varied, so the .13 eV feature is associated with

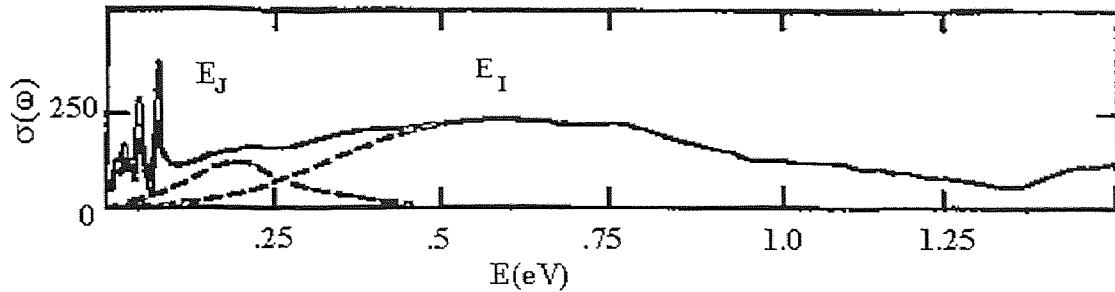


Figure 13 Optical Conductivity of $\text{YBa}_2\text{Cu}_3\text{O}_{6+x}$ crystal with $x \approx .2$. Dashed line shows two separate contributions to spectrum. Taken from Ref. [83].

slower dynamics. Similar PIA and bleaching features in the low energy IR spectra are seen [80] as discussed above. The PIA turns to bleaching above 1.6 eV, which closely corresponds to the charge transfer gap in insulating $R\text{Ba}_2\text{Cu}_3\text{O}_{6+x}$ [81, 82]. The shape of the $-\Delta T/T$ curve is qualitatively similar to the photon energy dependence of IR quenching [33], and we associate this PIA as due to the population of defects in the CuO_x chains.

For the moment, we will return to issues surrounding the optical conductivity in $\text{YBa}_2\text{Cu}_3\text{O}_{6+x}$. Measurements in the range 0 – 1.25 eV reveal a broad peak related to ‘impurities,’ possibly within the basal plane [83]. Figure 13 shows the optical conductivity of a crystalline sample of YBCO with low oxygen content. The peak E_J is near the anti-ferromagnetic exchange energy. It is presumed that this excited state represents the effect of an electron coupled to the lattice through the local spin state. The broad peak near .6 eV is labeled E_I . This peak seems to be a common feature of the insulating precursors to high T_c compounds with CuO_2 planes. For superconducting crystals, both of these peaks are dominated by Drude absorption at low frequency [84].

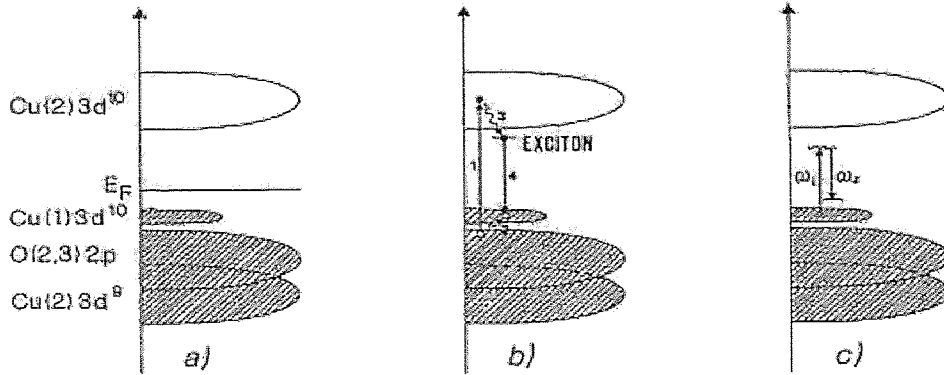


Figure 14 (a) proposed band structure for fully deoxygenated YBCO. $\text{Cu}(2) 3d^{10}$ band is above Fermi energy. $\text{Cu}(1) 3d^{10}$ band acts as narrow intra-gap band. $\text{O}(2,3) 2p$ and $\text{Cu}(2) 3d^9$ bands are hybridized and lie below Fermi energy, i.e. valence band. $\text{O}(2,3) 2p$ and $\text{Cu}(2) 3d^9$ and $\text{Cu}(2) 3d^{10}$ are separated by charge transfer gap of 1.7 eV and $\text{Cu}(1) 3d^{10}$ and $\text{Cu}(2) 3d^9$ are separated by 1.3 eV. (b) Schematic of process involving midgap luminescence (1) electron-hole pair is created, (2) hole migrates from valence band to $\text{Cu}(1) 3d^{10}$ band, (3) electron experiences Coulombic interaction with $3d^{10}$ hole and forms exciton below conduction band, (4) recombination of electron and hole with photon emission. (c) 1.16 eV resonant Raman scattering - ω_i incident photon, ω_s scattered photon. Adapted from Ref. [85].

It appears that a small number of oxygen atoms in the basal planes gives rise to midgap absorption. We associate this absorption with defect states becoming populated.

In a study which compares IR-excited Raman measurements and photoluminescence from intragap states, it is concluded that the $\text{O}(4)$ apex vibrations are strongly coupled to the charge transfer excitations, and that there is a narrow intragap state present even at $x = 0$ [85]. This narrow electronic state is then accompanied by the presence of other midgap states while increasing the concentration of oxygen ions on the $\text{O}(1)$ sites, i.e. increasing x . The presence of midgap photoluminescence (PL) for samples only with $x < .2$ and a peak around 1.3 eV coupled with the resonant nature of the $\text{O}(4) A_g$ mode is unambiguous evidence for the important role that intrinsic defects play in YBCO. In support of their model, the

authors propose a band structure model which treats the Cu(1) $3d^{10}$ states as a midgap band shown in Figure 14. Strictly speaking the narrow band below E_F that is labeled Cu(1) is the antibonding $O(4)p_z - Cu(1)3d_{(3z^2-r^2)} - O(4)p_z$ orbital, or the so-called ‘dumbbell’ complex. A similar model was proposed to explain resonant Raman scattering observed in $YBa_2Cu_3O_{6.1}$ for photon energies between 1.8 and 2.7 eV [86]. However, in this case the dumbbell level is placed beneath the Cu(2)-O(2,3) complex, although it is acknowledged that this level is isolated from the other bands. The dipole matrix elements between these bands are very small, so electronically they can be treated separately. This lends support to the interpretation in Ref. [85], with the added caveat that any such attempt to model YBCO as a band semiconductor may fall short.

Picosecond resonance Raman scattering [87] indicates that the interactions between O(4) sites and photogenerated carriers responsible for the photoinduced insulator metal transition in YBCO [88] are localized within the Brillouin zone. This result tends to support a Fermi glass model for oxygen contents greater than 6.0. The stoichiometric precursor compound is treated as a charge transfer insulator with a well defined gap. Once oxygen atoms are added to the basal plane the gap disappears and the band structure is replaced by a Fermi glass model in which insulating behavior is not due to the presence of a gap, but to the localization of electronic wavefunctions near E_F . It would be interesting to find if the crossover to Fermi glass behavior occurs for $x = .15$ in $YBa_2Cu_3O_{6+x}$, as might be expected from considering the threshold for percolation in Ref. [44]. In the percolation model, the overall transition to metallic behavior occurs near $x = 0.3$ and this is where the Fermi glass description may become appropriate [88]. As the doping induced changes, either by light or adding oxygen,

move the Fermi level away from the localized states and past the mobility edge, the free carrier contributions will dominate the < 1 eV optical conductivity. It is interesting to note that the photoconductive response is considered to be negligible below 1 eV [88], in contrast to Ref. [33] in which PPC is observed for photon energies as low as .93 eV.

One nice feature of the band structure picture is that it naturally accounts for the double well potential presumed to exist for the O(4) atoms, and experimentally observed in XAFS measurements [89]. It is assumed that the coupling between the Cu(1)-O(4) dumbbell's electronic states and vibrational modes depends only on the charge state on the Cu(1) ion [85]. Then, the existence of the double well potential is not surprising. Illumination induced changes in the Cu(1)-O(4) bond length are consistent with the existence of such a double well potential [25].

The importance of these results becomes clear when we consider the prediction that there would be a strong enhancement of the O(4) photon efficiency near 4.1 eV [86]. As we have seen [46], there is a large enhancement of PPC at 4.1 eV (Fig. 7) and this lends credence to the idea that excitations involving Cu(1) sites near an oxygen vacancy have increased PPC efficiency, while also strongly exciting O(4) charge transfer modes. Once again, this supports the conclusion drawn by Federici et al. [29], i.e. that the electron hole pairs responsible for PPC are created and destroyed in the same place, namely the chain layers.

In summing, the interaction of light-induced trapped carriers and charge transfer vibrational modes can tell us about the band structure of insulating YBCO with $x \approx 0$. These results tell us that as oxygen atoms are added to the O(1) site the appropriate description shifts to that of a Fermi glass. Whatever one may choose to believe about

the various band structure / Fermi glass scenarios, it is clear that polaronic distortions play a central role in explaining IR stimulated and picosecond resonant Raman scattering.

In addition, the models presented in support of these results nicely account for the double well potential that exists for the O(4) sites. These sites participate in the transfer of charge from the chains to the planes, thus enhancing the conductivity. Such a model applies to a particular mechanism for PPC, i.e. photoinduced trapped carriers at oxygen vacancies in the chain layers result in the transfer of holes to the planes.

CHAPTER 3

SAMPLE PREPARATION AND CHARACTERIZATION

3.1 Deposition Techniques

3.1.1 Sample Overview

The samples used in this study are thin films of $\text{YBa}_2\text{Cu}_3\text{O}_{6+x}$ deposited on LaAlO_3 (LAO) and SrTiO_3 (STO) substrates. With one exception, the method of fabrication was pulsed laser deposition (PLD). One film was deposited by means of metal organic chemical vapor deposition (MOCVD). The use of different substrates and deposition procedures can help identify possible stress/strain effects as well as processing artifacts. Eliminating or minimizing these concerns allows us to be confident that our results are indicative of intrinsic properties of the material, rather than of substrate film heterostructures.

3.1.2 Pulsed Laser Deposition

Pulsed laser deposition (PLD) is a standard technique for making superconducting oxide thin films [90]. It has an advantage over several other methods in that the stoichiometry of the target material is conserved throughout the whole process. For YBCO, typically thin films are ablated in a chamber with a partial pressure of oxygen. An excimer laser with nanosecond pulse duration is focused onto a target of fully oxygenated YBCO. The laser pulses set up shock waves at the surface of the target material which instantly heat the solid far above its vapor temperature. Material is ejected in the form of a plume, which is directed to the substrate. Provided that the correct portion of the plume is chosen, the stoichiometry of the target material will be

conserved when the ejected material hits the substrate. Additionally, the substrate temperature can be varied in order to control the epitaxy of the film. Since the material is heated so rapidly, the stoichiometry is conserved throughout the entire process and the material settles on the substrate in clusters. Typical deposition parameters are substrate temperature, oxygen pressure, pulse energy, repetition rate, and deposition time. With this method high quality films can be grown in a controllable manner. This provides a good starting point for deoxygenation through annealing. After deposition, in most cases the films were annealed in about 1/2 atmosphere of oxygen at a lower temperature than at which they were deposited. Several of the films were checked for superconductivity. T_c was typically around 88 K, with $\Delta T_c \sim 1$ K. The films deposited on LAO were fabricated at the Army Research Laboratory (ARL), now located in Adelphi, MD. Typical deposition parameters were substrate temperature 865 °C, 125 mTorr Oxygen, 200 mJ/pulse, 12 Hz repetition rate, and 10 minutes deposition time. It was typical to increase the oxygen partial pressure as the film was cooled.

Films on STO were prepared at the Naval Research Laboratory (NRL), in Washington, D. C. The deposition parameters for the two types of films varied somewhat. For these films typical parameters were 750 °C substrate temperature, 320 mTorr oxygen, and 1.35 J/cm² laser fluence. In either case, high quality c-axis oriented films were produced.

3.1.3 MOCVD

One MOCVD-deposited film was used in the study. This film was obtained from Advanced Technology Materials (ATMI) in conjunction with ARL. MOCVD allows

for large area growth of thin films. The process has been described in detail elsewhere [91]. Simply put, β -diketonate complexes ($M(\text{thd})_n$, where $\text{thd} = 2,2,2,6$ tetramethyl-3,5-heptanedionate, and $M = \text{Y}, \text{Ba}$, and Cu) are injected into an heated stainless steel vaporizer. A nitrogen carrier gas takes them to the deposition chamber. The organic solvents evaporate, leaving behind the yttrium, barium, copper, and oxygen in the proper ratio to form YBCO. The process is somewhat more complicated, having more parameters to vary. For details, the interested reader may consult Ref. [91]. A post-deposition anneal in 1 atm of O_2 gas is standard procedure. High quality films are also produced by this method. The T_c of this film was 88 K, with ΔT_c approximately 1 K.

3.2 Characterization of Thin Films

3.2.1 Characterization Techniques

In general the characterization of thin films with respect to oxygen content is different from bulk material. Structurally, bulk material has been extensively characterized by neutron powder diffraction [92]. The critical temperature varies with the oxygen content, showing the well known ‘two-plateau’ behavior (See Fig. 2). The transition to non-superconducting behavior occurs near the orthorhombic to tetragonal phase transition which roughly coincides with the metal insulator transition. Previously, the c -axis length had been observed to vary with the oxygen content in a regular fashion [93]. Figure 15 shows the variation of the c -axis parameter with oxygen content for both films and bulk. This dependence is continuous through the metal insulator transition, indicating a second order phase transition. In $R\text{Ba}_2\text{Cu}_3\text{O}_{6+x}$, a change in oxygen stoichiometry from $x = 0$ to $x = 1$ results in about a 1.3% contraction of the c -

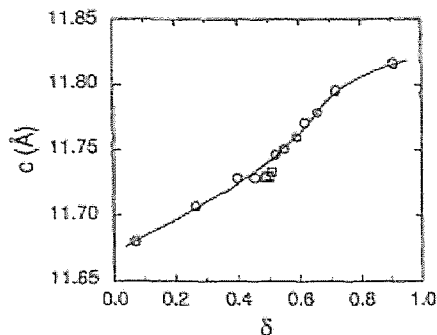


Figure 15 Variation of c-axis lattice parameter with oxygen deficiency, δ in $\text{YBa}_2\text{Cu}_3\text{O}_{7-\delta}$. Ref [94].

axis. Because of stress and strain effects arising from mismatch between the lattice parameters of the substrate and sample, the c-axis' dependence on oxygen content is different in thin films. It is necessary to seek more than one method of characterization in order to reliably assess the oxygen content. Detailed studies, comparing the bulk values with those on films, have shown that this relationship can vary quite a bit [94]. It is possible to use XRD data, if one also compares the integrated intensities of select peaks along with measurements of the c-axis.

Techniques such as Rutherford backscattering (RBS) are unsuitable for the assessment of the oxygen content because of the relative insensitivity. The backscattered particles are characterized only with respect to the energy of the particles. A difficulty can arise from scattering by heavier elements deeper within the film and lighter elements near the surface. This tends to smear out the spectrum in the energy range where oxygen appears. RBS is suitable for assessing cation stoichiometry in $\text{RBa}_2\text{Cu}_3\text{O}_{6+x}$, for example, verifying the 1:2:3 ratio. However, it can damage the surface of the film. Raman spectroscopy is a simpler and quicker technique to estimate both the cation stoichiometry and assess the oxygen content [95]. Substrate effects

have been studied [96], and a comparison of XRD and Raman techniques along with RBS data [97] shows that extreme care must be undertaken in order to reliably determine the amount of oxygen in thin films.

3.2.2 Substrate Effects - Strain

The substrates used in this study were either STO or LAO. STO has cubic crystallographic structure with a lattice constant of 3.905 Å. Since our films are at or near the metal-insulator transition, we can assume $a \approx b = 3.86$ Å [92]. This represents a lattice mismatch of about 1.2%. Since the unit cell of STO is slightly larger than YBCO, we expect the film to be under slight tensile stress. Thermal mismatch at the boundary is not expected to be a significant factor, as both substrates have similar coefficients of thermal expansion [98, 99]. LAO has rhombohedral symmetry, but its diffraction pattern can be fit with a ‘pseudocubic’ unit cell with a lattice parameter of 3.797 Å. In this case the film is under compressive stress and the lattice mismatch is roughly 2%. In a sense, having two different types of films on either side of the zero strain state is useful. It allows us to reason that strain effects are of minimal consequence in our results, as both types of films show the same behavior. Ideally, we would have zero strain, but in any thin film system such effects must be considered.

3.2.3 Annealing

To maximize the PPC effects, the thin films had to be carefully annealed in either an inert atmosphere such as Argon, or a very low concentration (980 ppm) of oxygen gas

with the balance nitrogen. Films A and B were annealed at higher temperatures than films C, D, and E (See Table 1 for identification of samples).

Table 1 Summary of characterization data for $\text{YBa}_2\text{Cu}_3\text{O}_{6+x}$ samples

<u>sample</u>	<u>c-axis length (Å)</u>	<u>substrate</u>	<u>oxygen content</u>	<u>fabrication</u>
A	11.839, [1.4] ^a	LaAlO ₃ (100)	6.25 ^b	e (PLD)
B	N/A	LaAlO ₃ (100)	6.45 ^c	f (MOCVD)
C	11.858, [1.5] ^a	LaAlO ₃ (100)	6.20 ^{c,d}	e (PLD)
D	11.776, [1.3] ^a	SrTiO ₃ (001)	6.40 ^d	(PLD)
E	11.798	SrTiO ₃ (001)	6.38 ^d	(PLD)

a - [005/006] ratio, b – Reference [94], c – Reference [100],

d – Reference [29], e – Reference [91], f - all $\pm .05$ oxygen content except B $\pm .1$.

Annealing the films according to that which is prescribed for bulk [80, 92] proved to be unfruitful. We found that in even a very small partial pressure of oxygen, the films retained a fair amount of oxygen, and could tolerate much higher annealing temperatures than were expected. In the final stage, films A & B were annealed at 760° C and 748° C respectively in 980 ppm oxygen, balance nitrogen. A platinum-rhodium thermocouple was placed next to the sample while it was in the furnace. In most cases, a platinum boat was fashioned out of the end of the thermocouple. Several different furnaces were used and the flow-rate was chosen such that the volume of the furnace was replaced once per minute, resulting in a flow-rate of anywhere from 2-6 liters per minute. Films C, D, and E were annealed in an argon atmosphere at much lower temperature, 520° C.

Instead of trying to follow a recipe based on bulk or other film systems, in which annealing parameters seem to vary with thickness and other characteristics, we

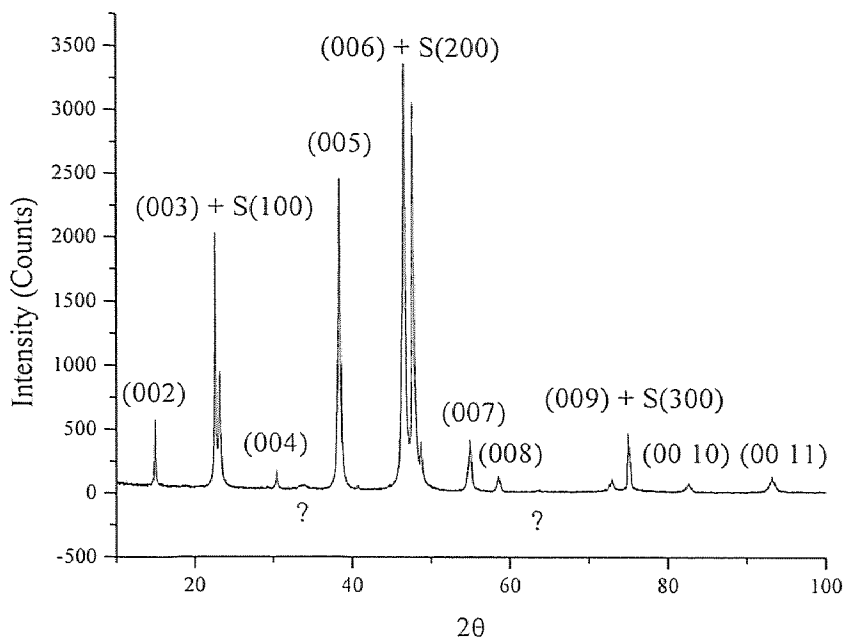


Figure 16 Bragg peaks of Sample A after initial post-deposition annealing to make $\delta \approx 0$.

decided to target resistivity as a means of rough characterization [100]. Occasionally, this resulted in overshooting and near complete removal of oxygen. The films were simply annealed in an oxygen atmosphere until the room temperature surface resistivity fully recovered.

In any case, once the annealing was complete the films underwent XRD measurements to verify that they had not become contaminated. None of the films had any new diffraction peaks, nor any evidence of contamination. All films were stored at least one week in dessicant before use, to minimize room temperature annealing effects on optical/photoconductive measurements [15].

3.2.4 X-Ray Diffraction Measurements

Figure 16 shows the Bragg peaks of film A after post-deposition annealing in O₂ while cooling. The measurements were made in a Phillips powder diffractometer in conventional θ - 2θ geometry, and copper K- α radiation (1.542Å). The edge length of the pseudocubic unit cell of LAO is nearly 1/3 of the c-axis lattice parameter in YBCO. The peaks corresponding to Miller indices S(hkl) = S(h00) slightly overlap with the (00 3·l)YBCO peaks (S indicates substrate). This provides a convenient starting point for peak indexing. Diffraction occurs due to interference between reflected wavefronts from parallel planes in the Bravais lattice. A schematic is shown in Figure 17, along with a diagram of a Bragg diffractometer. The condition that must be satisfied for interference to occur between successive wavelets is:

$$n\lambda = 2d \sin(\theta). \quad (3.1)$$

Reexamining Figure 16, we identify the peaks as follows. With the exception of the two peaks labeled with a question mark, the pattern clearly indicates that the film is single-phase c-axis oriented material. The first additional peak is close to the (111) peak in YBCO, yet the relative strength of the peak is 1/50 of the (103) peak or 1/12 of the (123) peak which do not appear [101]. In similar fashion, there are other peaks which should also be present if the additional feature is the (111) reflection of YBCO. Typical contaminants can be ruled out by Raman spectroscopy, as will be discussed later. However, there are gold electrodes on the film which could contribute to the diffraction pattern. Gold crystallizes with the FCC structure of edge length 4.08 Å. Analysis of the FCC structure factor tells us that the first three reflections expected are {200}, (202), and (111). Because of the combined width of the substrate (100) and

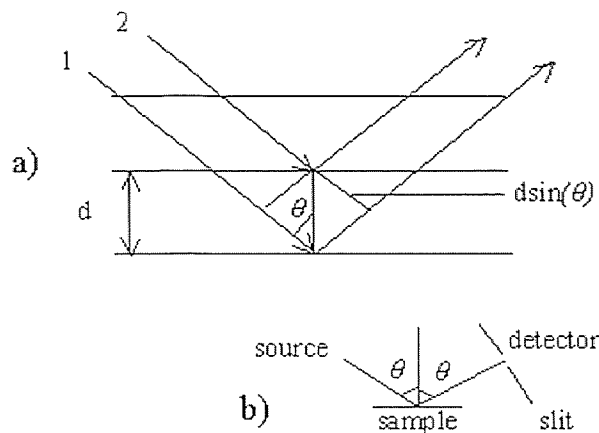


Figure 17 (a) conditions for Bragg scattering (b) detector arrangement

YBCO (003) reflections, the appearance of the relatively weak $\{200\}$ reflections will be masked. However, the (202) and (111) planes contain more atoms and the structure factor is correspondingly stronger. Therefore, we assign these extra reflections as arising from the gold electrodes. Later, when care is taken to avoid the electrodes, these peaks no longer appear. Figure 17 illustrates the geometric conditions necessary for Bragg scattering to occur.

Once we have satisfied ourselves that we have quality c-axis oriented material, the next step is to reversibly remove oxygen. Figure 18 illustrates the effect of annealing. The solid line is essentially a repeat of Figure 16 with log-log axes and the abscissa changed to the d-spacing between planes. After annealing at 620°C in 910 ppm oxygen, the diffraction pattern has changed. The substrate peaks do not move, but there is evidence of a systematic shift of the (001) reflections to larger d-spacings. On the figure, the reflections are identified by their l index. This shift is entirely consistent with the observed contraction of the c-axis upon addition of oxygen [15, 16, 94].

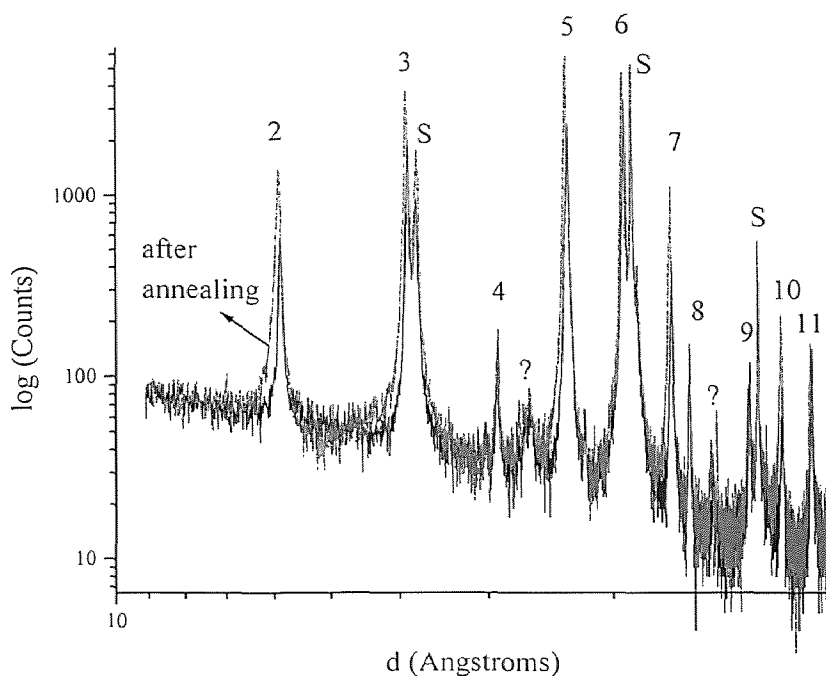


Figure 18 Log-log plot to illustrate effect of annealing on c-axis lattice parameters. Number above peak is index l in $(0\ 0\ l)$ reflection, S indicates substrate peak. Note shift to higher d-spacing when oxygen is removed.

Figure 19 shows the changes observed in the (005) peak as the result of annealing. Before annealing the FWHM of the peak is $.150^\circ$, as obtained by a Lorentzian fit. After annealing, the width is essentially unchanged, despite the intensity of the peak growing by more than a factor of two. The intensity is defined by integrating the area under the peak. In similar fashion, the (006) peak's FWHM is $.160^\circ$ before and after annealing. The ratio $\frac{I_{005}}{I_{006}}$ changes from .70 to 1.10. The c-axis grows from 11.667 to 11.737 Å, in both cases $\pm .003$ Å. This corresponds to a reduction in oxygen content from $x = 7$ to $x = 6.5$ in $\text{YBa}_2\text{Cu}_3\text{O}_x$ [94]. Since the fractional error in the measured

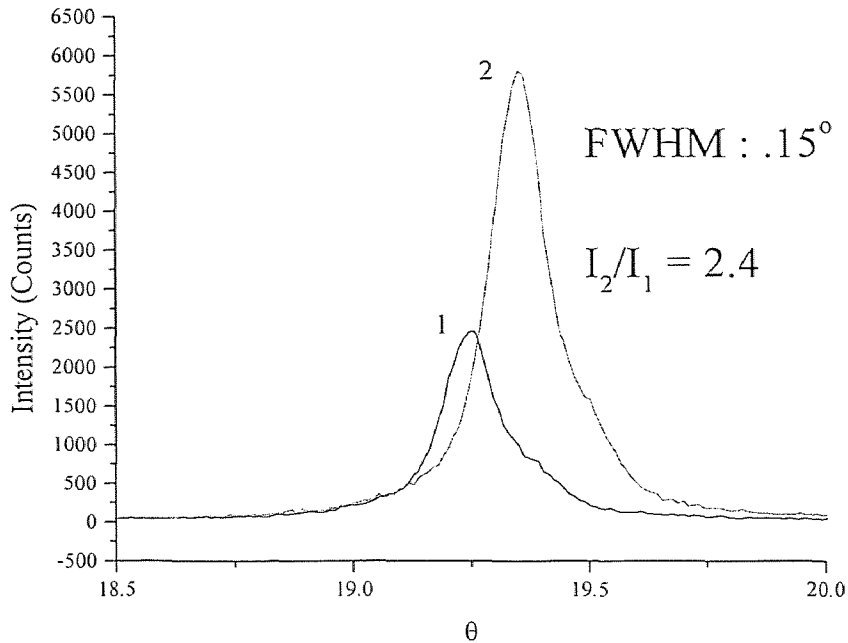


Figure 19 Width and intensity of (005) peak at intermediate annealing stage (1) and after final (2) annealing. Note that even though the intensity has changed by a factor of 2.4, the width remains constant.

lattice constant, $\frac{\Delta c}{c}$, varies directly with $\cos^2(\theta)$, the $l > 5$ indices are chosen for calculating the lattice parameter [102]. In most cases, it was possible to identify peaks out to (00 11). We base our error estimate on this formula and the location of the substrate peaks relative to their standard values.

Finally, we would like to illustrate the desired effect of annealing our films. We compared the relative change in resistivity for an intermediate annealing stage (oxygen content ≈ 6.6) and final stage (oxygen content ≈ 6.26). Figure 20 shows the effect of annealing on the relative change in resistivity for Film A, namely it increases by nearly

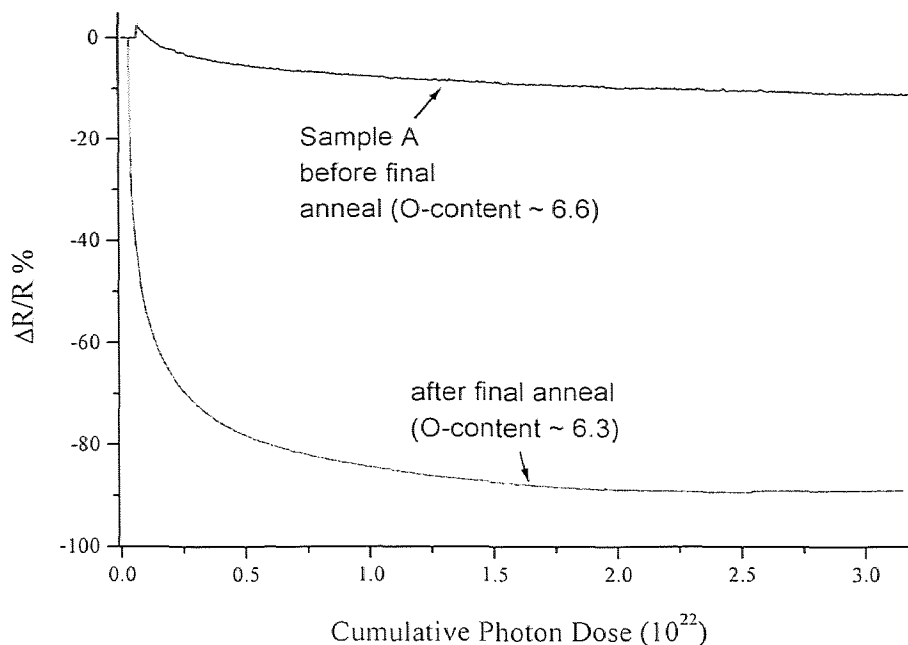


Figure 20 Increase in photoresponse, i.e. $\Delta R/R\%$ as a result of annealing for Sample A.

an order of magnitude. As can be gleaned from Figures 15, 18, and 19 the only significant change as the result of annealing has been a loss of basal plane oxygen. Table 1 summarizes the final results obtained from XRD patterns of the thin films. The measurements were made in a Siemens GADDS Highstar Platform powder diffractometer with multichannel CCD detection. Copper K- α radiation is used, and the instrumental resolution is 100 arc-sec.

3.2.5 Raman Scattering

As a check for contaminants, several of the films were investigated by means of Raman spectroscopy. Scattered radiation is shifted in energy due to the interaction of light with the lattice. The scattering can either create (Stokes) or annihilate (Anti-

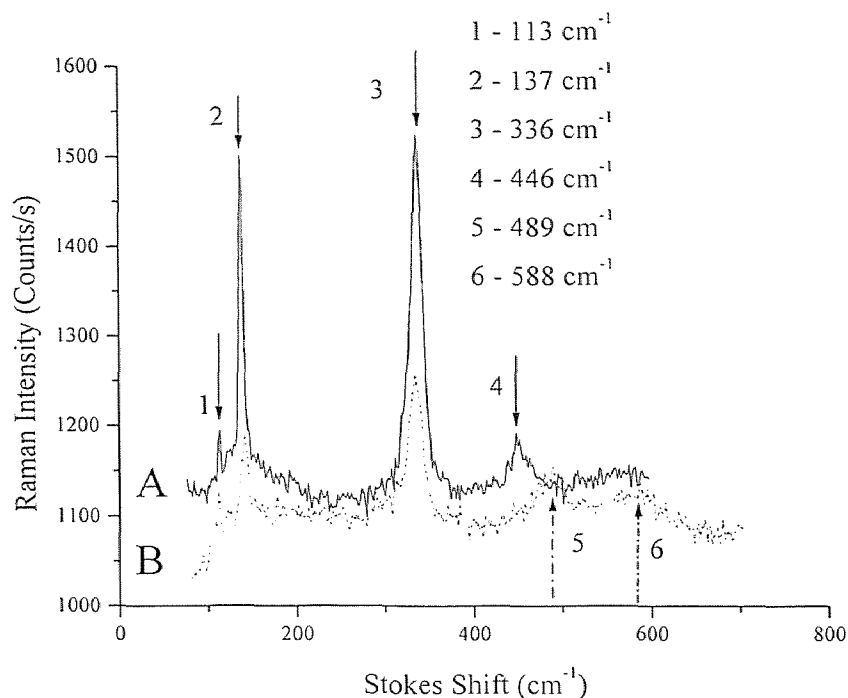


Figure 21 First order Raman spectrum (A) at moderate power density, and (B) after exceeding the damage threshold. (Film A) Numbering of modes explained in text.

Stokes) a phonon. Typically, the term Raman scattering applies to the process where an optical phonon is involved and Brillouin scattering when the phonon is in the acoustic branch. Raman scattering involves probing the unit cell by photons with wavenumbers a factor of 10^{-3} smaller than that of a typical reciprocal lattice spacing. With this technique we can learn about the local coordination within the unit cell. The occurrence of such processes depends on the polarizability tensor, α . In general, the enumeration of Raman-allowed modes is a group theory problem, and can be quite complex. Classification of the modes according to symmetry greatly reduces the amount of calculation involved. However, our interest in Raman spectroscopy is only

for the purposes of checking the film integrity and for the presence or absence of known contaminants.

It is typical to assign the z-direction in the polarization tensor to the c-axis, or (001) direction. Similarly the x and y directions are assigned to the a and b axes, respectively. Porto notation, $z(x, x)z$, is often used in which the incident and scattered directions are outside the parenthesis, while the incident and scattered polarizations are inside. The as-grown films are orthorhombic, but not completely epitaxial, so we cannot distinguish the x and y directions. Therefore, we will simply represent the scattering processes such as $z(x, x)z$, and understand it to include such terms as $z(x, y)z$, etc.

The first order Raman spectrum for $\text{YBa}_2\text{Cu}_3\text{O}_{6+x}$ extends out to 600 cm^{-1} . All modes with larger wavenumbers are multiple phonon scattering processes. For nearly fully oxygenated YBCO, the largest Raman active mode observed is around 500 cm^{-1} . The insulating parent compound, $\text{YBa}_2\text{Cu}_3\text{O}_6$ has a peak at 600 cm^{-1} . The oxide materials that are typically used to make YBCO, such as BaCuO_3 , CuO , and Y_2O_3 , should be readily identifiable in the region between 100 and 600 cm^{-1} . Additionally, parasitic phases that may develop such as Ba(OH)_2 , BaCuO_2 , and YCu_2O_5 , also have many Raman active modes in this wavenumber range [103, 104]. The first order Raman spectrum of Sample A is shown in Figure 21, the curve marked 'A'. The sample is placed on the stage of an optical microscope and a 488 nm laser beam was directed onto the thin film through the microscope objective. The spot on the surface is imaged, and when it is brought into focus the maximum amount of scattered light is collected. Although the focus is wavelength dependent the shift is so small in

comparison that this can be ignored. The scattered light is directed into a Dilor X-Y spectrometer with $\pm 2 \text{ cm}^{-1}$ resolution. The scattered light hits a diffraction grating and reflects onto a cooled CCD array detector. The entire spectrum can be recorded in ten seconds, and it is possible to co-add scans to improve the signal to noise ratio. In Figure 21, ten scans were averaged.

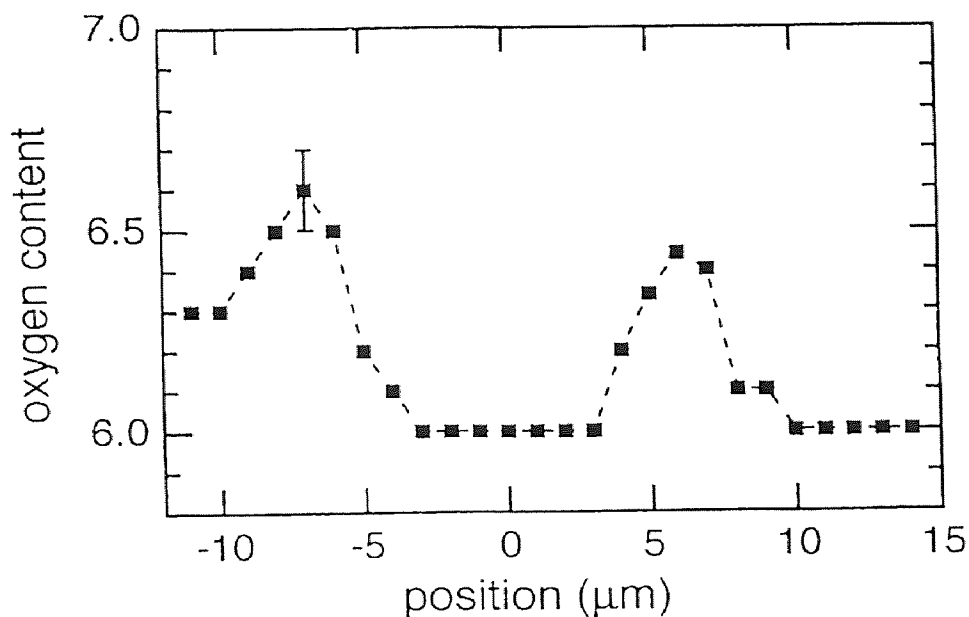


Figure 22 Oxygen content as a function of radial distance from center of damaged spot. Adapted from Ref. [107].

The modes observed (marked 1 – 4 in Fig. 21 marked ‘A’) are consistent in our scattering geometry with those previously reported for single crystals of YBCO with variable oxygen content [105]. Since our films are heavily oxygen deficient, they do not exhibit the 500 cm^{-1} O(4) mode very strongly as in other studies [95, 96, 97]. This is due in part to the strongly zz polarized nature of this mode.

We also investigated our films for resonant Raman scattering as discussed in Section 2.2.6 [53, 54, 55, 56]. We found no evidence for the additional lines that are observed in the spectrum when illuminating with power densities from 1.5 – 70 kW/cm². Our results are consistent with those reported in investigations of laser heating and oxygen desorption in thin films [106, 107]. In those studies, the authors report a range of oxygen content within the spot size when illuminated with greater than 63 kW/cm² power density. Our substrate, LAO has a smaller thermal conductivity than MgO, the substrate used to establish the damage threshold [106, 107].

Correspondingly, we expect that our damage threshold is somewhat lower. However, in a film of low oxygen content, the damage threshold must be exceeded by a fair amount in order to observe changes in the Raman spectrum. In the laser heating and annealing studies, it was observed that when films are illuminated with power densities greater than the damage threshold, in the center of the damaged spot the local oxygen content is nearly 6.0, while at the edges it is actually higher. Figure 22 shows the oxygen content as a function of radial distance from the center of the annealed spot [107]. This suggests that while oxygen is driven away from the center of the spot, it is absorbed near the edge of the ring.

We illuminated a film with a 60 mW 488 nm beam focused to about 1 μm spot size, or a power density on the order of one MW/cm², and simultaneously recorded the Stokes Shift at room temperature [108]. The Raman spectrum is marked 'B' in Figure 21, and the two new lines are at 490 cm⁻¹ and 590 cm⁻¹. The other lines lose some intensity and the 141 cm⁻¹ Cu(2) mode moves to slightly higher wavenumber, but remain relatively unchanged. These results are consistent with the damaged spot

consisting of areas of very low oxygen concentration surrounded by a ring of much higher oxygen content [107]. Thus, in a film which exhibits a very strong response to light ($\Delta\rho/\rho \sim 95\%$ @ 77 K), there are no resonant lines up to and above the damage threshold.

Raman measurements on our films compare well with the spectra taken on crystalline samples [105]. We find no evidence for impurity phases or starting compound contamination [103]. Additionally, we find no RRS lines in a film which exhibits PPC very strongly.

3.2.6 Resistivity Measurements

Sample B was the only film for which an XRD pattern was not obtained after annealing. Initial post-deposition XRD measurements indicated that the film was c-axis oriented. Resistivity vs. temperature measurements indicated a sharp superconductive transition at 88 K with a transition width of about 1 K. Room temperature resistivity measurements indicate a room temperature value of $3.4 \pm .2 \text{ m}\Omega\text{-cm}$ [109]. According to previous reports [100, 110], this places the oxygen content in the vicinity of either 6.9 or 6.4. Temperature dependent resistivity measurements indicate that the film is not superconducting down to 77 K, so the oxygen content cannot be 6.9. Therefore, this film has an oxygen content of about 6.45 (± 0.1).

Having discussed the characterization of the films, we will now briefly review the experimental techniques and apparatus used in our study. Then, in Chapter 5, the new experimental results will be discussed along with a simple model for our results.

CHAPTER 4

EXPERIMENTAL TECHNIQUES AND APPARATUS

4.1 Experimental Overview

4.1.1 Typical Experiment

The prototypical experiment performed involved cooling the sample down to liquid nitrogen temperature and illuminating it with laser light. Usually, the sample was exposed to visible light for approximately 1 – 1 1/2 hours with about 4 Watts output power. Next, infrared laser light from either a Ti:Sapphire laser or tabletop Nd:YAG laser would be directed onto the sample. Various data had to be recorded such as the voltage drop across the sample, the sample temperature, and the change in voltage as a result of illumination. The next several sections will describe the experimental apparatus and the techniques used to record the data.

4.1.2 GPIB Interface

Several instruments were required to simultaneously record data. A personal computer, or PC, was used to automate data acquisition. This was accomplished through the use of a General Purpose Interface Bus, or GPIB board. This interface conforms to IEEE – 488 standard. The use of a GPIB interface is preferable to that of an RS-232 or other interface because of its near universality and ability to ‘stack’ devices such that they can be simultaneously connected to a PC. We used several cards from National Instruments that were driven with Lab Windows software. Code can be written in a standard programming package such as C or BASIC and compiled, automating data

acquisition. Each instrument used is specially fitted with a GPIB interface. Data points are taken once per second. All instruments are rack mounted in a portable arrangement.

4.1.3 Sample Mounting

To facilitate reproducible measurements, a system needed to be developed in order to mount the samples. Either Au or Ag contacts were deposited before postdeposition *or* oxygen removal annealing. Extremely low contact resistances may be obtained this way, several orders of magnitude lower than the surface resistance of fully oxygenated YBCO [111]. For our purposes, the contact resistance is immeasurably low, since we are dealing with films having resistivity on the order of a few $\text{m}\Omega\text{-cm}$ and the contact resistance is well below one $\mu\Omega\text{-cm}$. As shown in Figure 23, samples were affixed to a copper plate with GE Varnish as an adhesive. GE Varnish is an electrical insulator, but is thermally conductive. Strips of a PC circuit board with electrically insulating backside were glued to the plate. The plate was then bolted to the cold finger of the cryostat with Apezion grease applied to the backside. This ensures that the sample and cold finger are in good thermal contact. Silver paste, DuPont compound 4929A, was placed on top of the gold contacts and thin gold wire, typically about .5 mm thickness, was attached to the silver paste. The gold wire was then soldered to the PC board. Electrical measurements were made by soldering wires to the PC circuit board that were attached to a ten pin connector on the cryostat. In this way, the sample and mount could be treated as a package, and direct handling of the sample was minimized. The contacts were checked for ohmicity by applying currents from -5 to $+5$ mA, and measuring the voltage drop on the sample. In all cases the voltage drop and current

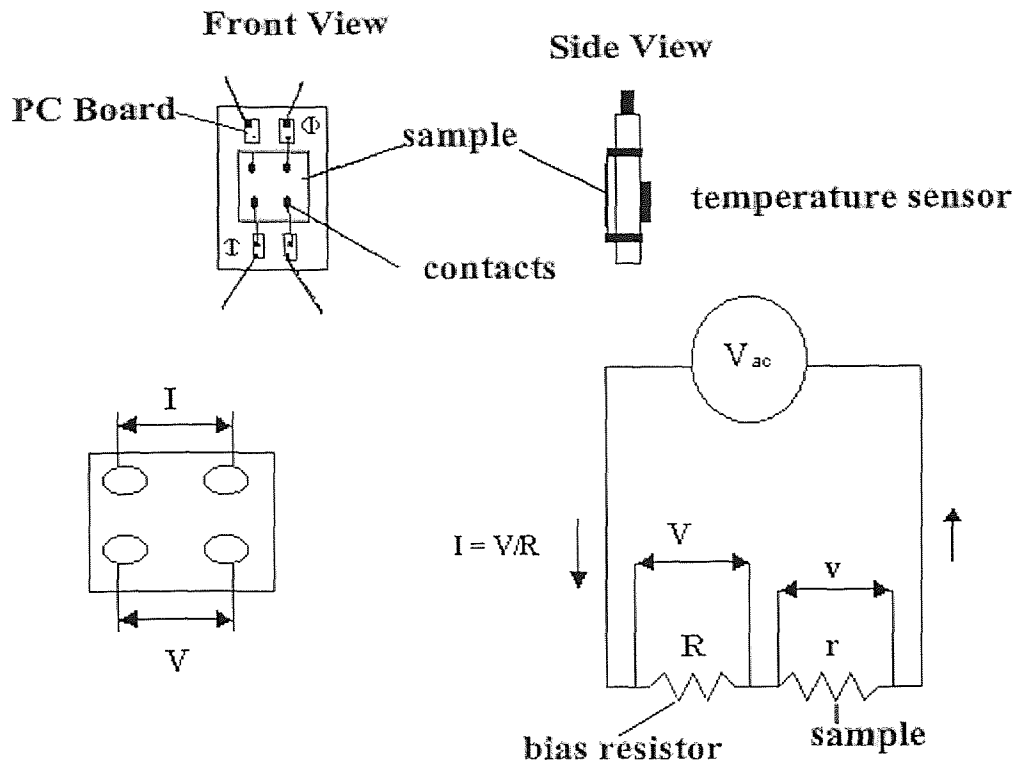


Figure 23 Sample mounting, 4-point technique, and circuit used to measure voltage drop across sample, v . Note that $R \gg r$.

scaled linearly. During data acquisition, the current never exceeded 1 mA in any of the samples. Therefore we felt confident that the electrical contacts would not produce spurious signals.

4.1.4 Resistance Measurements

A standard technique to measure resistivity is typically referred to as a Van der Pauw four-point measurement. A current is applied to the sample across two adjacent contacts, and the voltage drop across the material is measured using the other two

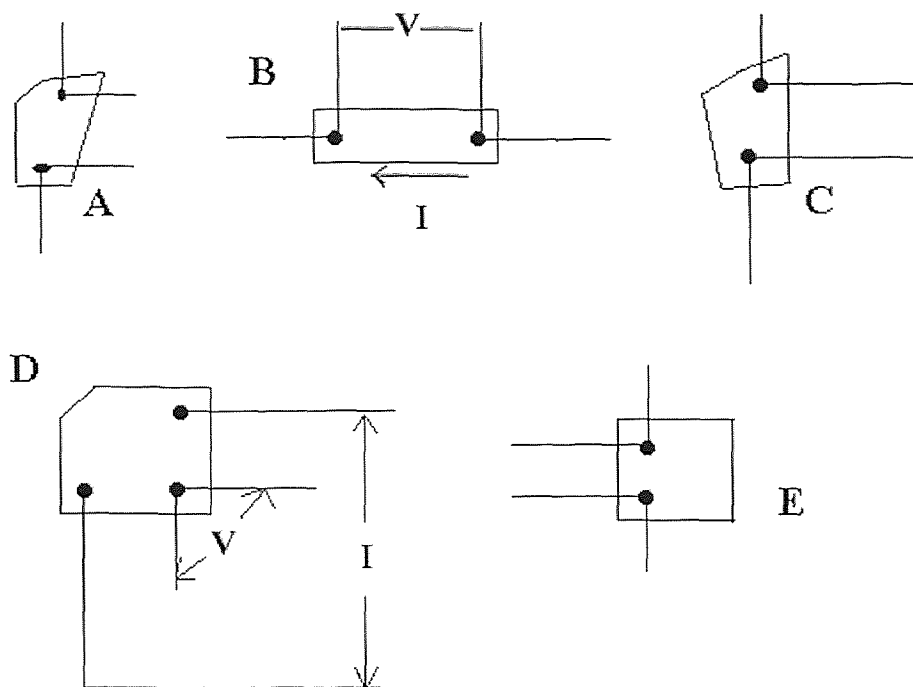


Figure 24 Sample/contact geometry for Samples A...E. Application of I , and measurement of V shown for Sample B & D.

contacts, as shown in Figure 23. From knowledge of the current applied and a geometric factor involving the arrangement of the contacts one may convert the voltage measurement directly into a resistivity value. It is best if the current is kept constant, so that changes in voltage truly represent changes in resistivity. A standard trick to accomplish this is using a 'bias' resistor connected in series with the sample. The value chosen should be large enough that the sample resistance may be neglected in calculating the current in the circuit.

Our films did not have four contacts. The geometry of the samples did not allow for direct determination of the resistivity. The various arrangements for films A-

E are shown in Figure 24. Since our principal aim was to measure relative changes in resistivity as the result of illumination, we are not greatly affected by our lack of knowledge of the geometric factor.

4.1.5 Lock-in Amplifier

The resistivity measurements were made by either an analog Stanford SR510 single phase lock-in amplifier, or a digital EG&G 760 DSP dual phase lock-in amplifier. When provided with a reference signal, the lock-in amplifier filters and amplifies an input signal to remove line signals and noise, and then multiplies the input signal by a sine wave with the reference frequency. Based on standard Fourier analysis, the resultant signal will have two frequencies, one near DC ($f_{ref} - f_{sig}$) and $2f$ ($f_{ref} + f_{sig}$). An electronic filter eliminates all frequencies except those near DC. This allows the lock-in to detect only signals with a frequency in a small range about the signal frequency. The DC gain after the filtering stages and the AC gain at the front of the lock-in amplifier have an inverse relationship represented by a quantity called dynamic reserve. If too much DC gain is used the output is unstable against fluctuations. If a large AC gain is used at the front end, the signal will cause overloads. In analog lock-in amplifiers, there is a trade-off between dynamic reserve and stability. Typically the best results are obtained when the lowest possible dynamic reserve setting was used. In a true digital lock-in, there is a AD converter at the front end with an anti-aliasing filter preventing stray signals from being digitally converted. A microchip, digital signal processing unit, creates a 24-bit sine wave and carries out the 24×24 bit multiplication. A digital lock-in amplifier offers a large improvement in stability and sensitivity over

analog lock-ins. The trade-off between dynamic reserve and stability is removed, due to the AD conversion. We found that the analog lock-in was unreliable when measuring signals below $10\mu\text{V}$, whereas the DSP lock-in was reliable to 50 nV [112].

Another feature of the lock-in amplifiers is that they have internal function generators. In the EG&G DSP lock-in, the reference signal is generated internally with a crystal clock. It was typical to apply an AC signal of .1 or 1 V to the sample at a frequency of about 1 kHz. The use of the lock-in amplifiers' own reference signal helps to minimize the possibility of stray signal aliasing in the reference input channel.

4.1.6 Fluke Multimeter

Large decreases in resistance due to illumination, such as those seen with our samples, could potentially cause a small change in the voltage drop across the bias resistor.

Consequently, there is an increase of the current applied to the sample. To compensate for this, we record the voltage across the bias resistor, so that we can always recover the changes in voltage that are due only to sample resistivity changes can always be recovered. A Fluke FL8520a digital multimeter was used for this purpose.

Now that all of the relevant parameters are known, it is a simple matter to relate the sample resistance to the measured voltages and bias resistor. In the limit that the bias resistor is much larger than the sample resistance, and the input impedances of the devices that are in parallel are much larger than both, the sample resistance may be obtained:

$$r = \frac{vR}{V} \quad (4.1)$$

where r is the sample resistance, v is the sample voltage, R is the bias resistance, and V is the voltage drop across the bias resistor.

4.1.7 Temperature Measurements

A silicon based diode is attached to the back of the cold finger such that it is level with the sample, Lake Shore part # DT-470 CU. Apezion grease is applied to the interface between the diode and cold finger in order to insure good thermal contact. The accuracy depends on a calibration curve, and for the temperature range in which it was used it varied between 80 – 120 mK. The sensor output was read by a Lake Shore 330 temperature controller. In this way the sample temperature may be varied between 77 K and 325 K. Heating the samples is accomplished by applying a current to a 50 Ω resistor wound about the top of the cold finger. In most of the optical measurements, the samples are immersed in liquid nitrogen, so the temperature is presumably constant. Of course, if we wish to heat the sample, the sample chamber will have to be emptied of liquid nitrogen first. The heating due to illumination is at most 2-3 K [107].

4.2 Cryostat

We use a Janis VT-100 model equipped with four windows for optical access, shown in Figure 25. The film is mounted on the end of the cold finger, which is at the end of a long rod, or, the sample stick. A dial at the top of the sample stick allows for fine adjustment of vertical position as well as rotational adjustment. To have reasonable hold time for liquid nitrogen, it is necessary to evacuate the outer chamber to

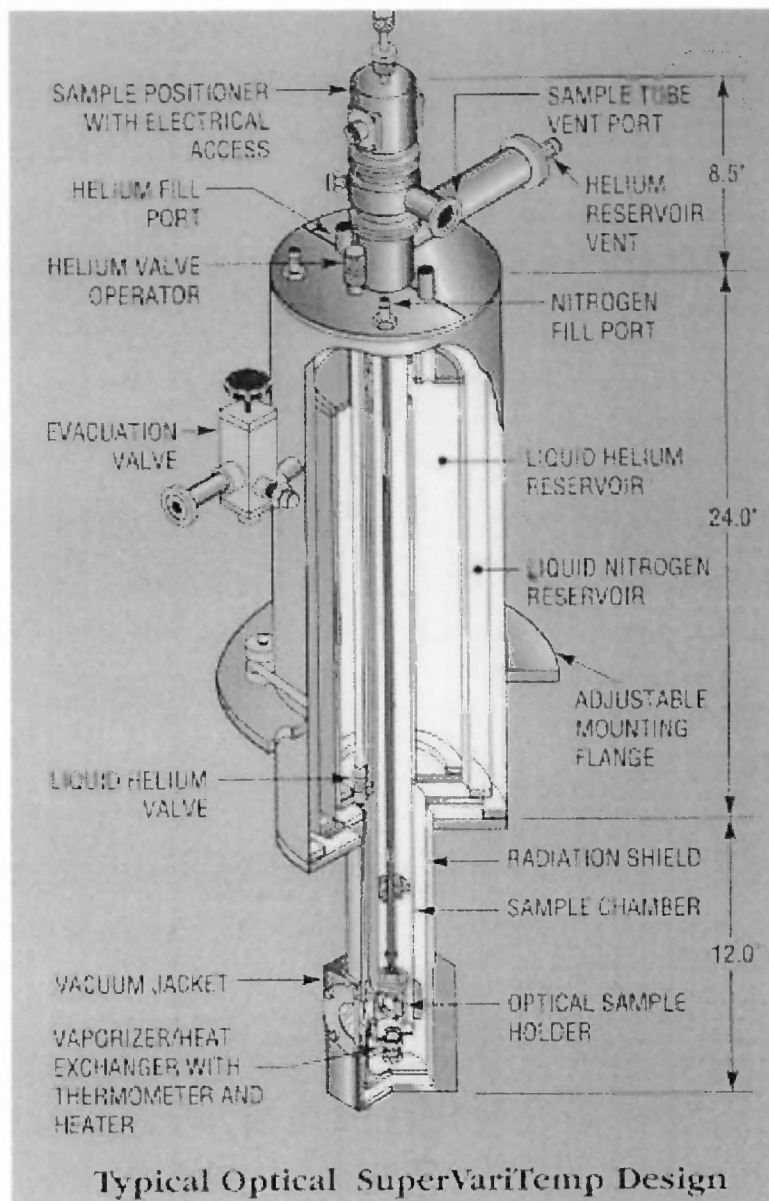


Figure 25 Optical access cryostat used in study.

approximately 10^{-5} Torr. A residual pressure of 10^{-6} Torr or less is preferable, if it can be achieved. Typically a mechanical roughing pump and oil based diffusion pump are used, equipped with Quickfit connectors. A thermocouple gauge provides a rough estimate of the pressure. Occasionally, a turbo pump system is available which increases the hold time from approximately six hours to almost twelve. After

evacuation, liquid nitrogen is added to the specified port. A system of Teflon tubing, Parker fittings, and valves is connected to the vent port in order to regulate the flow of liquid nitrogen into the sample chamber. The nitrogen becomes gaseous and exits the vent port creating a pressure differential, inducing the flow of liquid nitrogen into the sample chamber. A control temperature sensor is placed below the sample chamber. The valve connecting the sample chamber and nitrogen reservoir may be operated independently of the connection between the sample chamber and vent port. If all of the valves are shut, and there still is liquid nitrogen in either chamber, as it becomes gaseous it will exit the Helium reservoir vent. This is useful for measurements in which the sample is allowed to gradually warm up to room temperature overnight. Once liquid nitrogen is added to the cryostat, the sample is constantly bathed in N_2 gas until it is immersed in liquid. An inert atmosphere reassures us that our films' oxygen content are not altered during illumination. A constant concern is the presence of H_2O in the sample chamber. When the sample stick is not in the cryostat, it is always capped with an o-ring seal, to minimize the possibility of such contamination.

4.3 Lasers and Optical Measurements

4.3.1 Argon Ion Laser

For photoconductive measurements in the visible, a large frame Coherent Innova 200 Argon Ion (Ar^+), or a medium frame Coherent Innova 70 is used. In addition, the large frame laser pumped a $Ti:Al_2O_3$ laser with output in the near infrared. The large frame laser consumes up to 30 kW with an maximum output of 30 W. The Ar^+ lasers have several lines in the visible between 476.2 and 514.5 nm. Replacing a mirror at the end

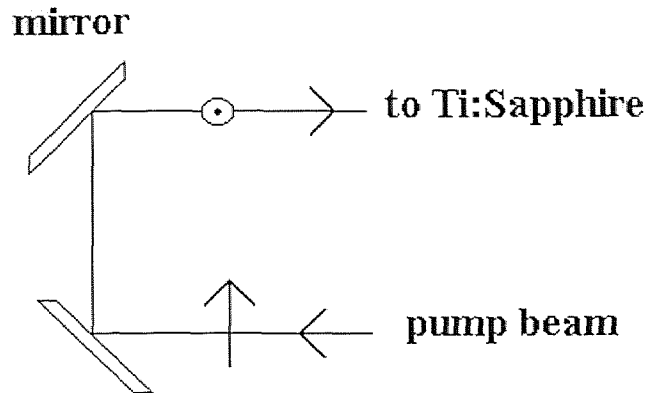


Figure 26 Rotation of polarization of pump beam.

of the tube with a prism allows for the selection of a particular wavelength. For our purposes, this is not necessary, and we operate in multi-line mode. The ends of the tube are cut at Brewster's angle such that the output beam is vertically polarized. The output power is measured by a pyrometric power meter. The large frame laser has a photodiode by the end of the tube which can be calibrated to aid in stabilizing the output.

4.3.2 Ti:Al₂O₃ Laser

For measurements in the near infrared, a Clark-MXR Ninja 4 kit laser is used. This laser is pumped by the Ar⁺ laser. A Ti:Al₂O₃ crystal has absorption bands in the visible and emission bands in the near IR. Typical operating ranges are between 700 and 1000 nm. The output of the Ar⁺ laser is vertically polarized. The Ti:Al₂O₃ laser requires horizontal input, so the polarization must be rotated by 90°. Two successive reflections, first vertical, then horizontal will accomplish this, as shown in Figure 26.

The arrow denotes the direction of polarization before reflection, and the circle with a dot in the middle denotes polarization into the page after reflection.

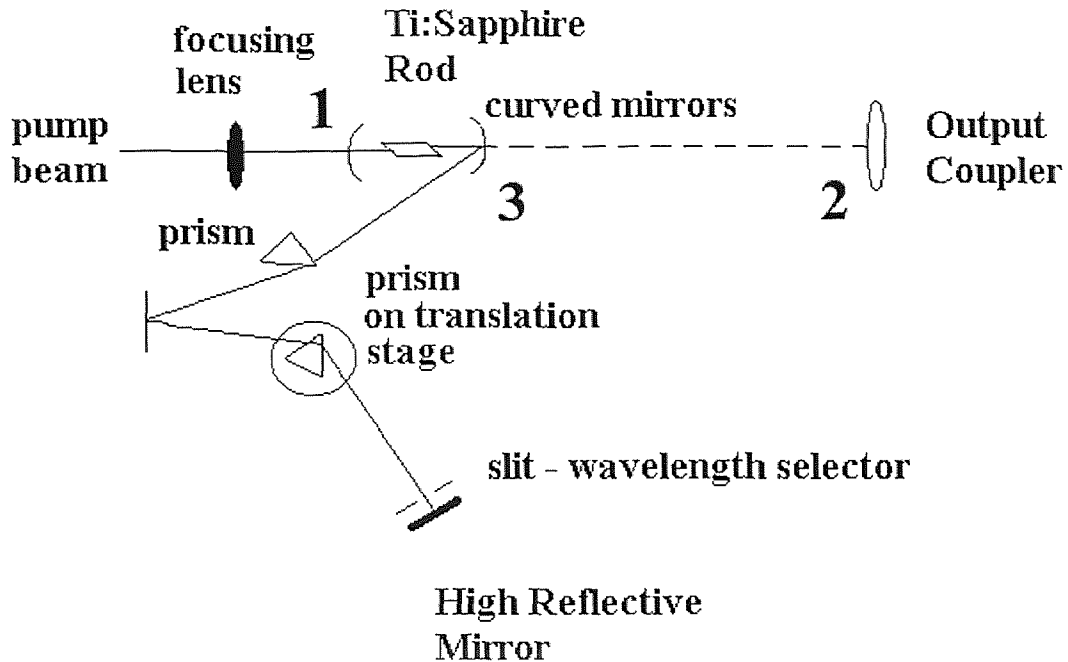


Figure 27 Ti:Sapphire Laser Cavity. See text for explanation on mirror numbering.

The cavity requires alignment in order to produce lasing. A simplified version is shown in Figure 27. The laser is operated in continuous wave (CW) mode in this alignment, although it could be mode-locked if required. The pump beam enters the enclosure and is focused onto the Ti:Al₂O₃ rod, which is cut at Brewster's angle to minimize reflection losses. Two curved mirrors which transmit the light but are partially reflective are on either side of the rod (mirrors 1 and 3 in Figure 27). Part of the beam is allowed to reach the output coupler (mirror 2 in Figure 27) which is specially coated in order to transmit 2% of the light and reflect 98% back into the

cavity. The portion of the beam that hits the second curved mirror is reflected onto the prisms in order to account for dispersion in the cavity. The second prism is on a translation stage which can be used in order to select the wavelength. Typically the pump beam would be seven Watts. For wavelengths near the edges of the gain curve, it would be increased to ten Watts. Once rough alignment has been achieved, it is necessary to 'walk' the high end reflector and output coupler into a parallel configuration to induce lasing. An unbiased photodiode is placed in the path of the beam that leaves the cavity and connected to an oscilloscope. Then the X and Y controls of the mirrors are adjusted iteratively. At each step, the negative voltage recorded by the diode is optimized, creating a feedback loop. Sometimes it is necessary to detune one mirror quite a bit in order to compensate for the tilt of the other. Gradually, the mirrors become more parallel and as the cavity begins to lase, the voltage recorded by the diode suddenly saturates. Then a power meter replaces the diode, and the output power is optimized.

The wavelength can be adjusted by translating the second prism towards the direction of the rod. The prism causes a different portion of the beam to be incident upon the tuning slit, much like a prism separates white light into its components. By selecting the proper portion of the infrared 'rainbow,' one can tune the wavelength. The slit is made as small as possible without reducing the power in order to keep the wavelength spread as narrow as possible. We have two sets of mirrors for different wavelength ranges. The first set is for wavelengths between 720 and 890 nm. The second set covers between 840 and 1000 nm. The optics have different reflection coatings so they all must be changed in order to change the wavelength range.

4.3.3 Wavelength Measurement

Figure 28 shows the arrangement for measuring the wavelength of the Ti:Al₂O₃ laser. A portion of the beam is deflected onto a surface which diffusely reflects. This allows the beam to be collected by a lens $2f$ away which is F- matched to the monochromator, and then focused onto the receiving slit a distance $2f$ from the lens. The F-number of a lens is the ratio of its focal length, f , to its diameter. Choosing the proper F-number lens ensures that the first curved mirror of the monochromator will be filled with light. This couples the maximum possible amount of light in. Since the diffusely reflecting surface can be treated as a point source the geometry is especially simple. Inside the monochromator, the beam reflects off of the diffraction grating and hits the exit slit. A photodiode is placed on a xyz translation stage behind the slit. The signal is fed into a lock-in amplifier with the output of a beam chopper as the reference frequency, and when the tilt of the diffraction grating produces the maximum signal, the scale reading is recorded. The monochromator is calibrated every run using a He-Ne laser. A linear relationship is derived from the principal maximum corresponding to the wavelength of the laser, and first order diffraction maxima which can be treated as twice the wavelength. The He-Ne laser is directed onto the diffusely reflecting surface, and the Ti:Al₂O₃ beam overlaps it. The resolution, R , of the monochromator is given by:

$$R = \frac{1}{2} d \times s \quad (4.2)$$

where $d = \frac{3894}{N}$ is the dispersion, N is the number of grooves per mm, and s is the slitwidth in μm . Typically, we would use a slitwidth of 50-100 μm , resulting in $R \approx 1$ nm.

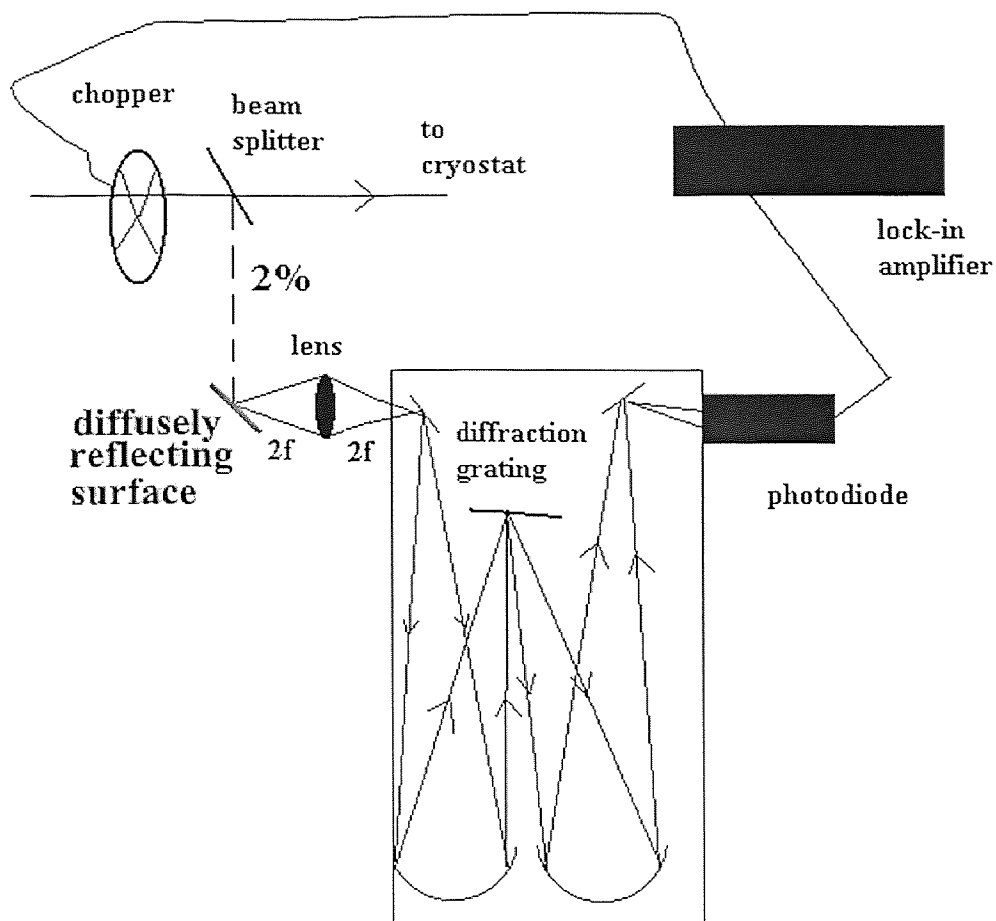


Figure 28 Monitoring the wavelength of the Ti:Sapphire laser.

4.3.4 Procedure and Data Acquisition

After the films have been mounted, placed in the sample chamber, and the cryostat has been pumped down, liquid nitrogen is added to the cryostat's reservoir. Liquid nitrogen is allowed to flow into the sample chamber, and the sample's resistance vs. temperature curve is recorded. This is done before each run in order to ensure that the sample has not degraded in some way. If the sample exhibits noticeable variation it is discarded. Typically the contacts become brittle after several runs, and are replaced. When the

sample is illuminated it is always immersed in liquid nitrogen in order to prevent annealing effects. Occasionally, room temperature measurements are performed, in which case the sample is in N_2 gas. Additionally, it is customary to mask the contacts in order to guard against spurious signals from stray beams during illumination. No differences are seen in the response to light when the contacts are made with silver paste, indium solder, or lead-tin solder. When illuminating with an infrared beam after visible light, every attempt is made in order to overlap the beams. The position of the IR beam can be checked with an infrared viewer.

Any other experimental particularities will be dealt with in the discussion of the results. The next task will be to present and discuss the experimental results found in this study.

CHAPTER 5

EXPERIMENTAL RESULTS

5.1 Illumination with Visible Light

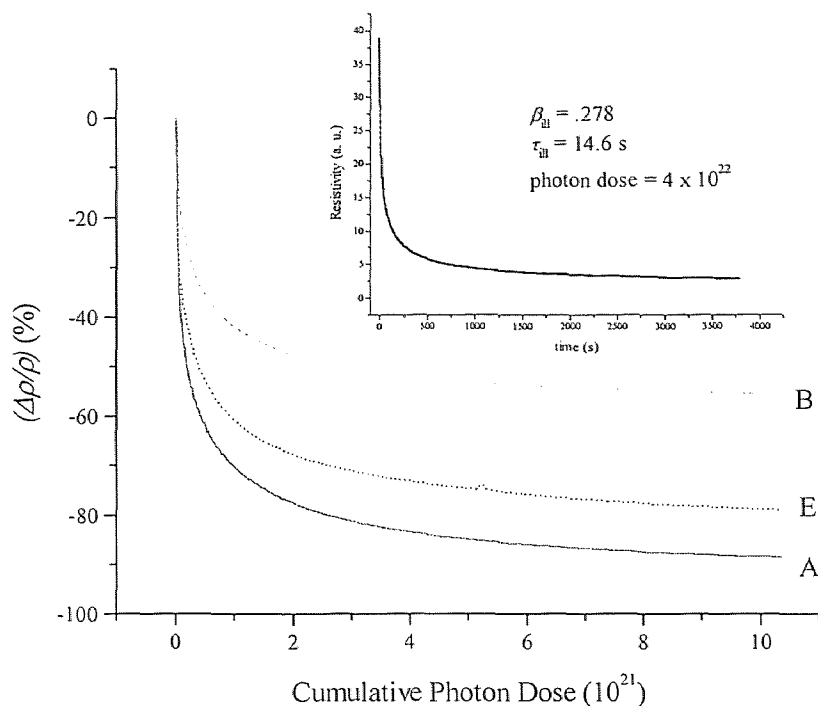


Figure 29 Relative change in resistivity vs. cumulative photon dose for several films (inset) Fit of resistivity vs. time (Eqn. 2.1) for Sample A when illuminated with 4 W all lines Ar+ laser light. Fit parameters shown on plot.

As discussed previously, when oxygen deficient films of YBCO are exposed to visible light, their resistivity decreases according to stretched exponential decay [23, 40] (Equation 2.1). Figure 29 shows the response of several films during irradiation with 4 W (All Lines) Argon Ion (Ar+) laser at 77 K when immersed in liquid nitrogen. All three films had a large relative change in resistivity upon illumination. Typically, a

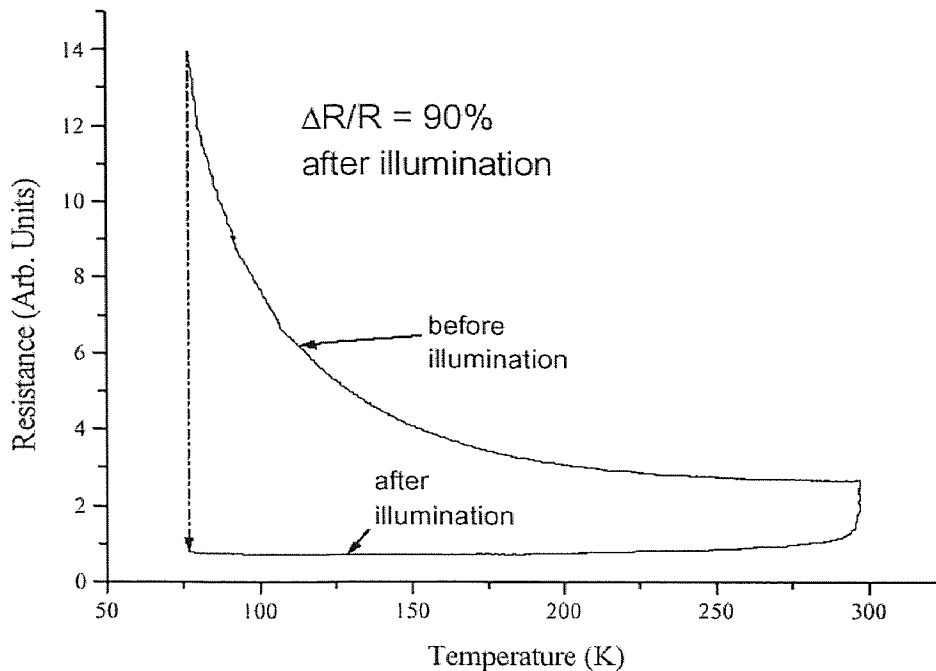


Figure 30 Hysteresis in Resistance vs. Temperature curve for Sample A. Sample is cooled to 77 K, then illuminated. It is allowed to slowly warm, excess conductivity decays in about 30 hours.

photon dose of $\sim 10^{23}$ is required for saturation, however, there is disagreement about whether saturation actually occurs [40, 110]. The inset shows the time dependent decay of the resistivity during illumination for Sample A. The line through the points is a fit to Equation 2.1 which minimizes χ^2 and is subject to the constraints that $\rho_\infty < \rho_0$, $0 < \beta_{\text{ill}} < 1$, and $\tau_{\text{ill}} > 0$. It is doubtful whether the fitted value of the exponent, β , is meaningful within the context of any accepted theory. Currently, fitting the time dependent behavior of the resistivity during illumination to Eqn. 2.1 is purely

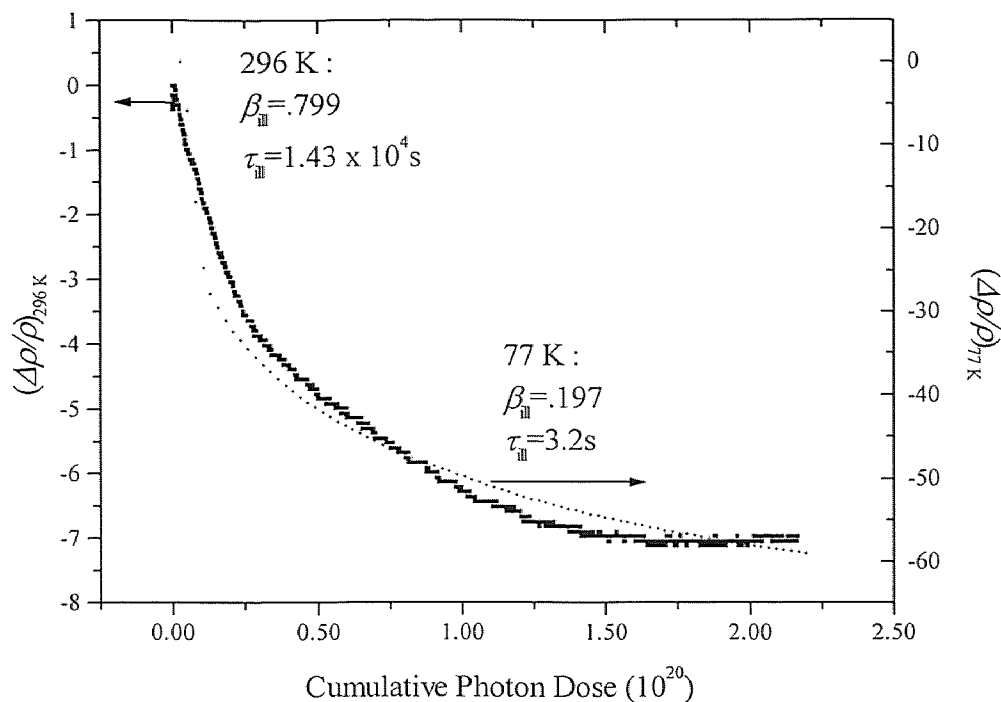


Figure 31 Contrasting the behavior of Sample E when illuminated at 296 K and 77 K, respectively.

phenomenological. We intend to provide some justification for such a fit based on a microscopic model for PPC.

Most striking is the reversible nature of resistivity changes induced by illumination through temperature recycling. Strong illumination causes the dependence of resistivity on temperature to be suppressed. In Figure 30, this is shown for Sample A. The film was cooled down to 77 K from room temperature and illuminated with approximately 10^{23} photons. Then the sample is allowed to slowly warm to room temperature. Once the sample is returned to room temperature, the resistance slowly

reaches its unilluminated, uncooled value over a period of approximately 24 hours. This loop may be repeated many times without any adverse effects to the sample.

Figure 31 contrasts the behavior of Sample E when illuminated at 296 K and 77 K, respectively. We plot the normalized change in resistivity vs. photon dose (At 296 K, the photon flux was considerably weaker and exposure time commensurately longer than for 77 K) for both temperatures. As can be seen, the efficiency is temperature dependent. A complete study of this temperature dependence reveals that below 220 K, the lifetime of the photoinduced state is essentially infinite [41]. We chose to do the vast majority of our illumination experiments at 77 K, with the sample immersed in liquid nitrogen. This allowed us to use an average laser power of 4 Watts which reduced the amount of time it took to achieve the saturation value of the resistivity.

5.2 Infrared Quenching

5.2.1 Wavelength Dependence

A major portion of our experimental work was devoted to the wavelength dependence of infrared quenching in YBCO. As discussed in sections 1.5.2 and 2.4.3, if oxygen deficient YBCO is exposed to infrared light after visible illumination, the photoconductive state can be partially quenched. The quenching efficiency is defined as the change in resistance due to IR light divided by the change in resistance induced by visible light, i.e. $\frac{\Delta R_{\text{IR}}}{\Delta R_{\text{VIS}}} \cdot 100\%$ [30, 33]. For any single wavelength, the maximum observed quenching efficiency is typically about 2%. For broad-banded light between 1.5 to 5 μm , the quenching efficiency is about 10%. The results of separate measurements for Samples A and B are shown in Figure 32. The experiments were

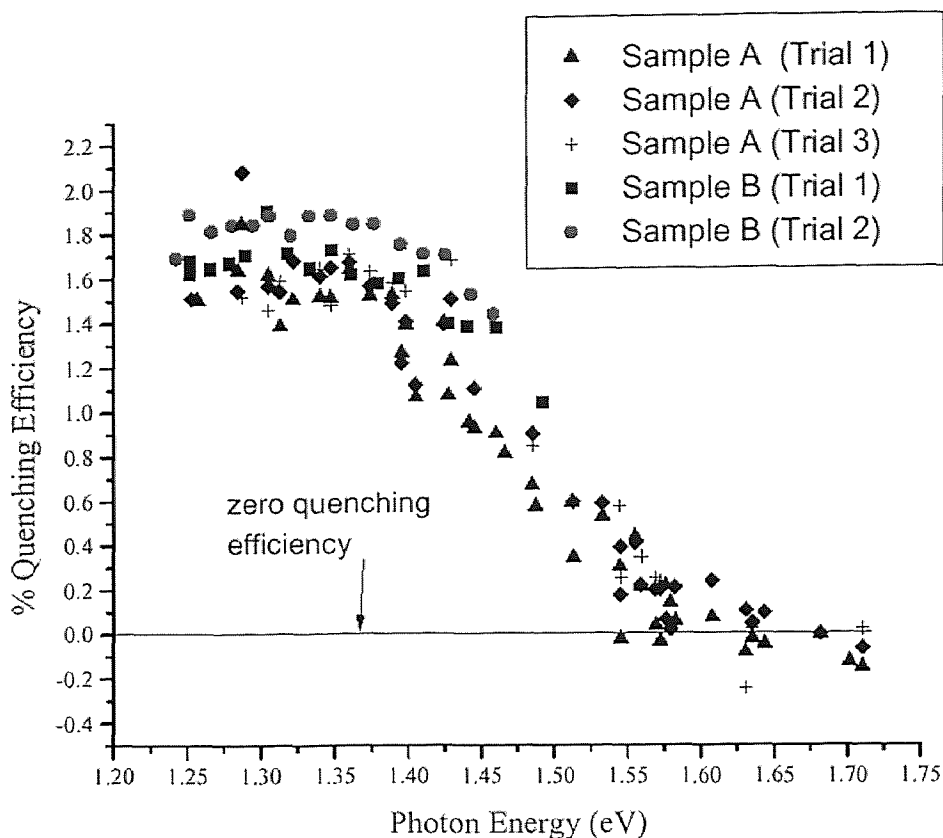


Figure 32 IR Photon Energy Dependence of Quenching Efficiency for Samples A & B (after visible illumination).

conducted as follows. First, the sample was cooled to 77K, then illuminated with a 4W all lines Ar⁺ ion laser beam. Then, once the change in resistivity had nearly saturated, the sample was exposed to infrared light. The wavelength and quenching efficiency were recorded, and the sample was exposed to visible light to recover the resistance value prior to IR illumination. Measurements on sample A were done somewhat differently than sample B. When studying sample A, exposure to the same IR wavelength was repeated several times before stepping in wavelength (typically 5-10 nm). Measurements on sample B followed the protocol that the wavelength was stepped after each exposure to IR light. As can be seen from examining Figure 32, the

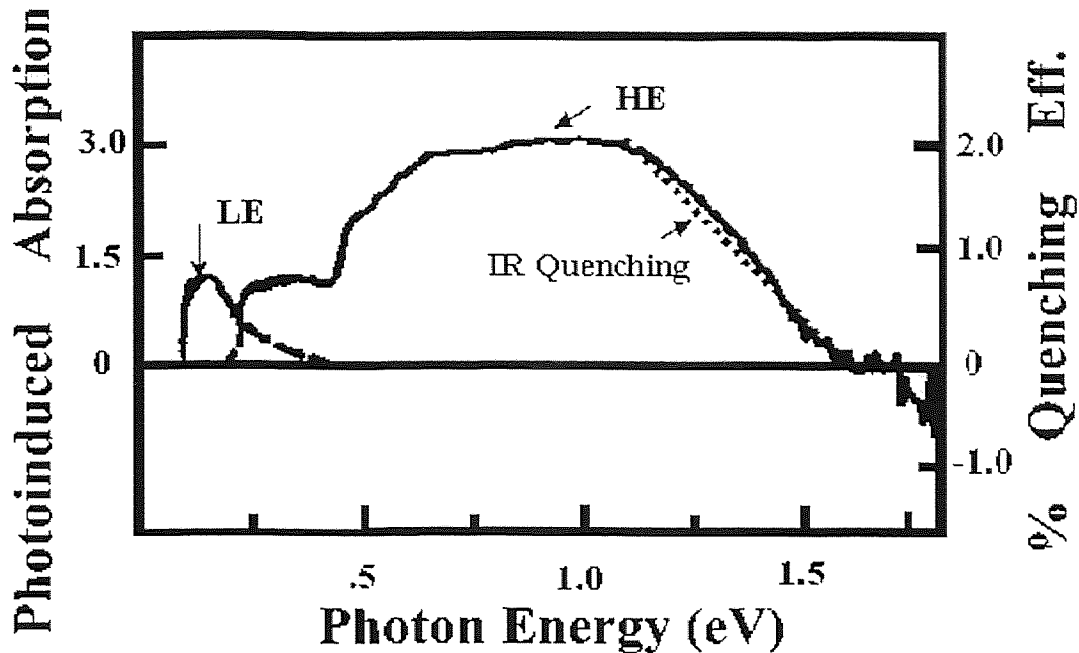


Figure 33 Comparison of HE band of Ref [79] with photon energy dependence results for Quenching Efficiency of Fig. 32. Dashed line represents linear fit to one of the trials in Fig. 32. Left vertical axis in units of $10^{-4} -\Delta T/T$

onset of IR quenching occurs at about 1.6 eV. The data are not inconsistent with a small further decrease in resistance when illuminating with photon energies greater than 1.6 eV after visible illumination. The quenching efficiency saturates at photon energies below approximately 1.3 eV.

In Figure 33, we compare a linear fit (dashed line) of the quenching efficiency with the photoinduced absorption (PIA) results of Ref. [79]. Insulating samples of YBCO have a well-defined gap which is readily apparent in absorption spectra [81, 82]. The energy region of interest applicable to both IR quenching and PIA is within the gap. Examination of Figure 33 reveals that there are two photo-induced absorption bands of interest when exciting with 2.4 eV photons. The first feature, referred to as the low energy (LE) band, is centered at .15 eV and has width of about .15 eV. The

second, or high energy (HE) band, is centered at about 1 eV, with width about 1 eV. We believe that there is a correspondence between the HE band and IR quenching. Noting that positive values of $-\Delta T/T$ correspond to absorption, we see that both IR quenching and $-\Delta T/T$ become positive at around 1.6 eV. Additionally, both saturate at about 1.3 eV. Finally, the HE band in Figure 33 begins to decrease below .8 eV, with $-\Delta T/T$ becoming zero at about .25 eV.

For physical interpretation of these results we refer to Figure 14 and the picture developed in Ref. [85] (see section 2.4.4). We note that the top of the hybridized Cu(2)-O(2,3) band is separated from the top of the Cu(1) band by about .3 eV, and separated from the Cu(2) anti-bonding orbitals by about 1.6 eV. Recall that the Cu(1) band is treated as an impurity band for small values of x in $\text{YBa}_2\text{Cu}_3\text{O}_{6+x}$, and is present even at $x \approx 0$ as evidenced by mid-gap photo-luminescence measurements [85]. When oxygen is added to the basal plane, the mid- to near infrared (.3 – 1.7 eV) absorption grows until the metal-insulator transition is reached and the well-defined gap disappears [82, 83, 84]. We observe that IR quenching becomes very small for metallic samples, and seems to disappear when a band picture is no longer appropriate

Finally, we also refer to Section 2.2.4 and Fig. 7, in which the PPC efficiency spectrum is shown. The enhancement of the 4.1 eV peak is at least an order of magnitude greater than the 3.2 eV peak. There is a peak in the absorption coefficient at the same energy, but it is only about a factor of three greater than at 3.2 eV [82]. The reason for the enhancement of the PPC efficiency at 4.1 eV seems to do with the fact that this transition has been ascribed to $O(4)p_z - Cu(1)3d_{(3z^2-r^2)} - O(4)p_z$, or so called

‘dumbbell’ transitions in which a Cu(1) site is bordered by two oxygen vacancies [46]. Previously, measurements the PPC efficiency spectrum had been limited to between 1.6 and 3.4 eV, and attributed to electronic transitions within the CuO_2 planes. This lends strong credence to the interpretation that the PPC efficiency at 4.1 eV is enhanced by a larger factor than one would expect from looking at the absorption coefficient, because the electronic transition involved occurs close to an oxygen vacancy.

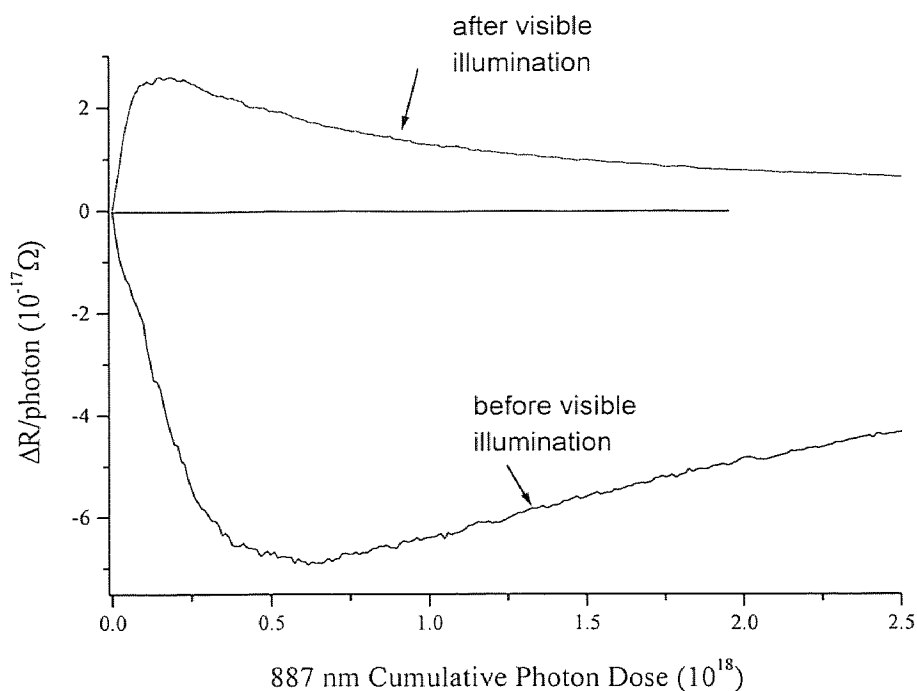


Figure 34 Comparison of Sample A’s response to 1.4 eV (887 nm) before and after illumination with visible light.

Coupling the IR quenching/PIA experimental results with the PPC efficiency measurements at 4.1 eV, one may conclude that there is a relatively broad distribution

of mid-gap states which are probed by IR quenching and PIA measurements. It appears that the presence of these states is correlated with a small distribution of oxygen atoms in the basal plane. Once the insulator-metal transition is approached (i.e. the oxygen content increases) and a band picture is no longer appropriate, then these defect states can no longer be optically probed. Furthermore, the ability to initiate the PPC state is greatly enhanced if one generates electron-hole pairs in close proximity to oxygen vacancies. We feel that these results strongly support a defect-based model for PPC as suggested by previous work [27, 28, 29, 30]. However, there are still unaddressed questions left to answer. Namely, the magnitude of IR quenching seems to be too small to account for the change in resistivity due to visible or UV illumination. We will attempt to account for this in the remaining sections of Chapter 5.

5.2.2 Photon Dose Dependence

After measuring the wavelength dependence of IR quenching, it was natural to question the manner in which the IR photoconductive response varied with visible photon dose. Previously, it had been reported that the photoconductive response to photons with energies less than 1.6 eV was negligible [23]. We were surprised to find out that this was not the case [33]. Sample A was exposed to 1.4 eV (887 nm) photons before and after exposure to 2.4 (514.5 nm) eV photons. *Before* visible illumination, the resistance was observed to *decrease* with exposure to 1.4 eV photons in accordance with stretched-exponential decay, albeit at a lower efficiency than for 2.4 eV photons. On the other hand, *after* visible illumination with approximately 10^{22} 2.4 eV photons, the resistance was observed to *increase*. Figure 34 shows the change in resistance per

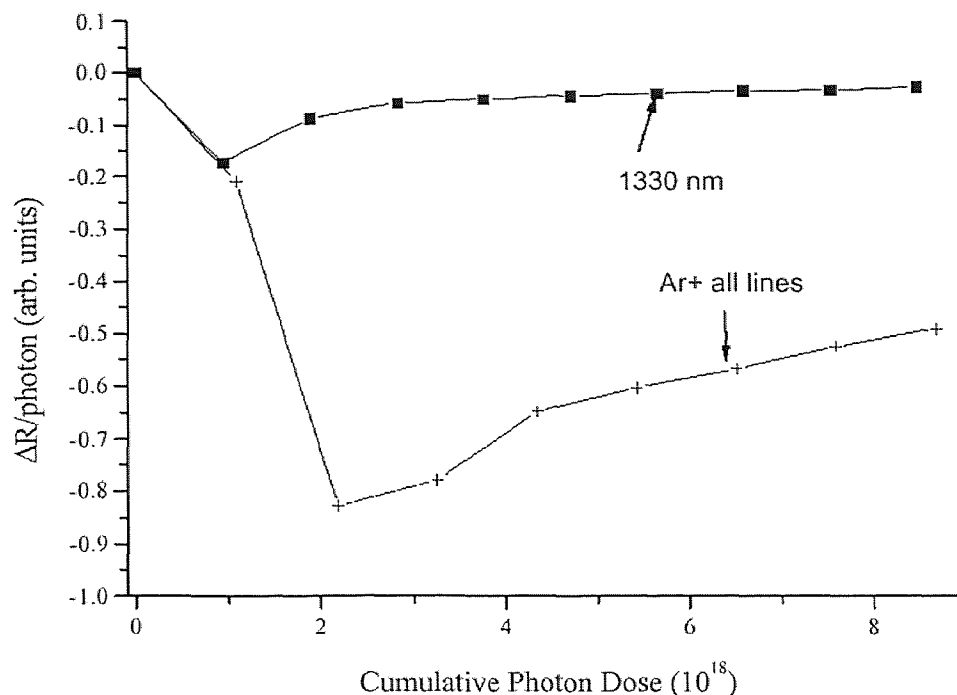


Figure 35 Comparison of Sample C's response to 1330 nm (.93 eV) and 514.5 nm (2.4 eV). The response to Ar+ light is about an order of magnitude greater than 1330 nm light which is consistent with the spectral efficiency measurements of Refs. [23, 29, 46].

photon for 1.4 eV light for sample A before and after illumination with 2.4 eV photons. We repeated this experiment for .93 eV light (1330 nm). The results are shown in Figure 35, where the response to .93 eV photons is contrasted with the response to 2.4 eV photons for Sample C. Similar behavior was observed for Sample A.

The next logical step seemed to be recording the quenching efficiency as a function of visible photon dose. We did this for Sample A, and the results are shown in Figure 36. A similar graph was obtained for Sample C. We found it surprising that the

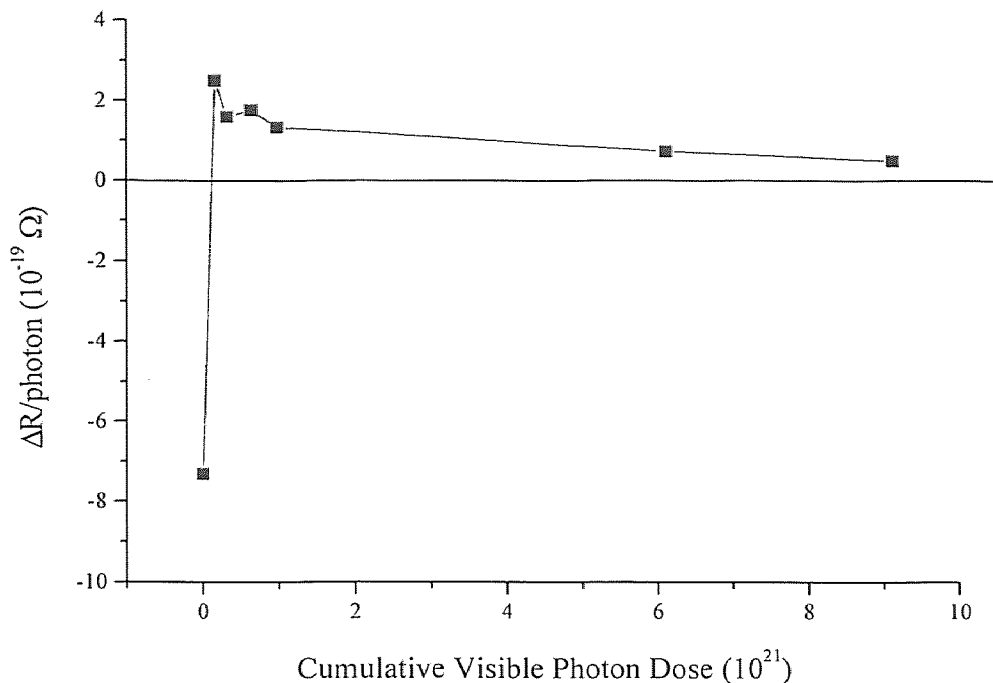


Figure 36 Quenching Efficiency as a function of Cumulative Visible Photon Dose for Sample A (1330 nm).

quenching efficiency saturates almost immediately, i.e. for photon doses on the order of 10^{19} photons. This is approximately 1 part in 10^4 of the photon dose required to saturate the change in resistivity due to illumination.

It may be helpful to pause for a moment and summarize our results before moving on. It seems that, within the range of oxygen content that a gap semiconductor model for the electronic structure of YBCO is appropriate, there exist mid-gap states which can be probed with infrared radiation. Illumination with visible light, say 2.4 eV photons, causes the response [$-\Delta T/T$ [79, 80] or infrared quenching [30, 33]] of the sample to infrared light to change. Both of these effects have been observed for photon energies as low as .25 eV (for the HE band of Refs.[79, 80] and Ref. [30] for IR

quenching). Furthermore, before visible illumination, exposure to IR light for photon energies as low as .93 eV results in a decrease in resistivity. Then, for a visible photon dose as small as 1 part in 10^4 required to saturate the photoconductive response to visible light, the response to IR completely changes character.

Recalling the mode-bleaching results discussed in Section 2.4.4 [76, 77, 78], the photon dose dependence of IR quenching measurements is additional evidence for a polaronic distortion playing an important role in the photoconductive properties of YBCO. The photoconductive response to IR light is extremely sensitive to whether or not the sample has been exposed to visible light. The time scale (or equivalently photon dose) over which this dramatic change in the character of the response occurs is small compared to the time it takes to observe changes in the resistivity during illumination. Illumination induced changes in the IR spectrum below .1 eV of $\text{YBa}_2\text{Cu}_3\text{O}_{6+x}$ ($x \approx .2$) show a suppression of modes associated with tetragonal symmetry and concomitant emergence of modes associated with orthorhombic symmetry [76, 77, 78]. Furthermore, these modes are associated with the basal plane, i.e. the CuO chains. The authors interpret their results as implying the formation of polarons, in the form of a local orthorhombic distortion in the lattice in the chain region. We are motivated by these experimental results to propose a model for PPC in which the illumination initially causes trapped carriers to occur in the basal plane, leading to the observed structural rearrangements [113]. This model will be in the form of a cellular automata. A flowchart representation of the code for this program is in the Appendix.

5.3 Cellular Automata Model for PPC

5.3.1 Motivation

Cellular automata are often used in an attempt to explain the dynamical behavior of physical systems which have many degrees of freedom [114, 115, 116]. The underlying belief of the theory of Self-Organized Criticality is that ‘spatially extended dynamical systems’ naturally evolve towards a critical state in which infinitesimal perturbations can lead to system responses on all length and time scales [116]. The theory was originally born out of an attempt to explain what the authors called ‘ubiquitous’ $1/f$ noise in the power spectrum of many physical systems such as earthquake faults, traffic, sunspots, etc. Obviously, the physical mechanism behind the noise is different in each of these systems, yet there seems to be underlying principles at work which result in the common behavior in the power spectrum.

The existence of $1/f$ noise in the power spectrum of electrical systems is well known, yet poorly understood. The prototype model often cited is a resistor in series with a constant current source. If one plots the voltage fluctuations from the average voltage drop across the resistor, one will find fluctuations which scale inversely with the frequency. These voltage (resistance) fluctuations are the source of much debate and many mechanisms have been proposed, yet they are still only understood phenomenologically [117]. A simple model based on a cellular automata called the sandpile model attempted to replicate the underlying dynamics of systems exhibiting $1/f$ noise in terms of power law behavior and critical scaling exponents. Later the approach was shown to be somewhat flawed, and the sandpile model was not as universal applicable as originally claimed (See for example Ch. 2 in Ref [114]).

There are several interesting parallels between the normal state properties of YBCO and systems which have been claimed to exhibit self-organized critical behavior. First of all, in measurements [118] of low-frequency resistance fluctuations of YBCO, the $1/f$ noise was found to be 3-7 orders of magnitude larger than in comparable metal films. As a function of oxygen content, the noise magnitude goes through a sharp minimum near the ‘pure’ O-II phase. The authors are able to link this large noise magnitude to vacancy creation in the basal plane. Secondly, the excess conductivity as a result of illumination, or the decay of resistivity during illumination is phenomenologically fit to stretched exponential dependence (Eqn. 2.1 or 2.2) without any understanding of the microscopic physics. Most authors make vague reference to ‘glassy dynamics’ or ‘systems with a distribution of time constants’ when discussing this fit, yet there is no consensus as to the underlying mechanism. We note that when certain systems which obey self-organizing principles are perturbed, energy is dissipated on a variety of time scales.

5.3.2 Model

The preceding discussion has led us to try a similar model for the microscopic mechanism for PPC. Like Bak et al’s model of a sandpile, we use a two dimensional square array of integers to represent the basal plane. We represent the basal plane by a square array shown in Figure 37. For reasons of computational efficiency, we have assigned the Cu(1) sites to even-even coordinates in terms of the ordered pair (Y, Z) shown on Figure 37. Oxygen vacancies are assigned to even-odd, and odd-even coordinates. Odd-odd sites are not occupied, as these are interstitial sites. The oxygen

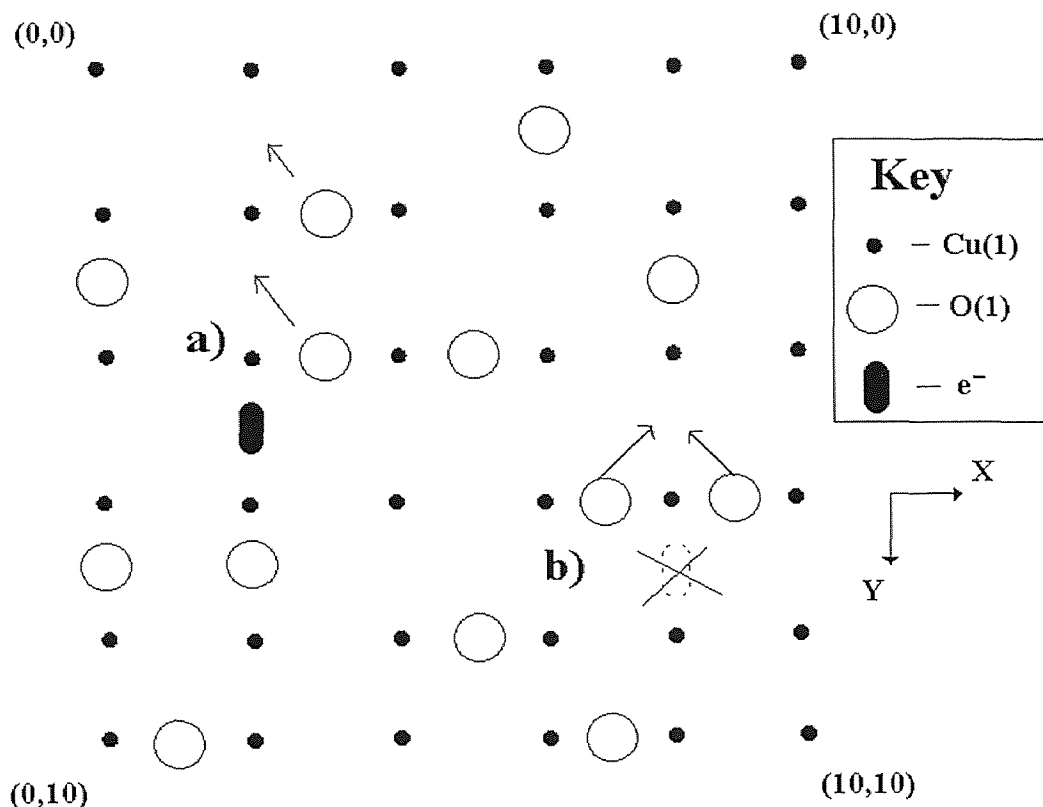


Figure 37 Representation of basal plane of oxygen deficient YBCO below the metal insulator transition. (a) an electron is trapped leading to the motion of oxygen into the chains, the disturbance propagates to the next lattice site – it will propagate until it reaches a vacancy or the situation in (b) electron cannot be trapped because oxygen cannot move into chain.

content is fixed at the start and vacancies are filled randomly. Since the simulation is designed with low temperature illumination experiments in mind, the oxygen is considered to be ‘frozen’ in place. Once the oxygen sublattice is populated, the mean chain length is computed. The distribution of various chain lengths in our model are consistent with previously reported calculations [27, 28]. We typically chose an array size that included $N \times (N+1)$ oxygen sites, a fraction, x , of which are occupied. Here, x is the oxygen content in $YBa_2Cu_3O_{6+x}$.

Once the array has been built up, oxygen vacancies are chosen at random and perturbed, by illumination and the absorption of photons with the subsequent generation of electron-hole pairs. We associate each perturbation with a unit of time. We feel that this is justified because the magnitude of the PPC effect has been shown to depend only on the cumulative photon dose [23]. At fixed flux, each *absorbed* photon produces an electron-hole pair, so the number of perturbations and time are directly proportional. Once a vacancy has been chosen, the local occupancy is scanned and a 'photogenerated' electron can be trapped provided the following conditions are met: 1) the trapping of an electron results in the motion of oxygen into the chain layer, 2) there is a vacancy for the oxygen to move into, and 3) there is no more than one trapped electron per unit cell. Figure 37 gives two illustrative examples for consideration. Once the initial trap event has occurred, the disturbance is allowed to propagate along the chain (Y), proceeding until a vacancy is encountered (Fig. 37a). Alternatively, both diagonal sites could be filled ($X \pm 1$) in which case the disturbance would not be allowed to propagate (Fig. 37b), and therefore the electron would not be trapped. In this fashion, we see the trapping event as requiring a balance of long and short-range forces. First, the electron exerts a local influence on the Cu(1) sites. This disturbance is passed along, propagating only along the chain directions, causing an instability which allows for reordering of the oxygen atoms. After each trapping event, the average chain length is computed, with the electron considered to bridge adjacent Cu(1) sites. Although it wasn't part of the original motivation, the short range interactions are consistent with the ASYNNNI model discussed in Section 2.4.2. The ability of the disturbance to be

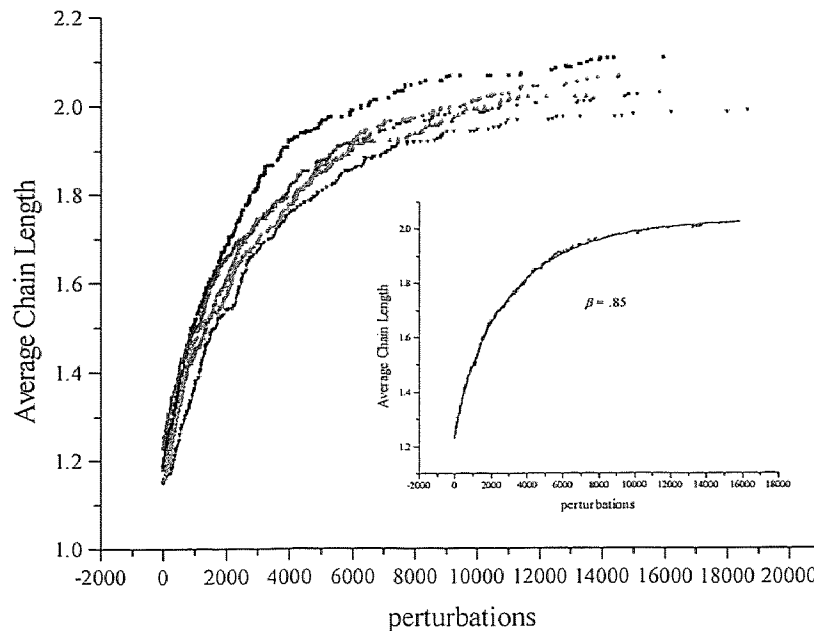


Figure 38 Growth of average chain length while lattice is perturbed. Inset shows fit of Eqn. 5.1 to data for one of the lattices with $\beta = .85$.

transmitted throughout the lattice relieves the criticism that the range of interaction is limited [65].

The average chain length is recorded as a function of the number of perturbations. Figure 38 shows the results for several lattices with 50x51 unit cells. The average chain length rises steeply at first, and then levels off quickly, characteristic of stretched exponential growth. We have fit the chain length to the following form:

$$l(\text{pert}) = l_{\infty} - \Delta l \cdot \exp\left(\frac{\text{pert}}{\text{pert}_{\text{fit}}}\right)^{\beta} \quad (5.1)$$

The change induced by 'illumination' is $\Delta l = l_{\infty} - l_0$, pert is the number of perturbations, and pert_{fit} is a constant obtained from the fit (analogous to τ_{fit} in Refs. [23, 40]). The

average chain length before the lattice is perturbed is l_0 and the final value is l_∞ . For the several lattices shown in Figure 38, $\Delta l/l \approx 65\text{-}70\%$. Typically, β varies between .75 and .85. The fit to Eqn 5.1 with $\beta = .84$ for one of the lattices is shown in the inset of Figure 38.

5.3.3 Single Band Model

In a one band model for the electronic structure of YBCO, relative changes in resistivity are given by:

$$\frac{\Delta\rho}{\rho} = -\left(\frac{\Delta\mu}{\mu} + \frac{\Delta p}{p}\right) \quad (5.2)$$

The hole density is p , and we will define it as the number of hole per formula unit CuO_2 . As a starting point for analysis, we think it reasonable to assume $\rho \sim 1/l$ where l is the average chain length, as will be justified below. The changes in resistivity due to illumination will be accounted for in the following way. First we will count the number of chains of greater than the minimum length necessary to ‘inject’ holes into the CuO_2 planes (i.e. $l \geq 3$). It has been theorized [63, 65, 119, 120, 121] that chains greater than this critical length transfer holes to the puckered planes. Furthermore the amount of holes transferred is proportional to the length of the chains with the proportionality factor being around 0.7 [63, 65, 119, 120, 121]. However, the possibility is held out that the proportionality factor may be closer to 0.4 or 0.5 than 0.7 for shorter chains. Finally, in order to calculate $\Delta p/p$, we must know the hole density before illumination. For $\text{YBa}_2\text{Cu}_3\text{O}_{6.3}$ we expect p to be .026 in accordance with Refs. [32, 122, 123].

Next we turn our attention to the increase in average chain length, Δl . We would like to directly correlate this with an increase in mobility. We think that such an association is reasonable because optical measurements on crystals show that increasing the chain length (oxygen content) results in a lower effective mass, and hence mobility [17, 124]. Extrapolating the infrared conductivity measurements of Ref. [124] to near DC frequencies shows that the scattering time is not dramatically different for fully oxygenated YBCO as it is for oxygen deficient material. Conversely, the effective mass for YBCO with several different oxygen contents is very similar in the mid-infrared, but is very different near DC frequencies [124]. The net result is that the mobility is enhanced by increasing the chain length. Within our range of current understanding the only significant changes that occur as the result of adding oxygen are an increase in the average chain length and an increase in the hole density in the planes. Therefore, in accounting for our results, we feel that the association $\Delta l/l \approx \Delta\mu/\mu$ is appropriate.

We would like to comment on the proportionality factor governing the amount of holes transferred from the chains to the planes. According to Refs. [63, 65, 119, 120, 121] charge transfer occurs for chain fragments greater than length 3. We note that the factor controlling the transfer of holes out the chains may be closer to .5 for short chains ($n \leq 6$) [63, 65, 119, 120, 121]. It is stated quite clearly that the use of the factor .7 is valid in the limit of infinitely long chains. In the case that we use .5, we see about a 10% reduction of $\Delta p/p$ than if we use .7. The vast majority of chains that develop are less than length 6, so this is not a terribly critical point.

For the five lattices that we have considered the average relative change in the mobility, $\Delta\mu/\mu = .7$. The average increase in hole density, $\Delta p/p = .35$. So, in accordance with a single band model, $\Delta\rho/\rho \approx -1.1$. This is in good agreement with our previous experimental results [33] as well as those of others [27, 28, 110]. Our results are in rough agreement with Tanabe et al's study [110] in which the increase in mobility dominates the increase in hole concentration for a $\text{YBa}_2\text{Cu}_3\text{O}_{6.35}$ thin film. In Tanabe et al's work the change in mobility outweighed the change in hole concentration by a factor of about 2.5 [110]. (We observe a smaller ratio, approximately 2.1). Additionally, their results show that the relative increase in hole density is independent of oxygen content. From our computer simulation, we predict a larger relative change in the hole density than they do. This discrepancy may be related to the fact that we are just below the metal insulator transition, while they were right on the metallic side. We note that our predicted increase (again from simulations) in CuO_2 plane hole concentration is right on the threshold for superconductivity, and overall metallic behavior. Since the hole concentration drops off rapidly below the insulator-metal transition, a small increase in carrier concentration should lead to a much larger relative change in hole density. This would help explain the extremely large $\Delta\sigma/\sigma$ (2.9) for a $\text{GdBa}_2\text{Cu}_3\text{O}_{6.1}$ sample reported in Ref. [27, 28]. When $\Delta\sigma/\sigma$ is plotted vs. oxygen concentration for $R\text{Ba}_2\text{Cu}_3\text{O}_{6+x}$ ($R = \text{Y, Gd}$), the increase in $\Delta\sigma/\sigma$ below the metal insulator transition is said to be 'faster than exponential [27, 28].' Based on our model, we would predict that this is due to the large relative change in hole concentration, and that further below the metal-insulator transition ($x < .3$) the increase in hole concentration will dominate the increase in mobility.

As a final step, we have developed a functional form for the resistivity as a function of illumination time (perturbations). This is shown in Figure 39, where the fit parameters appear on the graph. The dependence on perturbations is clearly that of a stretched exponential with $\beta = .75$. Our results are applicable in the limit of a weak flux, in that only one disturbance propagates at a time.

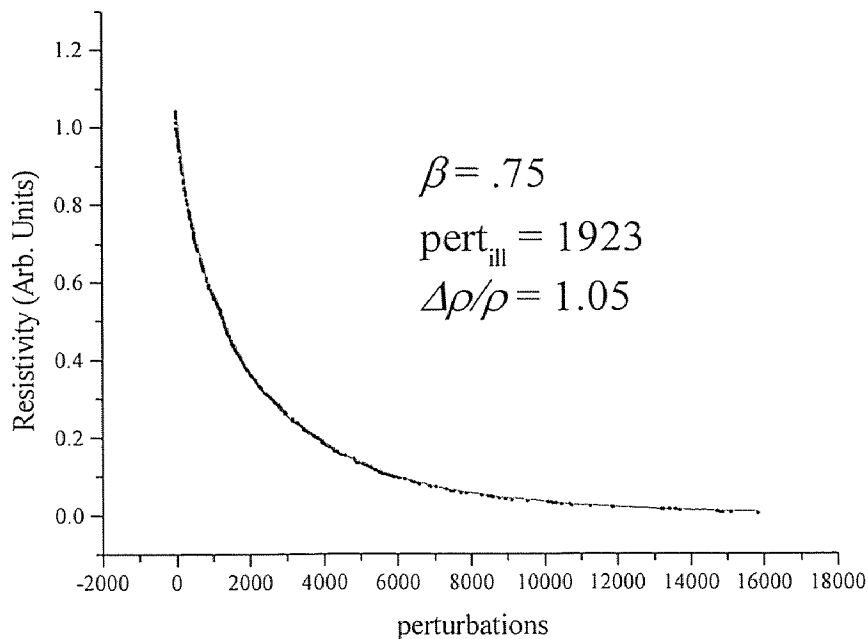


Figure 39 Simulated resistivity as a function of ‘illumination time’ (perturbations).

5.3.4 Further Applications of the Model

The cellular automata model described above has only been applied in a narrow range of oxygen concentration below the metal insulator transition. To extend the model to regions in the phase diagram where the crystal structure has orthorhombic symmetry

will require modification. Certainly, once the material no longer has tetragonal symmetry, we will need to make adjustments. However, one of the advantages (appeals) of the existing model is that the computer code necessary to simulate the basal plane only uses integers and integer arrays. This allows for computing efficiency in the form of small programs and memory requirements. One could imagine ways in which the existing code could be modified in order to treat orthorhombic material such as using the neutron data of Ref. [92] to populate the various $O(1)_1$, $O(1)_2$, and $O(5)$ (See Fig. 11) sublattices separately. Certainly, the oxygen distribution in the basal plane could no longer be considered to be random, but it would be interesting to see if random population of the separate sublattices still led to long-range order. These modifications would allow us to still use a square array and keep the program relatively simple.

Another interesting question that presents itself is, if the model can be used in regions with orthorhombic symmetry, can it account for the observed resonant Raman scattering (RRS)? Recall that the Raman efficiency has been observed to be largest near the O-III phase, i.e. $YBa_2Cu_3O_{6.67}$ [53, 55, 56]. It appears that the resonance has something to do with chain ends, i.e. an electronic excitation near an oxygen vacancy [55]. Of course, this is contingent upon one correctly identifying the polarizability and atomic displacement that results from the resonance (recall that the Raman efficiency

$\propto \frac{\partial \alpha}{\partial u} u$ where α is the polarizability and u is the atomic displacement).

CHAPTER 6

CONCLUSION

6.1 Summary of Results

The post-visible illuminated infrared photoconductivity spectrum was measured in the range 1.2 to 1.6 eV on YBCO thin films. We discovered that there is a correlation between our current work and prior results [79, 80, 85]. These results can be used to extend our interpretation and suggest that there is a broad distribution of narrowly spaced levels ($\Delta\varepsilon/\varepsilon \ll 1$ where ε is the energy level) between .25 eV and 1.6 eV. The photon dose dependence measurements of the IR quenching efficiency suggest that the local structure changes which appear almost immediately upon illumination [76, 77, 78] could be related to the population of defects which result in basal plane structural rearrangement.

In support of such a scenario, a cellular automata model is proposed in which populated defects, in the form of oxygen vacancies which trap photogenerated electrons, results in a more ordered configuration in the basal plane. This leads the prediction of a lower resistivity state when the results are interpreted within the context of the charge transfer hypothesis [63, 65, 119, 120, 121], if we associate the lengthening of the chains with an increase of the mobility, and assume a single band model for the electronic structure of YBCO. Also, our predicted relative change in resistivity due to illumination is consistent with our previous experimental results [33] as well as others [27, 28, 110]. Finally, we are able to construct a resistivity vs. time curve from our simulated data which has the same functional form as that is observed

experimentally [113]. It seems that we may have a successful marriage of the vacancy capture model and the ‘oxygen-ordering’ models.

For these reason we think the model may have more general applicability than the narrow region of oxygen concentration that we have applied it to. It would be interesting if we could predict the dependence of $\Delta\sigma/\sigma$ on oxygen content. Also, resonant Raman scattering could be investigated within the context of this model.

6.2 Future Experimental Work

There are still a number of interesting experiments to be done. In particular, one might do $1/f$ -noise measurements before, during and after illumination. Because of the success that others have had in using similar models to probe $1/f$ noise in other systems [115, 116], we may expect that there will be a relationship between the noise magnitude and the amount of basal plane disorder. In particular, we might expect a crossover to white noise near the pure O-II phase. Other experiments might include extending the photoluminescence measurements of Federici et al. [29] to include those regions between 3.4 eV and the large peak in the PPC efficiency spectrum at 4.1 eV.

APPENDIX

REPRESENTATION OF CELLULAR AUTOMATA

The following diagram represents the programming code for the cellular automata described in Chapter 5. The actual code is written in the Microsoft VisualBasic 6.0 language.

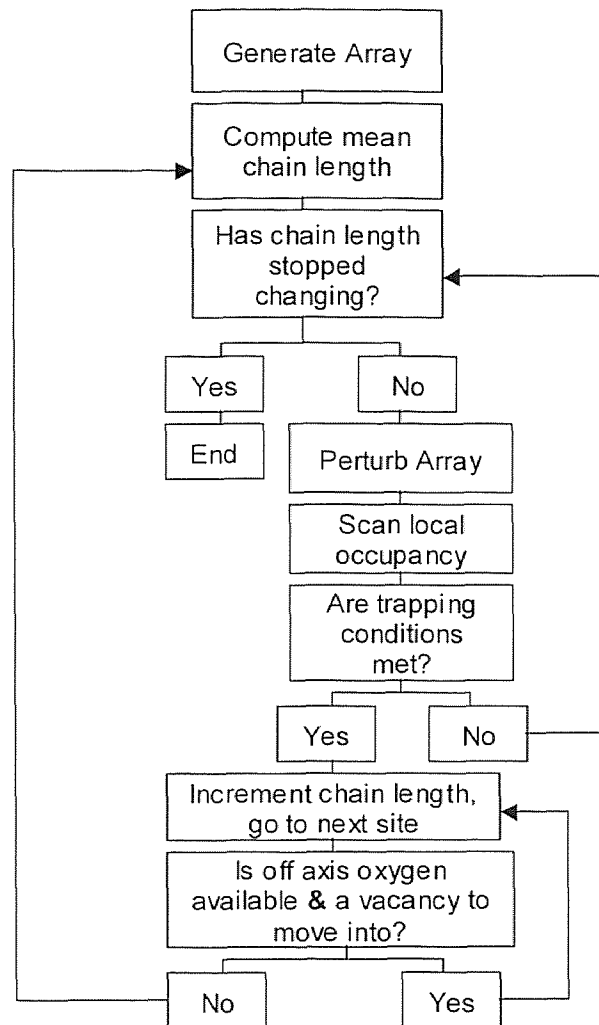


Figure 40 Flowchart representing Cellular Automata code.

REFERENCES

1. A. Gilabert, A. Hoffman, M. G. Medici, and I. K. Schuller, accepted for publication Journal of Superconductivity.
2. L. R. Testardi, Phys. Rev. B **4**, 2189, (1971).
3. H. Kamerlingh Onnes, Akad. Van Wetenschappen (Amsterdam) **14**, 818 (1911).
4. J. Bardeen, L. N. Cooper, and J. R. Shreiffier, Phys. Rev. **108**, 1175 (1957).
5. D. R. Tilley and J. Tilley, *Superfluidity and Superconductivity*, Graduate Student Series in Physics, Ed. D. Brewer (Philadelphia, IOP Publishing, 1994), 3rd Ed.
6. J. F. Federici, B. I. Greene, P. N. Saeta, D. R. Dykaar, F. Sharifi, and R. C. Dynes, Phys. Rev. B **46**, 11 153 (1992).
7. C. Kittel, *Introduction to Solid State Physics* (New York, Wiley, 1996) 7th Ed.
8. J. G. Bednorz and K. Mueller, Z. Phys. B **64**, 189 (1986).
9. P. W. Anderson, *The Theory of Superconductivity in the High- T_c Cuprates* (Princeton Univ. Press, Princeton, 1997).
10. C. P. Poole, H. A. Farach, and R. J. Creswick, *Superconductivity* (Acad. Press, San Diego, 1995).
11. W. Pickett, Rev. Mod. Phys. **61**, 433 (1989).
12. M. K. Wu, J. R. Ashburn, C. J. Torng, P. H. Hor, R. L. Meng, L. Gao, Z. J. Huang, Y. Q. Wang, and C. W. Chu, Phys. Rev. Lett. **58**, 908, (1987).
13. J. D. Jorgenson, M. A. Beno, D. G. Hinks, L. Solderholm, K. J. Volin, C. U. Segre, K. Zhang, and M. S. Kleefisch, Phys. Rev. B **36**, 3608 (1987).
14. J. D. Jorgenson, S. Pei, P. Lightfoot, H. Shi, A. P. Paulikus, and B. W. Veal, Physica C **167**, 571 (1990).
15. B. W. Veal, A. P. Paulikas, Hoydoo You, Hao Shi, Y. Fang, and J. W. Downey, Phys. Rev. B **42**, 6305 (1990).
16. R. J. Cava, B. Batlogg, K. M. Rabe, E. A. Rietman, P. K. Gallagher, and L. W. Rupp Jr., Physica C **156**, 523 (1988).
17. J. Kircher, M. Cardona, A. Zibold, K. Widder, and H. P. Geserich, Phys. Rev. B **48**, 9684 (1993).

18. H. A. Blackstead, J. D. Dow, J. F. Federici, William E. Packard, D. B. Pulling, *Physica C* **235-240**, 2161 (1994).
19. H. A. Blackstead and J. D. Dow, *J. Appl. Phys.* **81**, 6285 (1997).
20. H. A. Blackstead, D. B. Chrisey, J. D. Dow, J. S. Horwitz, A. E. Klunzinger, D. B. Pulling, *Physica C* **235-240**, 1539 (1994).
21. Z. Zou, K. Ota, T. Ito, and Y. Nishihara, *Jpn. J. Appl. Phys. Lett.* **36**, L18, (1997).
22. T. Ushgawa, Y. Ishamaru, J. Wen, T. Utagawa, S. Koyama, and Y. Enomoto, *Jpn. J. Appl. Phys.* **36**, L1583 (1997).
23. V. I. Kudinov, I. L. Chaplygin, N.M. Kreines, A.. I. Kirulyik, R. Laiho, E. Lähderanta, and C. Ayache, *Phys. Rev. B* **47**, 9017 (1993).
24. D. Lederman, J. Hasen, I. K. Schuller, E. Osquiguil, and Y. Bruynseraede, *Appl. Phys. Lett.* **64**, 652 (1994).
25. T. A. Tyson, J. F. Federici, D. Chew, A. R. Bishop, L. Furenlid, W. Savin, and W. Wilber, *Physica C* **292**, 163 (1997).
26. E. Osquiguil, M. Maenhoudt, B. Wuyts, Y. Bryunseraede, D. Lederman, and I. K. Schuller, *Phys. Rev. B* **49**, 3675 (1994).
27. J. Hasen, D. Lederman, I. K. Schuller, V. Kudinov, M. Maenhoudt, and Y. Bruynseraede, *Phys. Rev. B* **51**, 1342 (1995).
28. J. Hasen, Ph.D. Thesis, University of California San Diego, (1995).
29. J. F. Federici, D. Chew, B. Welker, W. Savin, J. Gutierrez-Solana, T. Fink, and W. Wilber, *Phys. Rev. B* **52**, 15 592 (1995).
30. D. C. Chew, J. F. Federici, J. Gutierrez-Solona, G. Molina, W. Savin, and W. Wilber, *Appl. Phys. Lett.* **69**, 3260 (1996).
31. J. I. Pankove, *Optical Processes in Semiconductors* (Dover, New York, 1971), Ch. 17.
32. H. Zhang and H. Sato, *Phys. Rev. Lett* **70**, 1697 (1993).
33. D. M. Bubb, J. F. Federici, S. Tidrow, W. Wilber, A. Piqué, and J. Kim, *Phys. Rev. B* **60**, 6827 (1999).
34. G. Grigelionis, E. Tornau, and A. Rosengren, *Phys. Rev. B* **53**, 425, (1996).
35. A. Heilman, Ph.D. Thesis, Notre Dame University, (1998).

36. J. Kircher, M. K. Kelly, S. Rashkeev, M. Alouani, D. Fuchs, and M. Cardona, *Phys. Rev. B* **44**, 217, (1991).
37. J. F. Federici and D. M. Bubb, *unpublished*.
38. P. M. Mooney, *J. Appl. Phys.* **67**, R1 (1990).
39. J. Y. Lin, A. Dissanayake, G. Brown, and H. X. Jiang, *Phys. Rev. B* **42**, 5855, (1990).
40. W. Markowitsch, C. Stockinger, W. Göb, W. Lang, W. Kula, and R. Sobolewski, *Physica C* **265**, 187, (1996).
41. S. L. Bud'ko, H. H. Feng, M. F. Davis, J. C. Wolfe, and P. H. Hor, *Phys. Rev. B* **48**, 16 707 (1993).
42. K. Kawamoto and I Hirabayashi, *Phys. Rev. B* **49**, 3655 (1994).
43. J. Guimpel, M. Maiorov, E. Osquiguil, G. Nieva, and F. Pardo, *Phys. Rev. B* **56**, 3552 (1997).
44. K. Widder, J. Münzel, M. Göppert, D. Lürßen, R. Becker, A. Dinger, H. P. Geserich, C. Klingshern, M. Kläser, G. Müller-Vogt, J. Geerk, and V. M. Berkalov, *Physica C* **300**, 115 (1997).
45. G. Nieva, E. Osquiguil, J. Guimpel, M. Maenhoudt, B. Wuyts, Y. Bruynseraede, M. B. Maple, and I. K. Schuller, *Phys. Rev. B* **46**, 14 249 (1992).
46. T. Endo, A. Hoffmann, J. Santamaria, and I. K. Schuller, *Phys. Rev. B* **54**, 3750 (1996).
47. M. K. Kelly, P. Barboux, J. M. Tarascon, D. Aspnes, W. A. Bonner, and P. A. Morris, *Phys. Rev. B* **38**, 870 (1988).
48. A. Michaelis, E. A. Irene, O. Auciello, and A. R. Krauss, *Journal Appl. Phys.* **83**, 7736, (1998).
49. C. L. Lin, Y. K. Lin, C. C. Chi, W. Y. Guan, and M. K. Wu, *Appl. Phys. Lett.* **71**, 3284 (1997).
50. R. S. Liu, J. R. Cooper, J. W. Loram, W. Zhou, W. Lo, P. P. Edwards, W. Y. Liang, and L. S. Chen, *Solid State Comm.* **76**, 679 (1990).
51. A. Hoffmann, I. K. Schuller, Z. F. Ren, J. Y. Lao, and J. H. Wang, *Phys. Rev. B* **56**, 13 742, (1997).

52. Y. Kubo, Y. Shimakawa, T. Manako, and H. Igarashi, *Phys. Rev. B* **43**, 7875, (1991).
53. A. Fainstein, P. Etchegoin, and J. Guimpel, *Phys. Rev. B* **58**, 9433 (1998).
54. D. R. Wake, F. Slakey, M. V. Klein, J. P. Rice, and D. M. Ginsberg, *Phys. Rev. Lett* **67**, 3728 (1991).
55. M. Käll, M. Osada, M. Kakihana, L. Börjesson, T. Frello, J. Madsen, N. H. Andersen, R. Liang, P. Dosanjh, and W. N. Hardy, *Phys. Rev. B* **57**, 14 072 (1998).
56. A. G. Panfilov, A. I. Rykov, and S. Tajima, *Phys. Rev. B* **58**, 12 459 (1998).
57. D. Mønster, P. -A. Lingård, and N. H. Andersen, *Phys. Rev. B* **60**, 110 (1999).
58. S. Horiuchi, *Jpn. J. Appl. Phys.* **31**, L1335, (1992).
59. S. Horiuchi, Y. Matsui, and B. Okai, *J. Appl. Phys.* **31**, L59, (1992).
60. M. Iliev, C. Thompson, V. Hadjiev, and M. Cardona, *Phys. Rev. B* **47**, 12 341, (1993).
61. Y. F. Hsieh, M. P. Siegel, R. Hull, and J. M. Phillips, *Appl. Phys. Lett.* **57**, 2268, (1990).
62. N. Newman, and W. G. Lyons, *J. Supercond.* **6**, 119 (1993).
63. G. V. Uimin, V.F. Gentmakher, A. M. Neminsky, L. A. Novomlinsky, D. V. Shovkum, and P. Brüll, *Physica C* **192**, 481 (1992).
64. L. T. Wille, A. Berrera, and D. Fontaine, *Phys. Rev. Lett.* **60**, 1065 (1988).
65. G. Uimin, *Phys. Rev B* **50**, 9531 (1996).
66. J. Oitmaa, Y. Jie, L. T. Wille, *J. Phys. : Cond. Matt.* **5**, 4161 (1993).
67. H. Schmid, E. Burkhardt, B. N. Sun, and J. P. Rivera, *Physica C* **157**, 555 (1989).
68. T. Fiig, N. H. Andersen, P. -A. Lingård, J. Berlin, and O. G. Mouritsen, *Phys. Rev. B* **54**, 556 (1996).
69. D. Mønster, P. -A. Lingård, and N. H. Andersen, *Phys. Rev. B* **60**, 110, 1999.
70. M. v. Zimmermann, T. Frello, N. H. Andersen, J. Madsen, M. Käll, O. Schmidt, T. Niemöller, J. R. Schneider, H. F. Poulsen, Th. Wolf, R. Liang, P. Dosanjh, W. N. Hardy, to be published, preprint available at xxx.lanl.gov/cond-mat/9906251

71. S. Lapinskas, A. Rosengren, and E. Tornau, *Physica C* **199**, 91 (1991).
72. N. Kristoffel and P. Rubin, *J. Phys. Cond. Matt.* **10**, L127, (1998).
73. N. Kristoffel and M. Klopov, *Phys. Rev. B* **54**, 9074 (1996).
74. S. O. Hemila and R. H. Bube, *J. Appl. Phys.* **38**, 5258 (1967).
75. O. Ray, P. Smorchkova, and N. Samarth, *Phys. Rev. B* **59**, 9810, (1999).
76. Y. H. Kim, C. M. Foster, and A. J. Heeger, *Phys. Rev. B* **38**, 6478 (1988).
77. D. Mihailović, C. M. Foster, K. Voss, and A. J. Heeger, *Phys. Rev. B* **42**, 7989 (1990).
78. D. Mihailović, C. M. Foster, K. Voss, T. Mertelj, I. Poberaj, and N. Herron, *Phys. Rev. B* **44**, 237 (1991).
79. X. Wei, L. Chen, and Z. V. Vardeny, C. Taliani, R. Zamboni, A. J. Pal, and G. Ruani, *Physica C* **162-4**, 1109 (1999).
80. C. Taliani, A. J. Pal, G. Ruani, R. Zamboni, X. Wei, and Z. L. Vardeny, in *Electronic Properties of High T_c Superconductors and Related Compounds*, Edited by H. Kuzmany, M. Mehring, and J. Fink, (Berlin : Springer Verlag, 1990), Solid State Physics Series.
81. H. P. Geserich, in *Electronic Properties of High T_c Superconductors and Related Compounds*, Edited by H. Kuzmany, M. Mehring, and J. Fink, (Berlin : Springer Verlag, 1990), Solid State Physics Series.
82. H. Yasuoka, H. Mazaki, T. Terashima, and Y. Bando, *Physica C* **175**, 192 (1996).
83. G. A. Thomas, D. H. Rapkine, S. L. Cooper, S. -W. Cheong, A. S. Cooper, L. F. Schneemeyer, and J. V. Waszczak, *Phys. Rev. B* **45**, 2474 (1992).
84. J. Orenstein, G. A. Thomas, A. J. Millis, S. L. Cooper, D. H. Rapkine, T. Timusk, L. F. Schneemeyer, and J. V. Waszczak, *Phys. Rev. B* **42**, 6342 (1990).
85. V. N. Denisov, C. Taliani, A. G. Mal'shukov, V. M. Burkhalov, E. Schonherr, and G. Ruani, *Phys. Rev. B* **48**, 16 714 (1993).
86. E. T. Heyen, J. Kircher, and M. Cardona, *Phys. Rev. B* **45**, 3037 (1992).
87. I. Poberaj and D. Mihailović, *Phys. Rev. B* **50**, 6426 (1990).
88. G. Yu, C. H. Lee, A. J. Heeger, N. Herron, and E. M. McCarron, *Phys. Rev. Lett.* **67**, 2581 (1991).

89. J. Mustre de Leon, S. D. Conradson, A. R. Bishop, and I. Batistic, *Phys. Rev. Lett.* **65**, 4675 (1990).
90. J. Cheung and J. Horwitz, *Material Research Society Bulletin XVII, No. 2*, 30, (1992).
91. J. Zhang, R. A. Gardiner, P. S. Kirlin, R. W. Boerstler, and J. Steinbeck, *Appl. Phys. Lett.* **61**, 2884 (1992).
92. J. D. Jorgensen, B. W. Veal, A. Paulikas, L. J. Nowicki, G. W. Crabtree, H. Claus, W. K. Kwok, *Phys. Rev. B* **41** 1863 (1990).
93. E. Takayama-Muromachi, Y. Uchida, M. Ishii, T. Tanaka, and K. Kato, *Jpn. J. Appl. Phys.* **26**, L1156, (1987).
94. J. Ye and K. Nakamura, *Phys. Rev. B* **48**, 7554 (1993).
95. L. A. Farrow, S. -W. Chan, L. H. Greene, and W. L. Feldman, *J. Appl. Phys.* **65**, 2381 (1989).
96. T. Venkatesan, C. C. Chang, D. Dijkkamp, S. B. Ogale, E. W. Chase, L. A. Farrow, D. M. Hwang, P. F. Miceli, S. A. Schwarz, J. M. Tarascon, X. D. Wu, and A. Inam, *J. Appl. Phys.* **63**, 4591 (1989).
97. S. Degoy, J. Jiménez, P. Martin, O. Martinez, A. C. Prieto, D. Chambonnet, C. Audry, C. Belouet, and J. Perrière, *Physica C* **256**, 291 (1996).
98. R. G. Munro and H. Chen, *Journal of the American Ceramic Society* **79**, 603 (1996).
99. Superconductive Components Inc., materials catalog.
100. D. J. Werder, C. H. Chen, R. J. Cava, and B. Battlogg, *Phys. Rev. B* **37**, 2317 (1987).
101. R. J. Cava, B. Battlogg, R. B. van Dover, D. W. Murphy, S. Sunshine, T. Siegrist, J. P. Remeika, E. A. Reitman, S. Zahurak, and G. P. Espinosa, *Phys. Rev. Lett.* **58**, 1676 (1987).
102. B. E. Warren, *X-Ray Diffraction*, (New York : Dover, 1969), Reprinted 1990, page 71.
103. R. Bhadra, T. O. Brun, M. A. Beno, B. Dabrowski, D. G. Hinks, J. Z. Liu, J. D. Jorgenson, L. J. Nowicki, A. P. Paulikus, I. K. Schuller, C. U. Segre, L. Solderholm, B. Veal, H. H. Wang, J. M. Williams, K. Zhang, and M. Grimsditch, *Phys. Rev. B* **37**, 5142 (1988).

104. A. Mascarenhas, S. Geller, L. C. Xu, H. Katayama-Yoshida, J. I. Pankove, and S. K. Deb, *Appl. Phys. Lett.* **52**, 242 (1988).
105. G. Burns, F. H. Dacol, C. Field, and F. Holtzberg, *Physica C* **181**, 37 (1991).
106. A. Bock, *Phys. Rev. B* **51**, 15 506 (1995).
107. A. Bock, R. Kursten, M. Bruhl, N. Dieckman, and U. Merkt, *Phys. Rev. B* **54**, 4300 (1996).
108. D. M. Bubb and Z. Iqbal, *unpublished*.
109. Valdes, L. G., *Proc. I.R.E.* **42**, 420 1954, also helpful information found at <http://www.ece.uiuc.edu/ece344/Equipment/4PointProbes/Instructions.html#Intro>.
110. K. Tanabe, S. Kubo, F. Hosseini Tehrani, H. Asano, and M. Suzuki, *Phys. Rev. Lett.* **72**, 1537 (1994).
111. J. W. Ekin, T. M. Larson, N. F. Bergren, A. J. Nelson, A. B. Swartzlander, L. L. Kazmerski, A. J. Panson and B. A. Blankenship, *Appl Phys. Lett.* **52**, 1819 (1988).
112. Helpful information may be found at www.srsys.com in the technotes section.
113. D. M. Bubb and J. F. Federici, submitted to *J. Phys.: Cond. Matt.*
114. Henrik Jeldtoft Jensen, *Self Organized Criticality : Emergent Complex Behavior in Physical and Biological Systems*, Cambridge Lecture Notes in Physics, Eds. P. Goddard and J. Yeomans, (New York : Cambridge, 1998).
115. Per Bak, *How Nature Works : The Science of Self Organized Criticality*, (New York : Springer Verlag, 1996).
116. P. Bak, C. Tang, K. Wiesenfeld, *Phys. Rev. A* **38**, 364 (1998).
117. P. Dutta and P. M. Horn, *Rev. Mod. Phys.* **53**, 497 (1981).
118. L. Liu, K. Zhang, H. Jaeger, D. B. Bucholz, and R. P. H. Chang, *Phys. Rev. B* **49**, 3679, (1994).
119. P. Gawiec and D. R. Grempel, A. –C. Riiser, H. Haugerud, and G. Uimin, *Phys. Rev. B* **53** 5872, (1996).
120. P. Gawiec and D. R. Grempel, G. Uimin, and J. Zittarz, *Phys. Rev. B* **53** 5880, (1996).
121. H. Haugerud, G. Uimin, and W. Selke, *Physica C* **275**, 93 (1997).

122. R. F. Wood, and M. Abdel-Raouf, Phys. Rev. B **51**, 11 773 (1995).
123. B. Wuyts, V. V. Moshchalkow, and Y. Bruynseraede, Phys. Rev. B **53**, 9418 (1996).
124. L. D. Rotter, Z. Shlesinger, R. T. Collins, F. Holtzberg, and C. Field, Phys. Rev. Lett. **67**, 2741 (1991).